Part II

Extended analysis and solutions

Chapter 6

Extended analysis of MC systems

In Part I of this thesis some background regarding the effect of nonlinearities in OFDM-based systems was provided. Moreover, we also showed that the OFDM signal suffers from large envelope fluctuations and presented the two metrics that are commonly used to evaluate the envelope fluctuations and, therefore, considered in the design of multicarrier systems. Nevertheless, a general evaluation was not provided, where both the metrics and the distortion term introduced by a nonlinearity were taken into account. The aim of this chapter is to present a deep study of the effect of nonlinear amplification in OFDM-based multicarrier systems, including the extension to sub-Gaussian distributed signals and a deep analysis of PAPR and CM. The presented framework will be used to discuss the suitability of the two metrics and to define the guidelines to be considered when designing the uplink and downlink of wireless communication systems.

In Chapter 4, a theoretical analysis of the effect of nonlinearities in OFDM systems was provided. This was based on the Bussgang theorem, which is valid for Gaussian distributed OFDM signals. According to the central limit theorem, an OFDM signal can be considered to be Gaussian distributed if the amplitude of the subcarriers are independent and identically distributed random variables and the number of subcarriers is large enough. In broadcasting applications [42] or in the downlink of OFDMA systems [55] a large number of subcarriers is generally used. Therefore, the Gaussianity assumption holds. On the other hand, in the OFDMA uplink, the number of subcarriers assigned to each user terminal is usually low. As a result, the Gaussian approximation is not accurate enough.

In Part I, the definitions of the two best known metrics of the envelope fluctuations, namely PAPR and CM, were also provided. Based on those, several techniques to reduce the sensitivity of OFDM systems to nonlinear amplification were defined. Nevertheless, an analysis of the two metrics in OFDM systems was not presented.

In this chapter, the analysis of the effect of nonlinearities is extended to sub-Gaussian distributed signals. Moreover, a general framework is presented, where both the metrics and the distortion term introduced by a nonlinearity are considered. First,

further definitions of the signal metrics and a general analysis in OFDM systems will be given. Next, we will focus on the problem of PAPR-reduction and present extensive simulation results of several well known PAPR-reducing techniques from the literature. Let us recall that PAPR is the best known and employed metric of the envelope fluctuations and, therefore, most of the techniques in the literature are originally designed for PAPR-reduction. Subsequently, the analysis of the effect of nonlinearities will be extended to consider the case where the Gaussian approximation is not so accurate. Finally, the suitability of the two metrics will be discussed, and the guidelines to be followed when designing the uplink and downlink of wireless communication systems will be defined.

6.1 Signal metrics

In Chapter 4, the most common metrics to measure the envelope fluctuations of multicarrier signals, namely PAPR and CM, were introduced. In this section, we provide a deeper study of the two metrics, since they will be used in the subsequent sections to further analyze the effect of nonlinearities in OFDM systems [33].

Peak-to-average power ratio

Let us recall that the PAPR of an OFDM symbol $\mathbf{s}^{(m)}$ is defined as the ratio between its peak power and the average power of all OFDM symbols, see equation (4.4). The most common way to evaluate the PAPR characteristics of the OFDM signal is by means of the complementary cumulative density function. Assuming that the samples are mutually independent, which is true for non-oversampled signals, the CCDF of PAPR of an N-subcarrier OFDM signal, that is, the probability that PAPR exceeds the threshold γ_0, is

$$\Pr(\gamma > \gamma_0) = 1 - (1 - e^{-\gamma_0})^N. \tag{6.1}$$

For oversampled signals, PAPR of an N-subcarrier OFDM signal can be approximated by that of a αN-subcarrier OFDM system without oversampling, where $\alpha > 1$ [98]. Thus, the probability that the PAPR of an oversampled OFDM signal with N subcarriers exceeds the threshold γ_0 is

$$\Pr(\gamma > \gamma_0) \approx 1 - (1 - e^{-\gamma_0})^{\alpha N}. \tag{6.2}$$

As discussed in [98] a value of $\alpha = 2.8$ gives a quite accurate approximation. Figure 6.1 shows the CCDF of PAPR of an OFDM system employing different number of subcarriers and an oversampling factor of $L = 4$. Even though the distribution of PAPR gives a lot of information regarding the PAPR characteristics of an OFDM system, it might not be straightforward to compare different OFDM systems. An easier way is to compute a single value of the PAPR characteristics rather than computing the distribution. Therefore, we will consider the average and maximum PAPR of all

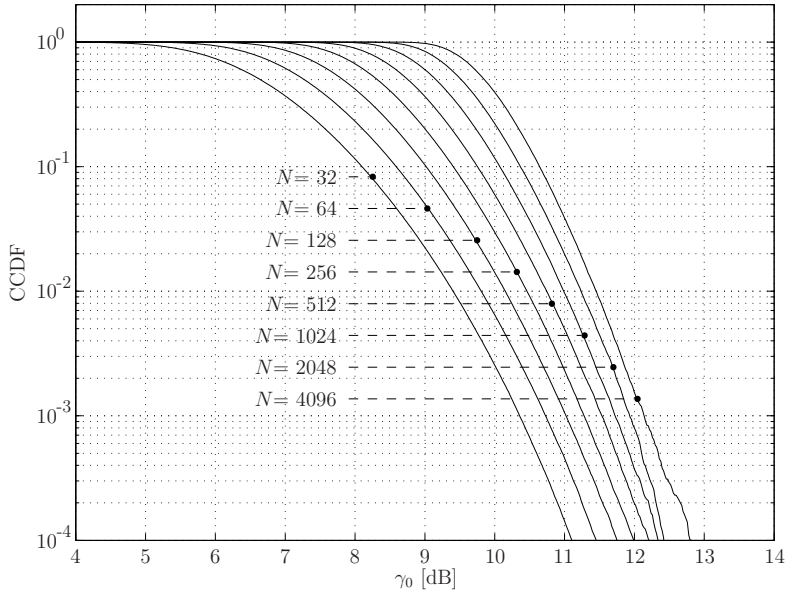

Figure 6.1: Probability that PAPR of an N-subcarrier OFDM symbol exceeds a given threshold.

OFDM symbols as

$$PAPR = E_m\left[\mathrm{PAPR}_m\right], \tag{6.3}$$

$$PAPR_{max} = \max_m \ \mathrm{PAPR}_m = \frac{1}{\sigma^2}\max_m \ \|\mathbf{s}^{(m)}\|_\infty^2, \tag{6.4}$$

respectively, where σ^2 is the average power of the OFDM signal. The maximum PAPR is also referred to as *system PAPR* since it represents the value that would be obtained when computing the PAPR of a sequence containing all the possible OFDM symbols in a system, that is

$$PAPR_{max} = \mathrm{PAPR}\left([\mathbf{s}^{(0)};\mathbf{s}^{(1)};\cdots]\right). \tag{6.5}$$

Let us analyze the PAPR of an OFDM system. From (2.10) and by considering $L = 1$ the instantaneous power of an OFDM symbol can be expressed as

$$|s_n|^2 = \frac{1}{N}\sum_{k=0}^{N-1}\sum_{l=0}^{N-1} S_k S_l^* e^{j\frac{2\pi n}{N}(k-l)}, \qquad n = 0,1,\ldots,N-1. \tag{6.6}$$

Assuming a modulation scheme with an average power $\mathrm{E}[|S_k|^2] = \sigma^2$ it follows that the average power of an OFDM system is also σ^2. Let us now consider a pure OFDM system where no spreading is used. From (6.6), $\mathbf{s}$ will have a maximum PAPR when all its subcarriers are added coherently, i.e. $S_k = S_l;\ \forall k,l$. The instantaneous power of

an OFDM symbol with maximum PAPR can be expressed as

$$\begin{aligned} |s_{n_{\max\ \mathrm{PAPR}}}|^2 &= \frac{1}{N}\sum_{k=0}^{N-1}\sum_{l=0}^{N-1}|S_{\max}|^2 e^{j\frac{2\pi n}{N}(k-l)} \\ &= \frac{1}{N}\sum_{k=0}^{N-1}\sum_{l=0}^{N-1}\sigma^2\mathrm{PAPR}(S)\cdot e^{j\frac{2\pi n}{N}(k-l)} \\ &= \begin{cases} N\sigma^2\cdot\mathrm{PAPR}(S) & \text{if } n=0 \\ 0 & \text{otherwise} \end{cases} \end{aligned} \tag{6.7}$$

and, as a result the PAPR of an OFDM system becomes

$$PAPR_{max} = N\cdot\mathrm{PAPR}(S), \tag{6.8}$$

where $S_{\max}$ is the baseband modulation symbol with maximum power and PAPR(S) is the PAPR of the symbol mapping[1]. Table 6.1 summarizes the PAPR of an OFDM system with different mappings.

M-PSK	16-QAM	32-QAM	64-QAM	128-QAM	256-QAM
N	$1.8N$	$1.7N$	$2.33N$	$2.07N$	$2.65N$

Table 6.1: PAPR of an N-OFDM system with different mappings.

Cubic metric

The raw CM is obtained by first normalizing the signal to a rms value of 1.0 and then computing the rms value of the normalized cubed signal. The general definition of the raw CM of a signal $s(t)$ and the definition of the raw CM of an OFDM symbol $\mathbf{s}^{(m)}$ are found in equations (4.6) and (4.7), respectively. As in PAPR, the CM characteristics of an OFDM signal can be obtained either by computing the distribution of the RCM of each OFDM symbol or by means of the average and maximum RCM, defined as

$$RCM = \sqrt{E_m\left[\mathrm{RCM}_m^2\right]}, \tag{6.9}$$

$$RCM_{max} = \max_m\ \mathrm{RCM}_m, \tag{6.10}$$

respectively. Note that the average raw CM is defined in this thesis as the square root of the mean squared RCM of each OFDM symbol, i.e. the rms of the RCM of all OFDM symbols. The reason is that, then, the average RCM coincides with the RCM

[1]Note that no oversampling is done to compute the maximum PAPR

of a sequence containing all the possible OFDM symbols in a system,

$$RCM = \sqrt{E_m\left[E\left[\left(\frac{|\mathbf{s}^{(m)}|^2}{\sigma^2}\right)^3\right]\right]} = \sqrt{E_{m,n}\left[\left(\frac{|s_n^{(m)}|}{\sigma^2}\right)^3\right]} = \mathrm{RCM}\left([\mathbf{s}^{(0)};\mathbf{s}^{(1)};\cdots]\right). \tag{6.11}$$

Therefore the average RCM is also referred to as the *system RCM*.

Let us now consider the distribution of the raw CM of an OFDM system. From (4.6), the raw CM of a signal $s(t)$ can be expressed as

$$\mathrm{RCM}\left(s(t)\right) = \frac{1}{\sigma^3}\sqrt{E\left[|s(t)|^6\right]}. \tag{6.12}$$

If $s(t)$ is complex Gaussian distributed, then according to Appendix C

$$\mathrm{RCM}\left(s(t)\right) = \sqrt{6}. \tag{6.13}$$

In general the OFDM symbols will not exactly be complex Gaussian distributed and, thus, the RCM of each OFDM symbol will be a value that oscillates around $\sqrt{6}$. From the central limit theorem we know that, the larger the number of subcarriers in the OFDM system is, the more its real and imaginary parts approach a Gaussian distribution. Therefore, one expects that as the number of subcarriers increases the RCM of each OFDM symbol will be closer to $\sqrt{6}$. Figure 6.2 shows the CCDF of the RCM of an OFDM system with different number of subcarriers. It can be observed that, as it was expected, the RCM of each OFDM symbol tends to be $20\log(\sqrt{6}) = 7.78$dB as N increases.

The CCDF curves shown in Figure 6.2 are similar to the Butterworth functions of the form

$$B(t) = \frac{1}{1+\left(\frac{t}{a}\right)^b}. \tag{6.14}$$

In fact it was observed that for $N > 32$, by choosing the appropriate parameters a and b, very accurate approximations of the CCDF curves were achieved. Nevertheless, for the sake of simplicity, a closed equation to approximate the CCDF curves of the RCM of OFDM systems with different number of subcarriers was empirically found to be

$$\Pr(\rho > \rho_0) = \frac{1}{1+\left(\rho_0/\left(\sqrt[12]{6}-\frac{1}{N}\right)^6\right)^{0.52N}}, \tag{6.15}$$

even though it is achieved at the expense of accuracy.

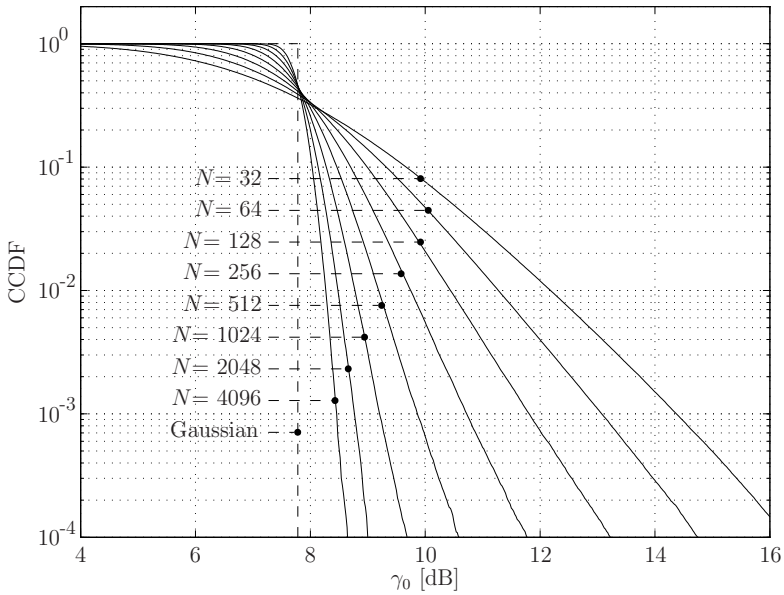

Figure 6.2: Probability that the raw CM of an N-subcarrier OFDM symbol exceeds a given threshold.

6.2 Performance of PAPR-reduced signals

In this section, the performance improvement capabilities of several well-known PAPR-reducing techniques are investigated by comparing the power spectral density and the error probability of conventional OFDM systems with those of PAPR-reduced OFDM systems [35]. Active constellation extension (ACE) [68], tone reservation (TR) [95], partial transmit sequences (PTS) [26] and selected mapping (SLM) [11] PAPR-reduction techniques are used.

In the simulations we set up an OFDM system with both QPSK and 16-QAM baseband modulation schemes. ACE and TR techniques are implemented as described in [68] and [34], respectively. PTS and SLM are implemented as in [50]. In TR approximately 4.3% of the subcarriers are reserved for PAPR-reduction. Those have been properly distributed to maximize the PAPR-reduction capabilities. In PTS $V = 3$ subblocks and $W = 4$ phase factors are used. For SLM, $U = 8$ different randomly generated phase sequences are used. As previously stated, we consider a soft limiter nonlinearity operating at IBO = 2dB, 4dB and 6dB and, in order to avoid aliasing the out-of-band distortion into the data bearing tones, an oversampling rate $L = 8$ has been used. Generally $L \geq 4$ is required in nonlinear multicarrier system simulations.

6.2.1 Active Constellation Extension

Performance improvement capabilities of ACE are strongly related to the constellation size. In general, larger constellation sizes result in less ACE flexibility. This phe-

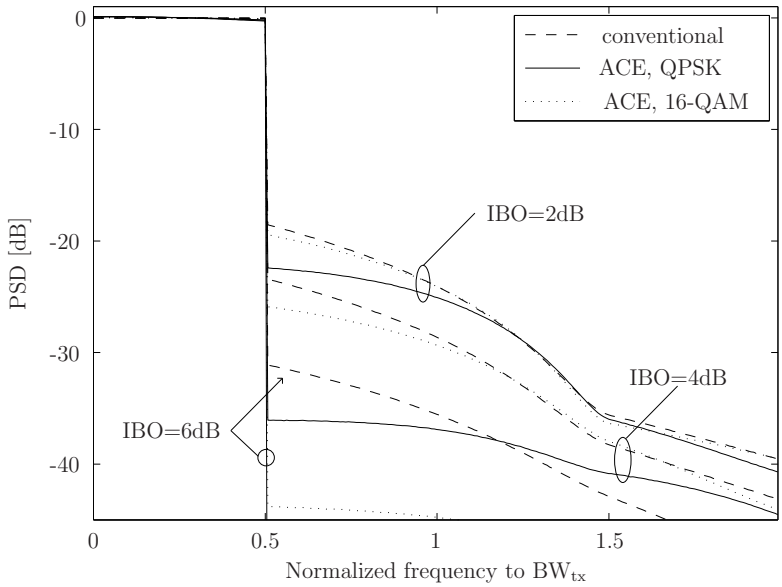

Figure 6.3: PSD of a conventional and an ACE-based PAPR-reduced OFDM system obtained when a soft limiter operating at several back-offs is present.

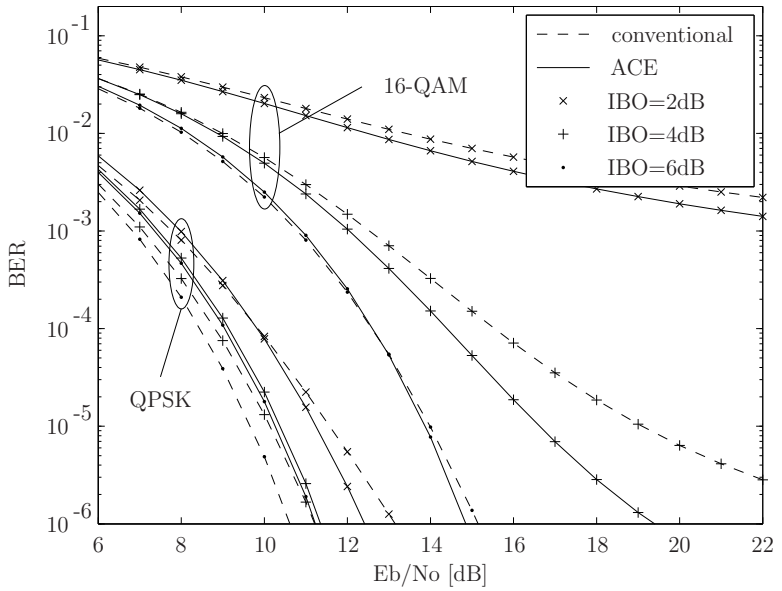

Figure 6.4: BER performance of a conventional and an ACE-based PAPR-reduced OFDM system obtained when a soft limiter operating at several back-offs is present.

nomenon can be observed in Figure 6.3 where the PSD of a conventional and ACE based PAPR-reduced OFDM systems are depicted. For all back-offs a larger reduction of the out-of-band radiation is achieved by using QPSK compared to 16-QAM. On the other hand, one should notice that, since by applying ACE the transmitted power increases, the power efficiency of the transmitted signal will decrease as the ACE flexibility increases. Figure 6.4 shows the BER performance improvement capabilities of ACE. When QPSK mapping is used a BER degradation occurs at IBOs of 4dB and 6dB, while a slight improvement is observed for Eb/No $\geq$ 10dB when IBO = 2dB is used. In case of using 16-QAM mapping the BER improvement is only noticed at IBOs of 2dB and 4dB. Hence, PAPR-reduction does not always lead to a BER performance improvement.

The PSD shown in Figure 6.3 was computed by means of periodogram, as the average of the PSD of the $L = 8$ oversampled signal in each OFDM symbol interval. This assures that the out-of-band radiation is computed just from the distortion term. In a practical situation a spectral outgrowth due to sharp transition between consecutive OFDM symbols would also occur. Figure 6.5 shows the PSD of a conventional and an ACE-based PAPR-reduced OFDM system in a rectangular window based transmission. As it can be observed, even though for large IBO (6dB) the out-of-band radiation introduced by the nonlinearity is considerably reduced when applying ACE (see Figure 6.3), in a practical situation the sharp transitions between consecutive OFDM symbols introduce a significant spectral regrowth.

6.2.2 Tone Reservation

Figures 6.6 and 6.7 show the PSD and the BER of a conventional and a TR-based PAPR-reduced OFDM system obtained when a soft limiter is used. TR performance is independent of the mapping, therefore so is the PSD in Figure 6.6. As in ACE, PAPR-reduction in TR is achieved at the expense of increasing the transmitted power, which has a direct influence on the BER performance. As it can be noticed in Figure 6.6, when QPSK is used the BER performance is only improved for high SNR and 2dB of IBO. In the other cases a conventional OFDM system with no PAPR-reduction achieves better performance. For 16-QAM the BER performance is always improved.

6.2.3 Partial Transmit Sequences

Figures 6.8 and 6.9 show the PSD and the BER of a conventional and a PTS-based PAPR-reduced OFDM system obtained when a soft limiter is used. It is useful to mention that a perfect knowledge of the side information at the receiver is assumed. Moreover, the extra power that would be required to transmit the side information is not taken into account. Hence, no loss of power efficiency occurs.

Let us consider the case where QPSK is used and the amplifier is set to operate at IBO = 6dB. From Figure 6.9 it can be noticed that the BER performance when PAPR-

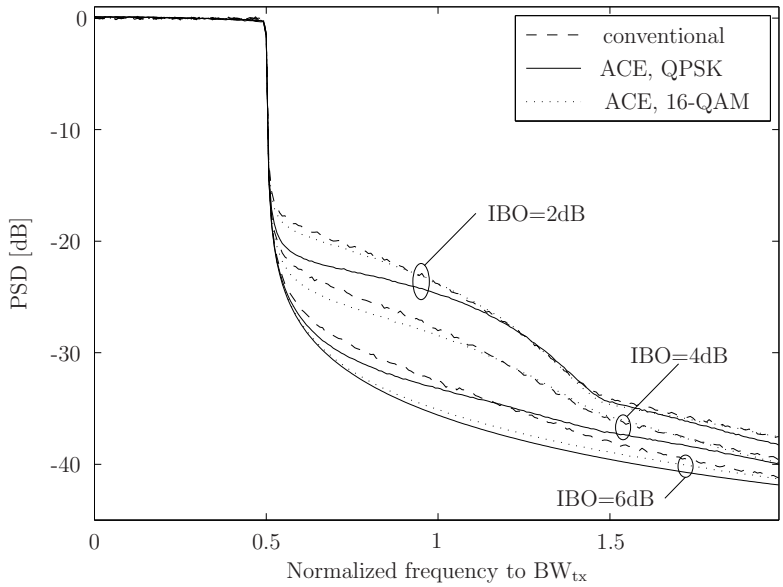

Figure 6.5: PSD of a conventional and an ACE-based PAPR-reduced OFDM system obtained when a soft limiter operating at several back-offs is present in a rectangular window based transmission.

reduction is done is scarcely improved compared to a conventional OFDM system. Therefore, if the loss of power efficiency due to the transmission of the side information was taken into account then the BER curves in Figure 6.9 would be shifted to the right causing a final degradation of the BER performance as occurred to ACE and TR. Moreover, since PTS requires the transmission of side information, an error on this side information would result in a large increase of the BER.

6.2.4 Selected mapping

The performance of a SLM-based PAPR-reduced OFDM system has also been simulated and similar results to those showed for PTS were found. Moreover, since both techniques have similar characteristics the previous discussion regarding the performance on an OFDM system employing PTS can also be applied to SLM. As in PTS, perfect knowledge of the side information at the receiver is assumed and no loss of power efficiency occurs since the extra power of the side information has not been taken into account.

6.2.5 Discussion

In this section the performance in terms of error probability and out-of band radiation of a conventional OFDM was compared with that of a PAPR-reduced OFDM system. From the presented work, it can be observed that the spectral outgrowth is reduced when applying PAPR-reduction, but a BER performance improvement only occurs

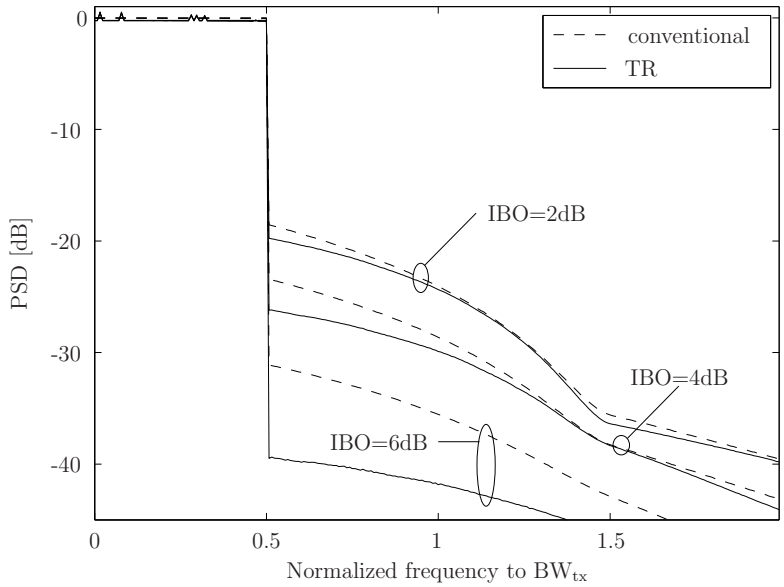

Figure 6.6: PSD of a conventional and an TR-based PAPR-reduced OFDM system obtained when a soft limiter operating at several back-offs is present.

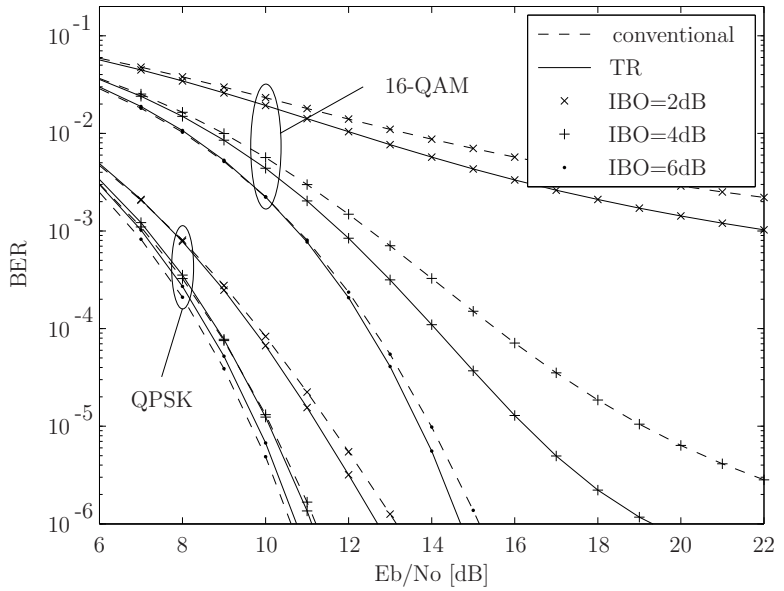

Figure 6.7: BER performance of a conventional and an TR-based PAPR-reduced OFDM system obtained when a soft limiter operating at several back-offs is present.

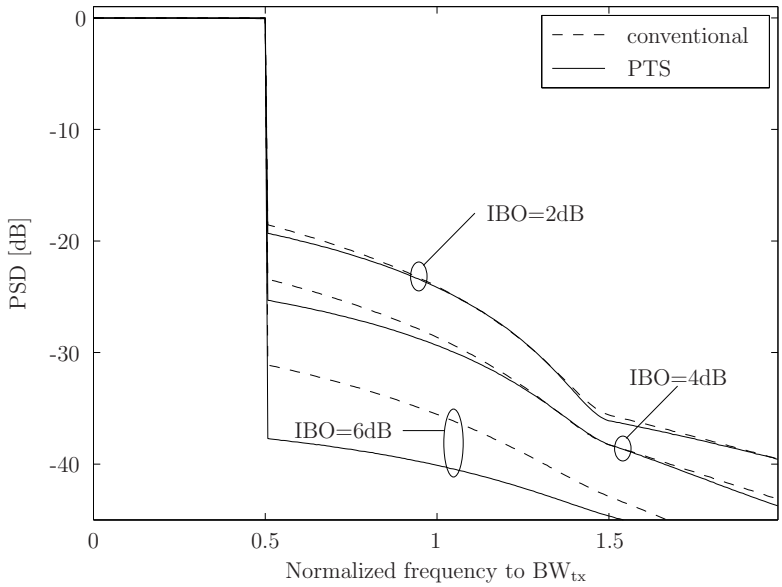

Figure 6.8: PSD of a conventional and an PTS-based PAPR-reduced OFDM system obtained when a soft limiter operating at several back-offs is present.

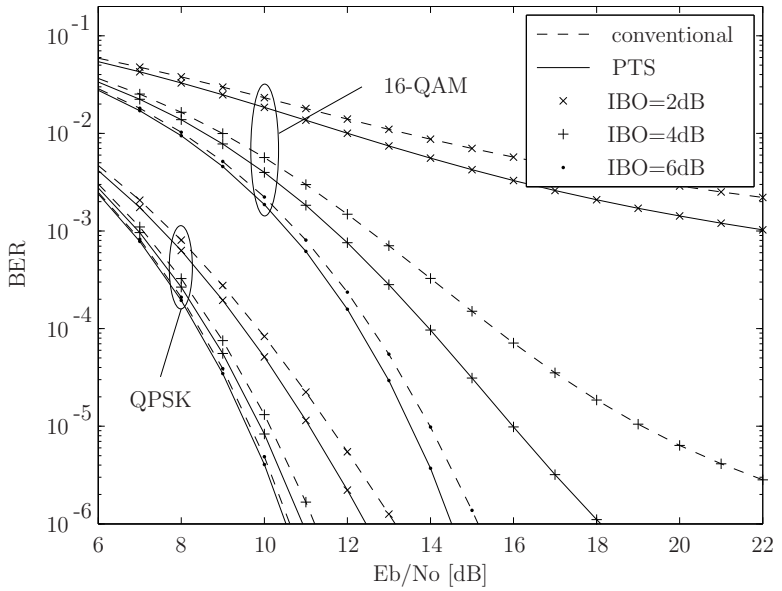

Figure 6.9: BER performance of a conventional and an PTS-based PAPR-reduced OFDM system obtained when a soft limiter operating at several back-offs is present.

when the effect of reducing the in-band distortion is more important than the loss of power efficiency. Therefore, in order to maximize the performance improvement of the techniques it is important that the most appropriate signal metric is used. This will be investigated in the remainder of this chapter.

6.3 Performance of sub-Gaussian distributed OFDM signals

In the previous chapters, the OFDM signal is always assumed to be complex Gaussian distributed. Figure 6.10 shows the normalized kurtosis of the real and imaginary parts of an OFDM signal, denoted as $s_n^{(r)}$ and $s_n^{(i)}$ respectively, with different number of subcarriers. It can be observed that kurtosis is always negative, which means that the OFDM signal is sub-Gaussian distributed. In this section, the work undertaken by Dardari et al. [29] is extended to consider sub-Gaussian distributed OFDM signals [33].

Let us model the OFDM system as a stochastic process $\mathcal{S}$ such that each symbol $s^{(i)}(t)$, $t \in [0, T_s)$, is a different realization of $\mathcal{S}$. Let us define $s_d^{(i)}(t)$ as the output signal of a nonlinear amplifier with input signal $s^{(i)}(t)$. Conventional receivers only process the part of $s_d^{(i)}(t)$ that corresponds to a linear amplification of $s^{(i)}(t)$, while the remainder of the signal is seen as distortion. Therefore, the output signal can be expressed without any Gaussianity assumption as

$$s_d^{(i)}(t) = \alpha^{(i)} s^{(i)}(t) + d^{(i)}(t), \tag{6.16}$$

where $d^{(i)}(t)$ is the distortion term and $\alpha^{(i)}$ is a complex amplification term that depends on the outcome i of $\mathcal{S}$. The value of $\alpha^{(i)}$ that minimizes the mean-squared error (MSE) of the unbiased input and output signals is found to be [79]

$$\alpha^{(i)} = \frac{\langle s_d(t), s(t) \rangle_i - \langle s_d(t) \rangle_i \langle s(t) \rangle_i^*}{\langle |s(t)|^2 \rangle_i - \langle s(t) \rangle_i \langle s(t) \rangle_i^*} \tag{6.17}$$

where $\langle x(t), y(t) \rangle_i = \frac{1}{T_s} \int_0^{T_s} x^{(i)}(t)(y^{(i)}(t))^* dt$ is the inner product of $x^{(i)}(t)$ and $y^{(i)}(t)$, and $\langle x(t) \rangle_i = \frac{1}{T_s} \int_0^{T_s} x^{(i)}(t) dt$ is the time average of $x^{(i)}(t)$.

Let us first assume that the number of subcarriers in the OFDM system is large enough. In this case the transmitted signal can be modeled as a complex Gaussian stationary process, $\mathcal{S} \sim \mathcal{N}(0, \sigma^2/2) + j \cdot \mathcal{N}(0, \sigma^2/2)$ where σ^2 is the transmitted signal power. For Gaussian processes, wide-sense stationary (WSS) and strict-sense stationary (SSS) are equivalent [83], therefore it is referred to as just stationary. According to [79] if the input to a memoryless system is a SSS process, the resulting output is also SSS. Therefore, for an OFDM system with large number of subcarriers the signal at the output of the nonlinearity can be modeled as a SSS (non-Gaussian) process. A

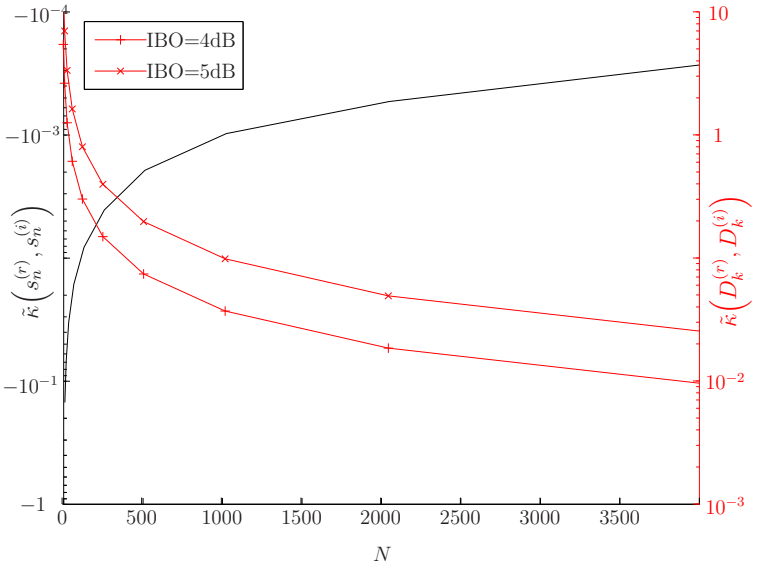

Figure 6.10: Normalized kurtosis of the real and imaginary parts of an OFDM signal with different number of subcarriers (black). Normalized kurtosis of the real and imaginary parts of the in-band distortion term introduced by a soft limiter operating at different back-offs (red).

consequence of the stationarity property is that the term $\alpha^{(i)}$ is, in fact, independent of t. As a result, within an OFDM symbol it generates a constant attenuation and rotation of the constellation. Moreover, for large number of subcarriers the processes at the input and output of the nonlinearity are also covariance ergodic [79]. Therefore, $\alpha^{(i)}$ does not depend on the realization.

Notice that by considering the previous properties, it follows that $\langle |s(t)|^2 \rangle_i = R_{ss}(0)$ and $\langle s_d(t), s(t) \rangle_i = R_{s_d s}(0)$, where $R_{ss}(\tau)$ and $R_{s_d s}(\tau)$ denote autocorrelation and cross-correlation, respectively. As a result, the term α is constant and equal to $\alpha = R_{s_d s}(\tau)/R_{ss}(\tau)$, for all τ. Moreover, the distortion term is uncorrelated with the input signal. This means that the effect of the nonlinearity reduces to a constant attenuation and rotation of the constellation plus the addition of an uncorrelated distortion term [29].

Let us now assume that the OFDM system employs a low number of subcarriers. Here the Gaussianity assumption does not hold. Moreover, the time averages of different realizations of $\mathcal{S}$ may not only be different than zero but also different to each other. Also, the average power of each realization may be different than σ^2. Therefore, $\mathcal{S}$ is not ergodic. In such case, the complex amplification term $\alpha^{(i)}$ will be different for different OFDM symbols.

Another consequence of employing a low number of subcarriers is that $\mathcal{S}$ in non-stationary. Notice that this means that the relation between the input, $s(t)$, and

output, $s_d(t)$, processes should be written as [29]

$$s_d(t) = \alpha(t)s(t) + d(t). \tag{6.18}$$

This means the constellation will not be constantly attenuated and rotated within an OFDM symbol, instead warping will occur. In practice, the constellation warping is very small and, as a result, it can be neglected. Therefore, one can assume that the complex gain term is constant within an OFDM and compute it according to (6.17).

When the number of subcarriers in the OFDM system is low, the process $\mathcal{S}$ is not only non-Gaussian distributed but also it is non-ergodic and non-stationary. The stationarity and ergodicity properties of $\mathcal{S}$ are independent of the fact that it is sub-Gaussian distributed. However, for the sake of simplicity, in this thesis the OFDM signals employing low number of subcarriers are referred to as just *sub-Gaussian distributed OFDM signals*.

From (6.16) the nonlinear distortion term introduced to an OFDM symbol can be computed without any assumption on the Gaussianity of the signal as

$$d^{(i)}(t) = s_d^{(i)}(t) - \alpha^{(i)}s^{(i)}(t), \tag{6.19}$$

where $\alpha^{(i)}$ is defined in (6.17). Figure 6.11 shows the average, minimum and maximum power of the distortion term introduced by a soft limiter nonlinearity operating at several IBOs to an OFDM system employing 16-QAM and different number of subcarriers. As it can be observed, for all number of subcarriers the same average power of the distortion term is introduced, nevertheless a larger variation occurs for lower number of subcarriers.

This has a direct consequence on the spectrum and error rate characteristics of an OFDM signal undergoing a nonlinear amplifier. On one hand, since the average power of the distortion term is independent of the number of subcarriers and the mapping scheme, the same average interference is generated to neighboring systems regardless of the system configuration. This can be observed in Figure 6.12 where the PSD of an OFDM system employing different number of subcarriers is shown. Nevertheless, for low number of subcarriers where the power of the distortion introduced by different OFDM symbols fluctuates significantly around the average, it results that some OFDM symbols generate interference levels significantly larger than the average. On the other hand, since the distribution of the power of the distortion term varies with the number of subcarriers, OFDM systems with different number of subcarriers have different error probabilities in the presence of nonlinearities. For large number of subcarriers, the power of the distortion term introduced to different OFDM symbols is almost constant. Therefore, the BER performance in nonlinear AWGN channels can be computed analytically as it was shown in Chapter 4. For lower number of subcarriers, where a larger variation of the power of the distortion term occurs, the analytical error probability in nonlinear AWGN channels must be computed by considering the distribution of the

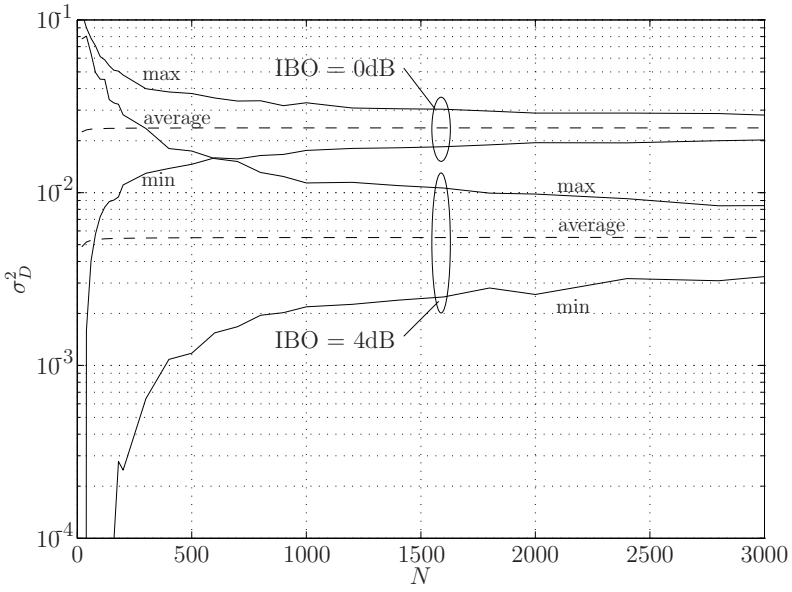

Figure 6.11: Average, minimum and maximum power of the distortion term introduced to an OFDM system with different number of subcarriers when a soft limiter operating at IBO=0dB and IBO=4dB is present.

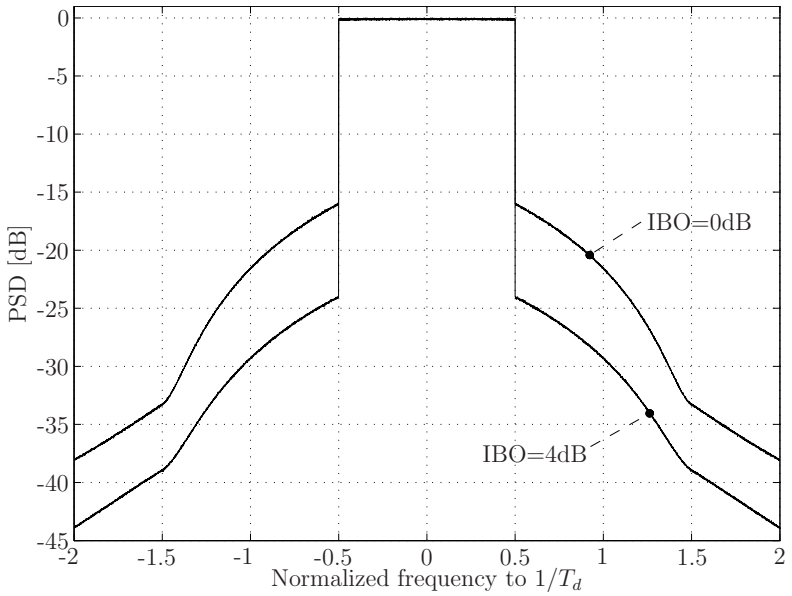

Figure 6.12: PSD of an OFDM system employing different number of subcarriers when a soft limiter nonlinearity is present.

power of the distortion term as,

$$P_e = \int_0^\infty P_e^{(G)}\left(\frac{\sigma^2}{\sigma_W^2+\sigma_D^2}\right) f_D\left(\sigma_D^2\right)\ d\sigma_D^2 \tag{6.20}$$

where $f_D\left(\sigma_D^2\right)$ is the probability density function of the variance of the distortion term and $P_e^{(G)}\left(\frac{\sigma^2}{\sigma_W^2+\sigma_D^2}\right)$ is the probability of error assuming a received signal power of σ^2 and a Gaussian noise of power $\sigma_W^2+\sigma_D^2$.

The reader should notice that for large number for subcarriers, where the Bussgang theorem holds, the variance of the distortion term is constant and, as a result,

$$f_D\left(\sigma_D^2\right) = \delta\left(\sigma_D^2 - E[\sigma_D^2]\right). \tag{6.21}$$

Therefore equation (6.20) reduces to $P_e = P_e^{(G)}\left(\frac{\sigma^2}{\sigma_W^2+\sigma_D^2}\right)$, where $\sigma_D^2 = E[\sigma_D^2]$. As a result, one can use the analytical formulation in Chapter 4 to compute the error probability in nonlinear AWGN channels.

As shown in Appendix B sub-Gaussian distributed OFDM signals undergoing a nonlinear amplifier have larger error probabilities than Gaussian distributed ones. In practice, this means that the error rate of an OFDM system with low number of subcarriers is higher than that of an OFDM system with large number of subcarriers. This can be observed in Figures 6.13 and 6.14 where the BER performance of an OFDM system with different number of subcarriers undergoing a nonlinear amplifier is shown. 16-QAM mapping and a soft limiter nonlinearity operating at 3dB and 5dB of IBO are used. Moreover, the analytical BER performance of a Gaussian distributed OFDM signal computed by means of the Bussgang theorem is also shown. This corresponds to the case of an OFDM system employing infinite number of subcarriers and, as shown in Appendix B, it is the lower bound for the BER performance.

The previous formulation was derived assuming that the in-band distortion term follows a Gaussian distribution. According to [29], since the nonlinear distortion noise component is the sum of N identically distributed random variables it is reasonable to assume it to be Gaussian distributed. Figure 6.10 shows the kurtosis of the real and imaginary parts of the in-band distortion of an OFDM system with different number of subcarriers. As it can be observed except for low number of subcarriers (< 16) kurtosis is moderate/low, which means that the Gaussian assumption holds.

6.4 Discussion on the signal metrics

So far a study of the effect of nonlinearities in OFDM systems has been presented. Moreover, the two signal metrics have been defined and used to evaluate the envelope

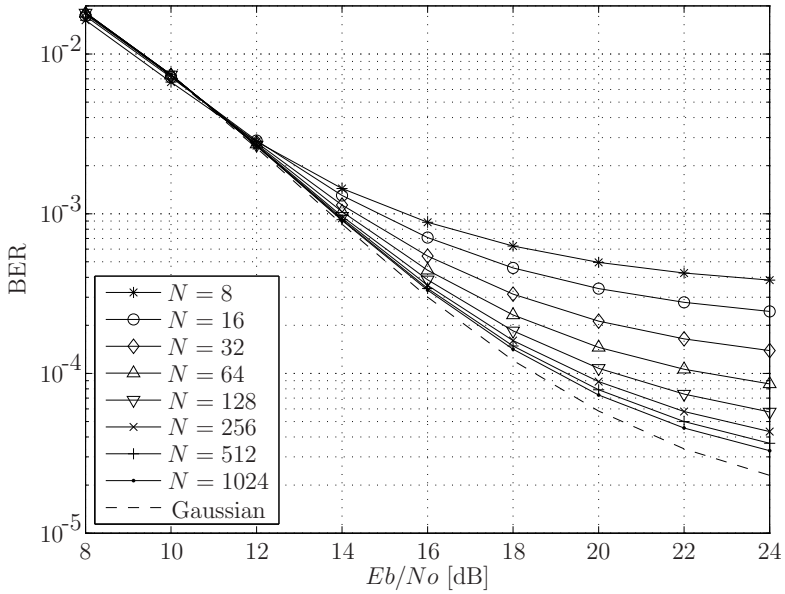

Figure 6.13: Bit error rate versus Eb/No of a 16-QAM OFDM system with different number of subcarriers when a soft limiter nonlinearity operating at IBO=3dB is present.

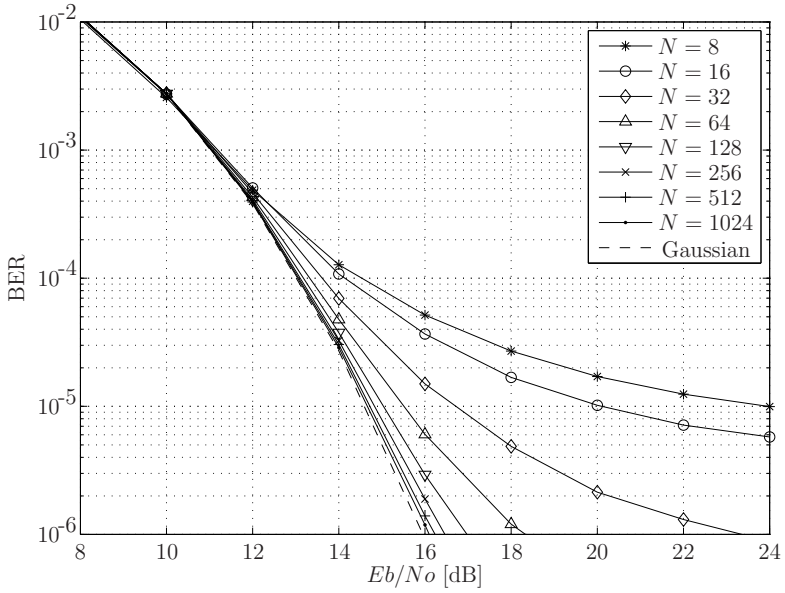

Figure 6.14: Bit error rate versus Eb/No of a 16-QAM OFDM system with different number of subcarriers when a soft limiter nonlinearity operating at IBO=5dB is present.

fluctuations of the transmitted signal. Quantifying the envelope fluctuations is twofold. On one hand it should guide us through the design of techniques to reduce the envelope fluctuations, hence, making the OFDM systems less sensitive to nonlinearities and, on the other hand, it should allow us to predict the amount of power back-off required to satisfy a given performance. Therefore, the amount of distortion introduced by the nonlinearity and the signal metrics should be closely related. In this section, the previous analysis is used as a framework for discussing the suitability of the signal metrics [33].

Different OFDM symbols have different PAPR/CM and when passed through a nonlinearity they result in different distortion terms. In order to determine how much information the knowledge of the PAPR/CM characteristics of the signal provides about the nonlinear distortion one should see them as random variables and analyze their dependencies. An intuitive way to determine the relation between the signal metric and the variance of the distortion term is by showing the scatter plot for various OFDM systems with different configurations. This is shown in Figure 6.15 for $N = \{16, 64, 1024\}$, and QPSK and 64-QAM. As it can be observed, the variance of the distortion term introduced to an OFDM symbol is somehow related to its CM. On the other hand, for PAPR no clear relation is observed.

To determine the dependence between two random variables X and Y in a more mathematically rigorous way one can compute their mutual information,

$$I(X;Y) = \sum_{y\in Y}\sum_{x\in X} p_{XY}(x,y)\ln\left(\frac{p_{XY}(x,y)}{p_X(x)\,p_Y(y)}\right). \tag{6.22}$$

Where $p_{XY}(x,y)$ is the joint PDF of X and Y, and $p_X(x)$ and $p_Y(y)$ are the marginal PDF of X and Y respectively. Figure 6.16 shows the mutual information between the signal metrics and the distortion term introduced by a nonlinearity. Two types of nonlinearities, namely soft limiter and Saleh, operating at different back-offs are considered. To compute the mutual information, an OFDM system employing different number of subcarriers in the range $N = [8, 2048]$ and different mapping schemes (QPSK, 16-QAM and 64-QAM) is used. As it can be observed, the mutual information between CM and the variance of the distortion term, denoted as $I(\sigma_D^2;\mathrm{CM})$, is generally larger than the mutual information between PAPR and the variance of the distortion term, denoted as $I(\sigma_D^2;\mathrm{PAPR})$. This means that CM is more related to the distortion introduced by the nonlinearity than PAPR. In fact $I(\sigma_D^2;\mathrm{PAPR})$ is only larger than $I(\sigma_D^2;\mathrm{CM})$ for a soft limiter nonlinearity operating at high back-offs. On the other hand, for a Saleh nonlinearity $I(\sigma_D^2;\mathrm{CM})$ is significantly larger than $I(\sigma_D^2;\mathrm{PAPR})$ even at high back-offs.

Let us now address some further discussions regarding the suitability of the signal metrics. It can be observed from the analysis of the distortion term that (i) the average distortion term introduced to an OFDM signal is independent of N and that (ii) as N increases the variation of the power of the distortion term introduced to each OFDM

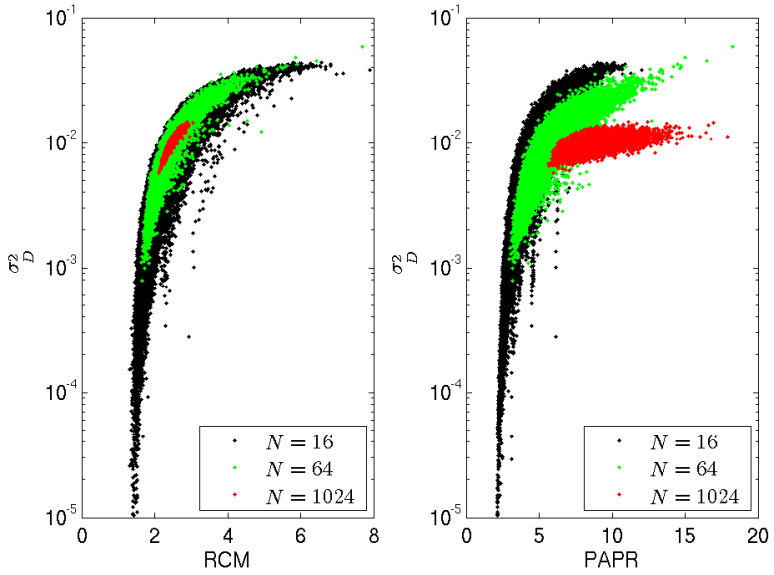

Figure 6.15: Scatter plot of the variance of the in-band distortion introduced to different OFDM symbols versus the RCM/PAPR of the corresponding OFDM symbol.

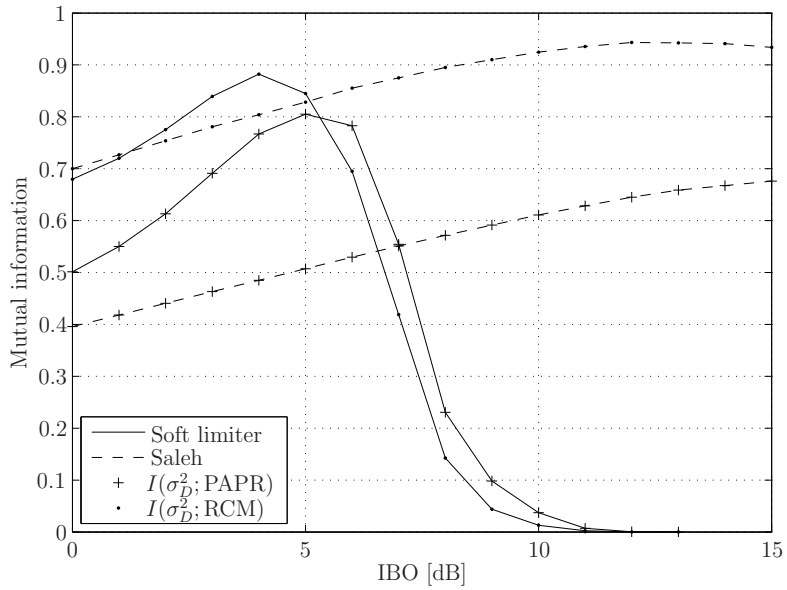

Figure 6.16: Mutual information between the signal metrics and the variance of the in-band distortion term introduced by the nonlinearity.

symbol decreases.

From the analysis of the signal metrics it was shown that CM of an OFDM symbol is a number that oscillates around $\sqrt{6}$ and that the variation of CM of each OFDM symbol around this value is smaller as N increases. This is depicted in Figure 6.17 where the average, minimum and maximum values of the signal metrics of an OFDM system employing 16-QAM and different number of subcarriers is shown. The reader should note that the information provided from the analysis of CM of an OFDM system is the same as that obtained from analyzing the distortion term: (i) both the average CM and average distortion are independent of the number of subcarriers and (ii) the variation of both terms around their average decreases as N increases. As a result, if all previous considerations are taken into account, it seems reasonable to state that CM is a suitable metric of the envelope fluctuations of multicarrier systems.

It is widely known that PAPR of an OFDM signal increases with N. In fact, as it can be observed in Figure 6.17 an OFDM system with larger number of subcarriers has a larger average PAPR[2]. Moreover the range of values that PAPR of an OFDM symbol may take also increases with N. Notice, that these are not the same conclusions that we draw from analyzing the distortion term. Since PAPR increases with the number of subcarriers one would expect that a worse performance in both PSD and BER is obtained. Nevertheless, the PSD is the same while BER improves. Thus, it seems that the effect of a nonlinearity on an OFDM signal is not clearly related to its PAPR.

Another important consideration regarding the discussion of the suitability of the two metrics refers to the ability to predict the PA power de-rating. In [1, 2], after analyzing certain OFDM-type signals, it is shown that CM predicts PA power de-rating more accurately than PAPR. This conclusion was drawn from empirical analysis based on measurements on real signals, however, the previously presented formulation can be used to explain it. Power de-rating refers to the amount of back-off that is required in a power amplifier in order to meet a given ACLR. Since the spectrum of the transmitted signal is independent of the number of subcarriers, it results that ACLR is also independent of N. Therefore, if the signal metric is expected to predict ACLR, it must also be independent of N. Otherwise we will not have a bijective prediction function. As it was previously shown, this is accomplished by CM but not by PAPR.

6.5 Considerations for wireless communications systems

In this chapter we provided an analysis of the effect of nonlinearities in OFDM systems that is based on the widely known Bussgang theorem but extended to sub-Gaussian

[2]Maximum PAPR is not shown because it is much larger than the average.

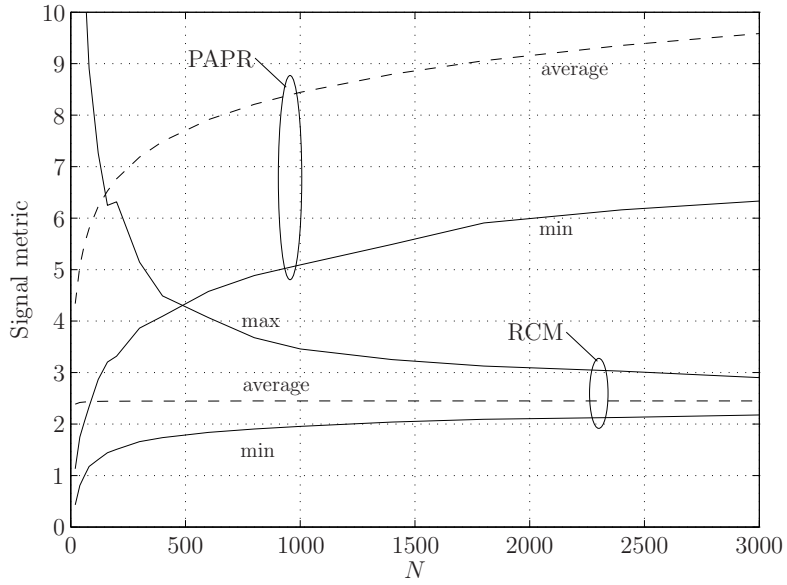

Figure 6.17: Average, minimum and maximum PAPR/RCM of an OFDM system employing 16-QAM and different number of subcarriers.

distributed signals [33]. As it was shown, performance is strongly influenced by the number of subcarriers.

OFDM is used for both the downlink and the uplink of many broadband and cellular wireless communication systems. In the downlink, the number of subcarriers is typically large and therefore the Gaussianity assumption holds. For instance, in Digital Video Broadcasting (DVB) [42] 6817 subcarriers are used in the 8K mode and 1705 subcarriers are used in the 2K mode. In a cellular system, OFDMA may be used to multiplex different user streams. Nevertheless, since the downlink signal is formed by all subcarriers and N is typically large, the Gaussianity assumption is also valid. For instance, in WINNER [55] 416 and 1664 subcarriers are considered for frequency-division duplex (FDD) and time-division duplex (TDD) modes, respectively. According to the Bussgang theorem if the signal is Gaussian distributed the effect of a nonlinearity reduces to a constant rotation and attenuation of the constellation plus the addition of a distortion noise. In practice, the term α is automatically compensated by the receiver through the channel equalization block. Therefore, only the distortion term is responsible for the performance degradation. Another implication from Bussgang is that the power of the distortion term introduced to each OFDM symbol is constant. Therefore, all OFDM symbols make equal contributions to the out-of-band radiation.

In the OFDMA uplink, a transmitter may be assigned one or more group of subcarriers, namely subchannels. In such a case Gaussianity will depend on the size of the subchannels. Generally the number of subcarriers per subchannel is low and, thus,

the Gaussianity assumption does not hold. For instance, in WINNER the total available bandwidth is divided into 52(104) subchannels of 8(16) subcarriers each in the FDD(TDD) mode [55]. For sub-Gaussian distributed signals the OFDM symbol at the output of the nonlinearity can still be computed as an attenuated and rotated version of the input symbol plus a distortion term. However, since the Bussgang theorem does not hold and, moreover the OFDM process is non-stationary and non-ergodic, neither the attenuation/rotation nor the power of the distortion term are constant among different OFDM symbols. This implies that the error probability of sub-Gaussian distributed signals is further increased compared to that of Gaussian distributed ones. Another consequence is that the average interference introduced to neighboring communication systems is the same regardless of the system configuration. Nevertheless, some OFDM symbols generate interference levels significantly larger than the average. This is of special relevance, if we take into account that not only low back-offs should be used in the handset to increase the battery life but also that in order to reduce the cost of the handsets power amplifiers with poor linearity characteristics are employed.

Chapter 7

Tone reservation technique

In this chapter a study of the TR technique for both PAPR and CM reduction is provided. The chapter is divided into two major sections. First, a low complexity suboptimal method to compute the complex amplitude of the correcting tones in PAPR-reduction is presented. As it will be shown, the proposed method achieves higher PAPR-reduction than previously suggested suboptimal TR-based methods. In the second part of this chapter TR technique is reformulated for CM-reduction. Here, optimal and low-complexity suboptimal solutions are derived. Moreover, since both suboptimal implementations for PAPR and CM reduction are similar, a comparison of the performance improvement capabilities of both methods is presented. Simulation results show that larger performance improvement is obtained by using CM.

7.1 Efficient and low-complexity PAPR-reduction by TR

The optimal complex amplitude of the peak-reducing tones can be obtained by solving a quadratically constrained quadratic program, which is a type of convex optimization problem [94]. Since finding the exact solution to such kind of problem is computationally demanding, an iterative way to reduce PAPR was also introduced in [94]. This solution is less complex, but on the other hand it is not optimal. Nevertheless, as stated in [69], the iterative PAPR-reducing method is still computationally complex because of its slow convergence and, in turn, a faster converging iterative algorithm was proposed. Another iterative method to compute the peak-reducing tones was proposed in [44]. This is essentially a specific case of [94] and has slower convergence speed.

This section presents and evaluates a new way to compute the peak-reducing tones [34]. The peak-reducing tones are obtained by computing a peak-reducing signal from a clipped version of the original OFDM symbol. Similar versions of this algorithm can be found in [94] and [44]. However, here the smart gradient-project (SGP) algorithm [68] is used to reduce the convergence time. Moreover, by exploiting the characteristics

of TR a new technique that can dramatically reduce the computational complexity requirements is proposed. Simulation results show that this method achieves higher PAPR reduction than the other methods in the literature [44, 69, 94].

7.1.1 Description of the method

Consider $\mathbf{S} \in \mathbb{C}^N$ as an OFDM vector in the frequency domain consisting of M information symbols at subcarrier positions $\mathcal{P}_M = \{p_1, p_2, \ldots, p_M\}$ and $R = N - M$ zeros at subcarrier positions $\mathcal{Q}_R = \{q_1, q_2, \ldots, q_R\}$, where $\mathcal{P}_M$ and $\mathcal{Q}_R$ are disjoint sets. Then, the OFDM symbol in the time domain is computed as

$$s_n = \frac{1}{\sqrt{N}} \sum_{k \in \mathcal{P}_M} S_k e^{j2\pi kn/LN}, \qquad n = 0, 1, \ldots, LN-1, \tag{7.1}$$

where L is the oversampling factor. Let us recall from Chapter 2 that (7.1) can be computed by means of a scaled length-LN IFFT of the zero padded symbol vector $\mathbf{S}$ as

$$\mathbf{s} = L\sqrt{N} \cdot \mathrm{IFFT}_{LN}\{\mathbf{S}^{\mathrm{zp}}\} \tag{7.2}$$

where without any loss of generality $\mathbf{S}^{\mathrm{zp}}$ is defined in this chapter as

$$\mathbf{S}^{\mathrm{zp}} = [S_0, S_1, \ldots, S_{N-1}, \underbrace{0, 0, \ldots, 0}_{N(L-1)}]. \tag{7.3}$$

TR consists in adding a peak-reducing signal $\mathbf{C}^{(\mathbf{s})} \in \mathbb{C}^N$ with zeros at the data bearing tones in $\mathbf{S}$, i.e. $\mathcal{P}_M$, and R peak-reducing tones at the subcarrier positions defined by $\mathcal{Q}_R$. The time domain signal can be described as

$$\begin{aligned} \overline{s}_n &= s_n + c_n^{(\mathbf{s})} \\ &= s_n + \frac{1}{\sqrt{N}} \sum_{k \in \mathcal{Q}_R} C_k^{(\mathbf{s})} e^{j2\pi kn/LN}, \end{aligned} \tag{7.4}$$

where the notation $C_k^{(\mathbf{s})}$ is used to stress that the complex amplitude of each peak-reducing tone is computed according to the shape of the time domain OFDM symbol $\mathbf{s}$. After computing the values $C_k^{(\mathbf{s})}$; $\forall k \in \mathcal{Q}_R$, the peak-reducing signal in the time domain could be computed by means of the IFFT as shown previously. However, since the complexity of an IFFT is $\mathcal{O}(LN \log LN)$ and the number of peak-reducing tones is $R << LN$, computing the time domain peak-reducing signal as shown in (7.4) instead of using the IFFT is less computationally demanding. To implement (7.4), the time domain representation of the peak-reducing tones is computed at initialization as

$$w_{n,\,k} = \frac{1}{\sqrt{N}} e^{j2\pi q_k n/LN} \qquad k = 1, \ldots, R;\ n = 0, \ldots, LN-1 \tag{7.5}$$

and, subsequently, at run time, first, the complex amplitude of each peak-reducing tone is computed, i.e. $C_{q_k}^{(\mathbf{s})},\ k = 1, \ldots, R$, and then the peak-reducing signal is found as

$$c_n^{(\mathbf{s})} = \sum_{k=1}^{R} C_{q_k}^{(\mathbf{s})} w_{n,\,k}. \tag{7.6}$$

Clipping is a powerful operation to reduce the peak factor of a signal. As in [44,94] a clipping device is used to compute the peak-reducing signal. The proposed method is as follows:

1. Clip the OFDM data symbol s_n to obtain the clipped OFDM data symbol $\tilde{s}_n$,

$$\tilde{s}_n = \begin{cases} s_n & \text{if } |s_n| \leq A \\ A\dfrac{s_n}{|s_n|} & \text{otherwise} \end{cases} \tag{7.7}$$

   where A is the clipping threshold.

2. Compute the unconstrained peak-reducing signal as $\tilde{c}_n = \tilde{s}_n - s_n$.

3. Compute the complex amplitude of the peak-reducing tones by projecting $\tilde{c}_n$ onto each peak reducing tone $\mathbf{w}_k = [w_{0,\,k}, \ldots, w_{LN-1,\,k}]^{\mathsf{T}}$,

$$C_{q_k}^{(\mathbf{s})} = \sum_{n=0}^{LN-1} \tilde{c}_n w_{n,\,k}^{*} \qquad k = 1, \ldots, R. \tag{7.8}$$

4. Compute the peak-reducing signal as formulated in (7.6).

Let us recall from Chapter 4 that if an OFDM signal s_n with a sufficiently large number of subcarriers is fed to a nonlinearity, then the output signal $\tilde{s}_n$ can be written as the sum of a scaled input replica and an uncorrelated distortion term as [29]

$$\tilde{s}_n = \alpha s_n + d_n, \qquad \text{where } \alpha = \frac{E[\tilde{s}_n s_n^{*}]}{E[|s_n|^2]}. \tag{7.9}$$

To determine the output signal $\tilde{s}_n$ at the peak-reducing tone positions let us, first, take the DFT of (7.9) as

$$\tilde{S}_k = \alpha S_k + D_k, \qquad k = 0, 1, \ldots, LN-1, \tag{7.10}$$

where D_k is the distortion term introduced to the k-th subcarrier, and α is computed as in (7.9). Now, notice that at the peak-reducing tone positions the complex amplitude of the input subcarriers is zero, thus,

$$\tilde{S}_{q_k} = D_{q_k}, \qquad k = 1, \ldots, R. \tag{7.11}$$

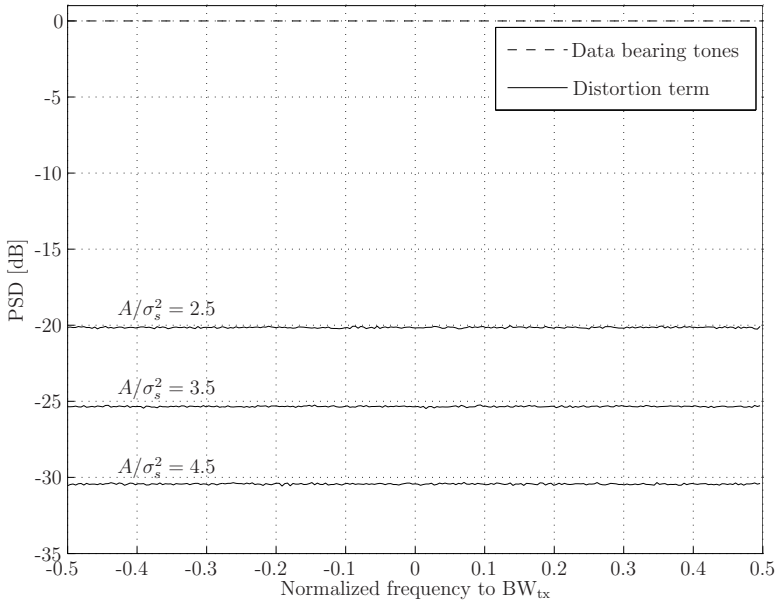

Figure 7.1: Distortion term introduced by a clipping device with different clipping levels.

Figure 7.1 shows power spectral density of the in-band distortion term introduced by a clipping device operating at several practical clipping levels to an OFDM system. It can be observed that the power spectral density of the distortion term is much lower than the power spectral density of the data bearing tones. Thus the peak-reducing tones will have a much lower amplitude than the data bearing tones. In order to maximize the peak power reduction it is important to rescale all the peak-reducing tones. The optimal scaling factor can be determined by solving the following minimax optimization problem

$$\mu_{\text{opt}} = \arg\min_{\mu} ||\mathbf{s} + \mu\mathbf{c}^{(\mathbf{s})}||_{\infty} \tag{7.12}$$

where $\mathbf{s} = [s_0, \ldots, s_{LN-1}]$ and $\mathbf{c} = [c_0, \ldots, c_{LN-1}]$. However, finding the optimal scaling factor is computationally demanding. In [68] a reduced complexity approach, denoted as smart gradient-project (SGP), was proposed. In this section the SGP approach is used since it obtains a good approximation of the optimal solution. Finally, the peak-reduced signal $\overline{s}_n$ becomes

$$\overline{s}_n = s_n + \mu c_n^{(\mathbf{s})}. \tag{7.13}$$

Iterative implementation

The above described procedure can be applied iteratively to achieve larger peak reductions. The block diagram of the iterative implementation of the method is depicted in Figure 7.2.

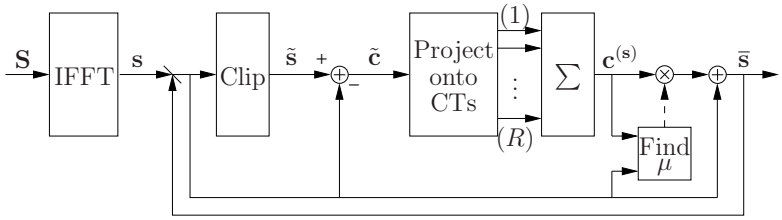

Figure 7.2: Block diagram of the iterative implementation of the proposed suboptimal PAPR-reducing method.

Simulation results suggest that at most three iterations are required to achieve maximum peak power reduction. Note that (7.11) only holds at the first iteration since at the other iterations the peak-reducing tones at the input of the clipping device have an amplitude different than zero. Nevertheless, computing the scaling factor μ is still necessary.

Practical considerations

Some important aspects have to be considered on the implementation of the method: which upsampling factor to use and what should be the clipping level A.

In this method the distortion term at the output of the clipping device is used to reduce the peak power. When an OFDM signal is fed to a nonlinear device (e.g. a clipping device) a distortion term with a much larger bandwidth than the bandwidth of the information signal is generated. In order to assure that the complex amplitude of the peak-reducing tone is computed properly it is important to avoid aliasing the out-of-band distortion into the peak-reducing tone positions. This can be achieved by sufficiently oversampling the signal (typically $L \geq 4$) at the input of the nonlinear device. Therefore, an oversampling $L \geq 4$ must be used in the above described method to compute the complex amplitude of the peak-reducing tones.

Another important aspect is to properly select the clipping level in (7.7) to achieve the maximum PAPR reduction. The appropriate value depends on the number of subcarriers in the OFDM system, the peak-reducing tone distribution and the modulation scheme. Therefore, it has to be obtained by means of simulation.

Computational complexity

If FFT/IFFT were used to compute the peak-reducing signal, the computational complexity would be $\mathcal{O}(LN \log LN)$. However, the complexity is dramatically decreased by, first, just computing the frequency representation of $\tilde{c}_n$ at the peak-reducing tone positions and, second, computing the weighted sum of the time domain representation of the peak-reducing tones. The first requires RLN complex multiplications and $RL(N-1)$ complex additions, while the second requires RLN complex multiplications

and $(R-1)LN$ complex additions. This results in a total of $2RLN$ complex multiplications and $L(2RN-R-N)$ complex additions per iteration. Notice that this means that the complexity requirements increase linearly with the number of tones, i.e. $\mathcal{O}(LN)$. Therefore, since the complexity associated with SGP is also of order $\mathcal{O}(LN)$ [68], the complexity of the proposed method becomes of order $\mathcal{O}(LN)$. Note that at initialization the time domain representation of the peak-reducing tones has to be computed and it has not been taken into account as a complexity requirement.

7.1.2 Simulation results

Several setups are used to evaluate the performance of the proposed method, i.e. modulation schemes and peak-reducing tone distributions. The number of peak-reducing tones has been chosen to be $R = 11$ and $R = 21$ with the following subcarrier distributions:

$$\begin{aligned}\mathcal{Q}_{11} &= [5, 25, 54, 102, 125, 131, 147, 200, 204, 209, 247],\\ \mathcal{Q}_{21} &= [5, 11, 25, 33, 54, 71, 90, 102, 108, 125, 131,\\ &\quad 138, 147, 163, 183, 200, 204, 209, 230, 247, 253].\end{aligned}$$

The total number of subcarriers in all cases is $N = 256$ and the number of data bearing tones is, thus, M=235 and M=245 for R=11 and R=21, respectively. The peak-reducing tone distribution for the $R = 11$ case, i.e. $\mathcal{Q}_{11}$, is the same that was used in [69]. This distribution has been specifically used for fair comparison purposes. For $R = 21$, the extra peak-reducing tones have been chosen randomly. All previously described subcarrier distributions have been evaluated with three different modulation schemes, namely QPSK, 16-QAM and 64-QAM.

Table 7.1 summarizes the appropriate clipping levels to achieve a maximum PAPR reduction for each of the previously described setups. The values have been obtained from extensive simulations.

Clipping level [dB]	QPSK	16-QAM	64-QAM
$\mathcal{Q}_{21}$	4.6	4.86	4.86
$\mathcal{Q}_{11}$	4.7	5.0	5.0

Table 7.1: Clipping level normalized to σ_s^2.

PAPR-reduction capabilities

PAPR reduction is evaluated in terms of its complementary cumulative density function, that is the probability that PAPR exceeds a given threshold. Some PAPR-reducing techniques, such as tone reservation, increase the transmitted signal power.

Therefore, in order to just consider the peak power reduction capabilities, in such techniques it is common to define PAPR as

$$\mathrm{PAPR}(\bar{\mathbf{s}}) = \frac{||\bar{\mathbf{s}}||_{\infty}^{2}}{E[||\mathbf{s}||^{2}]/LN} \tag{7.14}$$

where the expectation is taken over all OFDM symbols. Notice that the energy of the peak-reducing signal is not taken into account in the denominator of (7.14). This avoids misleading PAPR-reductions due to potential increases in the average power of the PAPR-reduced signal and therefore all the PAPR-reduction comes from the peak power reduction [94] of the original signal.

The purpose of PAPR reduction is to decrease the distortion introduced by a nonlinear amplifier, thus it is important to reduce PAPR at the input of the amplifier. Since the amplifier belongs to the analog portion of the transmitter, this PAPR is referred to as the analog PAPR. The analog PAPR can be obtained by oversampling the transmitted signal. An oversampling factor $L = 8$ is shown to give a good approximation of the analog PAPR [69].

Figure 7.3 shows the CCDF of the analog PAPR of the previously described setups (i.e. $\mathcal{Q}_{11}/\mathcal{Q}_{21}$ with QPSK/16-QAM/64-QAM) using both conventional OFDM and the proposed TR-based method. PAPR results for the conventional case were obtained by using the different setups and by forcing the peak-reducing tones to zero. When no peak-reducing is applied, all setups have the same PAPR behavior. This suggests that the peak power reduction obtained with the proposed method using different setups can be compared without error. Oversampling to $L = 4$ was done before applying the proposed method and, subsequently, oversampling to $L = 8$ was done to compute PAPR. The analog PAPR results at the 5-th iteration of the TR-based method proposed in [69] and the analog PAPR results at the 20-th iteration of the method proposed in [44] are also shown. 256-OFDM with QPSK and the subcarrier distribution defined by $\mathcal{Q}_{11}$ is used in these two methods. As it can be observed the PAPR reduction achieved with the method proposed in this thesis is higher than the one achieved by [69] and [44]. For a symbol clip probability of 10^{-4} an analog PAPR reduction of 2.75dB can be achieved, regardless of the mapping, by using 11 out of 256 subcarriers (i.e. 4.49% bandwidth increase).

Performance improvement capabilities

In this section we compute the performance improvement capabilities of the presented PAPR-reducing method when a nonlinearity is present by comparing the power spectral density and the bit-error rate of a conventional OFDM system with those of the PAPR-reduced OFDM system.

In this section, a soft limiter type of nonlinearity is considered, since it models a situation where digital predistortion is used to linearize the HPA [59]. Figure 7.4 shows

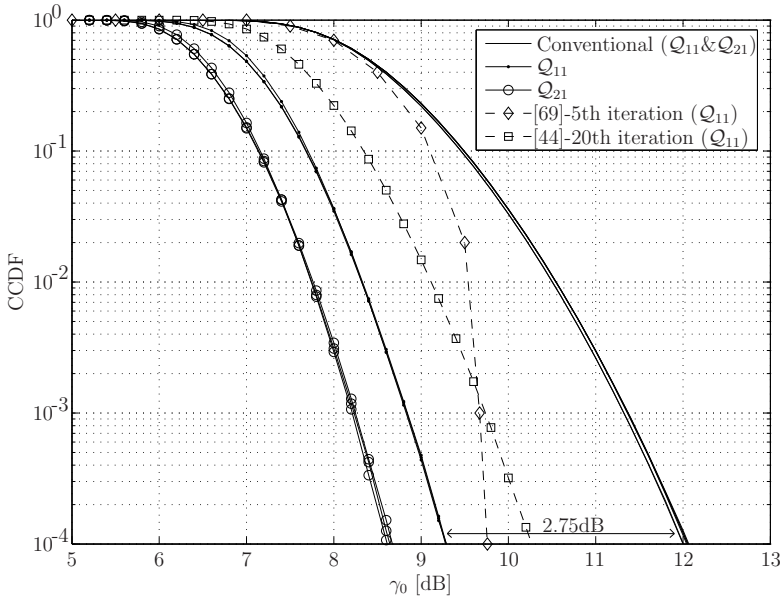

Figure 7.3: Analog PAPR for both conventional OFDM and the proposed method.

the PSD of the conventional and the PAPR-reduced OFDM system obtained when a soft limiter is present. 21 peak-reducing tones have been used with the subcarrier distribution determined by $\mathcal{Q}_{21}$. The PAPR-reduction capability of TR is independent of the mapping, therefore, the same PSD is obtained for all mapping schemes. The interference at the center of the adjacent channel is reduced by 2.9dB and 7.2dB when the nonlinearity is operating at IBO = 4dB and 5dB respectively.

The PSD was computed by means of periodogram, as the average of the PSD, computed by FFT, of the $L = 8$ oversampled signal in each OFDM symbol interval. This assures that the out-of-band radiation is computed only from the distortion introduced by the nonlinearity. In a practical implementation the OFDM symbols would be transmitted consecutively in time causing a spectral outgrowth not only due to the nonlinear amplification but also due to the sharp transitions between OFDM symbols.

Figures 7.5 and 7.6 show the error probabilities in AWGN channels of a conventional and a TR-based PAPR-reduced OFDM system with a soft limiter operating at IBO = 4dB and 5dB, respectively. The performance of conventional OFDM in a linear AWGN channel is also shown. Although the performance of TR is independent of the mapping, due to the higher sensitivity of 64-QAM compared to 16-QAM to the in-band distortion, a larger improvement in the BER performance is obtained with 64-QAM compared to 16-QAM. Further improvements in the BER of the system could be achieved by using more peak-reducing tones. However, one should note that increasing the number of peak-reducing tones results in reducing both the spectral and power efficiencies.

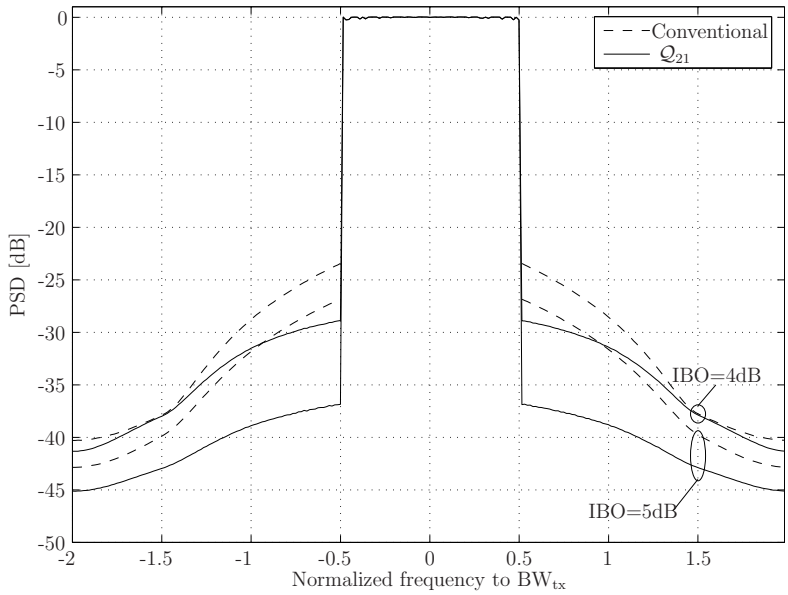

Figure 7.4: PSD of a conventional and a TR-based PAPR-reduced OFDM system obtained when a soft limiter is present.

7.2 On CM-reduction by TR

In CM-reduction, the root mean square value of each normalized cubed OFDM symbol is reduced with the aim of limiting the distortion term introduced by the nonlinear amplifier. Thus, most of the techniques that were originally designed for PAPR-reduction can easily be reformulated to CM-reduction. In particular, some techniques such as, selected mapping (SLM) [11], partial transmit sequences (PTS) [26], interleaving [56] and tone injection (TI) [94] can be directly reformulated by just changing the minimum-PAPR rule in the selection stage for minimum-CM rule. However, other techniques such as tone reservation (TR) [94] and active constellation extension (ACE) [68] do not have such a straightforward reformulation.

The main purpose of this section is to formulate the TR technique for CM-reduction. TR is a powerful technique that fits perfectly in new and emerging multicarrier systems. For instance, in IEEE 802.16 [54] the so-called radio resource units may not only be used for data transmission or signaling but also for PAPR-reduction. To reformulate TR, CM is first analyzed and simplified with the aim of defining the objective function to be used in the optimization problem. Then, the objective function is shown to be convex and, thus, the TR technique for CM-reduction is formulated as an unconstrained convex optimization problem. The solution to this problem is found by means of an iterative algorithm that approaches the optimal solution with only a few steps. Moreover, in this section, a low-complexity suboptimal algorithm capable of approaching the optimal solution with sufficient accuracy is also proposed.

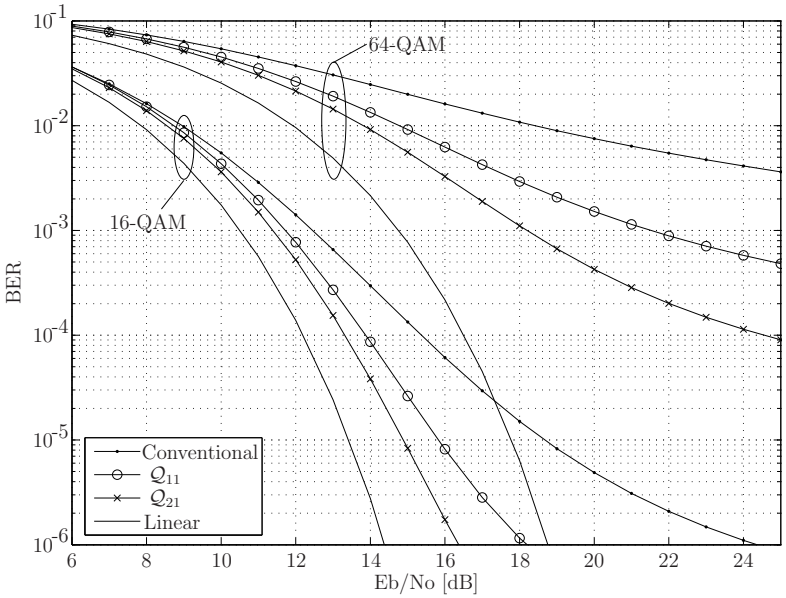

Figure 7.5: BER performance of a conventional and a TR-based PAPR-reduced OFDM system with a soft limiter operating at IBO=4dB.

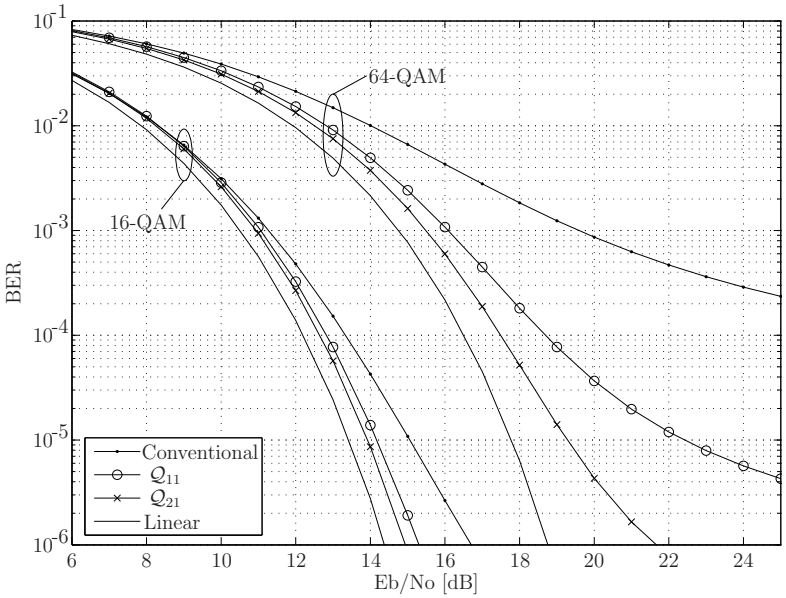

Figure 7.6: BER performance of a conventional and a TR-based PAPR-reduced OFDM system with a soft limiter operating at IBO=5dB.

7.2.1 Problem formulation

Objective cubic metric

The definition of CM provided by 3GPP can be easily simplified to obtain an equivalent definition that can be used as an objective function. The resulting metric is referred to as objective CM (OCM). To derive OCM we start from RCM since the constant terms $\mathrm{RCM}_{\mathrm{ref}}$ and K in (4.5) play no role in the optimization problem. Let $\mathbf{s}^{(m)}$ be the m-th OFDM symbol, then its RCM can be expressed as

$$\mathrm{RCM}\left[\mathbf{s}^{(m)}\right] = \sqrt{E\left[\frac{|\mathbf{s}^{(m)}|^6}{P_s^3}\right]}, \tag{7.15}$$

where P_s is the average power of the OFDM signal. OCM is obtained by removing the constant normalization P_s and squaring the metric as

$$\mathrm{OCM}\left[\mathbf{s}^{(m)}\right] = E\left[|\mathbf{s}^{(m)}|^6\right], \tag{7.16}$$

which is essentially equivalent to the definition of RCM from an optimization problem point of view.

Tone reservation technique as an optimization problem

In this section the TR technique is formulated for CM-reduction. Thus, in the remainder, the signal $c_n^{(\mathbf{s})}$ in (7.6) will be referred to as correcting or CM-reducing signal instead of peak-reducing signal. From (7.4) and (7.6) the corrected or CM-reduced signal can be easily expressed as

$$\bar{s}_n = s_n + \sum_{k=1}^{R} C_{q_k}^{(\mathbf{s})} w_{n,\,k}, \tag{7.17}$$

where $C_{q_k}^{(\mathbf{s})}$ is the complex amplitude of the k-th reserved tone and $w_{n,\,k}$ is the Fourier transform coefficient corresponding to the n-th sample and k-th reserved tone. Note that, for brevity in the mathematical expressions, the notation $C_{q_k}^{(\mathbf{s})}$ will not be used in the remainder of this chapter to stress that the complex amplitude of each correcting tone is computed according to the shape of the time domain OFDM symbol $\mathbf{s}$. Instead, C_{q_k} will be used. As in PAPR-reduction, complexity is reduced by computing each $w_{n,\,k}$ at initialization according to (7.5).

From (7.16), the amplitudes of the reserved tones that reduce CM can be obtained as

$$\arg\min_{C_{q_k}\in\mathbb{C}} \; J(\mathbf{C}), \tag{7.18}$$

where the objective function is defined as

$$J(\mathbf{C}) = \sum_{n=0}^{LN-1} \left| s_n + \sum_{k=1}^{R} C_{q_k} w_{n,\,k} \right|^6, \tag{7.19}$$

and $\mathbb{C}$ is the set of complex numbers. Let us write $\bar{s}_n$ as its real and imaginary parts, $\bar{s}_n = \bar{s}_n^{(r)} + j\bar{s}_n^{(i)}$ and define

$$\dot{\mathbf{C}} = [C_{q_1}^{(r)}, C_{q_1}^{(i)}, \ldots, C_{q_R}^{(r)}, C_{q_R}^{(i)}]^{\mathsf{T}} \tag{7.20}$$

as the real and imaginary parts of the complex amplitudes of the correcting tones. Then, the unconstrained optimization problem becomes

$$\min_{\dot{\mathbf{C}} \in \mathbb{R}^{2R}} J(\dot{\mathbf{C}}) = \min_{\dot{\mathbf{C}} \in \mathbb{R}^{2R}} \sum_{n=0}^{LN-1} \left(\left(\bar{s}_n^{(r)}\right)^2 + \left(\bar{s}_n^{(i)}\right)^2 \right)^3, \tag{7.21}$$

where

$$\bar{s}_n^{(r)} = s_n^{(r)} + \sum_{k=1}^{R} \left(C_{q_k}^{(r)} w_{n,\,k}^{(r)} - C_{q_k}^{(i)} w_{n,\,k}^{(i)} \right), \tag{7.22}$$

$$\bar{s}_n^{(i)} = s_n^{(i)} + \sum_{k=1}^{R} \left(C_{q_k}^{(i)} w_{n,\,k}^{(r)} + C_{q_k}^{(r)} w_{n,\,k}^{(i)} \right). \tag{7.23}$$

An advantage of the formulation in (7.21) is that the objective function $J : \mathbb{R}^{2R} \to \mathbb{R}$ is convex. Thus, assuming that the problem is solvable, it only has one globally optimal solution [19]. To prove the convexity of (7.21) with respect to the real and imaginary parts of the complex amplitudes of the correcting tones we start by discussing convexity with respect to $\bar{s}_n^{(r)}$ and $\bar{s}_n^{(i)}$ and then apply several operations that are known to preserve convexity [19]. Since the square function is convex, then by the property of non-negative weighted sums it follows that $(\bar{s}_n^{(r)})^2 + (\bar{s}_n^{(i)})^2$ is a convex function of $\bar{s}_n^{(r)}$ and $\bar{s}_n^{(i)}$. Moreover, since the cubic function, x^3, $\forall x \geq 0$ is convex and non-decreasing and since $(\bar{s}_n^{(r)})^2 + (\bar{s}_n^{(i)})^2$ is not only convex but also non-negative, from the rule of composition, it turns that

$$I(\bar{s}_n^{(r)}, \bar{s}_n^{(i)}) = \left(\left(\bar{s}_n^{(r)}\right)^2 + \left(\bar{s}_n^{(i)}\right)^2 \right)^3 \tag{7.24}$$

is convex. Notice that, according to equations (7.22) and (7.23), $\bar{s}_n^{(r)}$ and $\bar{s}_n^{(i)}$ can be expressed as

$$\bar{s}_n^{(r)} = \mathbf{A}^{(r)}\dot{\mathbf{C}} + s_n^{(r)}, \tag{7.25}$$

$$\bar{s}_n^{(i)} = \mathbf{A}^{(i)}\dot{\mathbf{C}} + s_n^{(i)}, \tag{7.26}$$

which is an affine transformation of $\dot{\mathbf{C}}$ with $\mathbf{A}^{(r)} = [w_{n,\,1}^{(r)} \;\; -w_{n,\,1}^{(i)} \;\; \cdots \;\; -w_{n,\,R}^{(i)}]$ and $\mathbf{A}^{(i)} = [w_{n,\,1}^{(i)} \;\; w_{n,\,1}^{(r)} \;\; \cdots \;\; w_{n,\,R}^{(r)}]$. Hence, according to the property of composition with an affine mapping, since $I(\bar{s}_n^{(r)}, \bar{s}_n^{(i)})$ is a convex function of $\bar{s}_n^{(r)}$ and $\bar{s}_n^{(i)}$, then

$$I(\dot{\mathbf{C}}) = \left(\left(\mathbf{A}^{(r)}\dot{\mathbf{C}} + s_n^{(r)}\right)^2 + \left(\mathbf{A}^{(i)}\dot{\mathbf{C}} + s_n^{(i)}\right)^2 \right)^3 \tag{7.27}$$

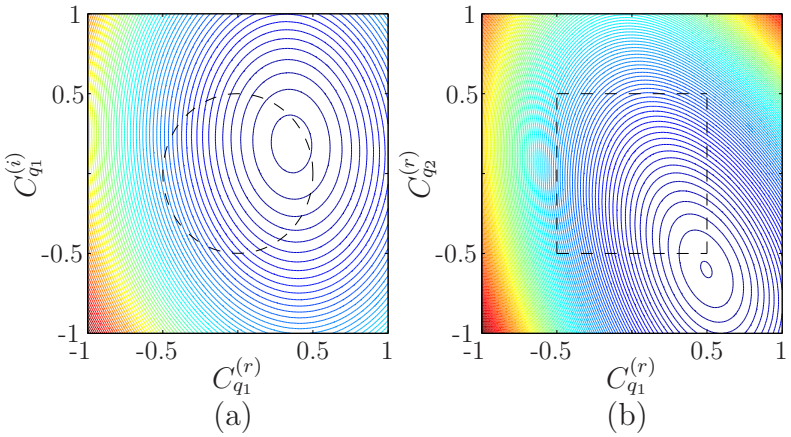

Figure 7.7: Contour plot (colored) of OCM for an OFDM system with 8 subcarriers as a function of (a) real and imaginary parts of the single complex-valued correcting tone and (b) real parts of the two real-valued correcting tones. The black dashed lines denote the sets satisfying correcting tones with magnitudes ≤ 0.5.

is a convex function of $\dot{\mathbf{C}}$. Finally, by using the property of non-negative weighted sums one can see that (7.21) is a convex function of $\dot{\mathbf{C}}$.

As an example, let us consider two OFDM systems with 8 subcarriers. In the first system all subcarriers are complex-valued and 7 of them are used for data transmission while the other is used as a correcting tone. In the second system all subcarriers are real-valued and 6 of them are used for data transmission while the other two are used as correcting tones. The contour plots of the objective function in (7.21) for two random OFDM symbols corresponding to the two described systems are shown in Figure 7.7.a and Figure 7.7.b, respectively. As it can be observed, the objective function is convex in both cases.

Solution to the optimization problem

Since the objective function $J : \mathbb{R}^{2R} \rightarrow \mathbb{R}$ in (7.21) is differentiable and convex, assuming that the problem is solvable, a necessary and sufficient condition for a point $\dot{\mathbf{C}}^*$ to be optimal is,

$$\nabla J(\dot{\mathbf{C}}^*) = \mathbf{0}, \tag{7.28}$$

where ∇ is the gradient operator as defined in Appendix D. According to [19] solving the unconstrained minimization problem in (7.21) is the same as finding the solution to (7.28), which is a set of $2R$ equations with $2R$ unknown variables. Thus, in principle, the solution to (7.21) could be found by analytically solving the optimality equation (7.28). In this particular case, the system of equations can not be solved analytically and, thus, it has to be solved numerically. This is done by means of an iterative algorithm that computes a sequence of points $\dot{\mathbf{C}}^{(0)}$, $\dot{\mathbf{C}}^{(1)}$, $\ldots$, $\dot{\mathbf{C}}^{(m)}$, $\ldots \in \mathbf{dom}\ J$,

which converge to the minimal value as $m \to \infty$. The iterative algorithm starts from a suitable point $\dot{\mathbf{C}}^{(0)}$ and compute the next point as

$$\dot{\mathbf{C}}^{(m+1)} = \dot{\mathbf{C}}^{(m)} + \Delta\dot{\mathbf{C}}^{(m)}, \tag{7.29}$$

where m is the index of the iteration. The descent direction, $\Delta\dot{\mathbf{C}}$, is found by using the Newton's method for unconstrained convex problems, which requires solving the following matrix equation [19]

$$\nabla^2 J(\dot{\mathbf{C}})\ \Delta\dot{\mathbf{C}} = -\nabla J(\dot{\mathbf{C}}). \tag{7.30}$$

In (7.30), $\nabla J(\dot{\mathbf{C}}) \in \mathbb{R}^{2R}$ and $\nabla^2 J(\dot{\mathbf{C}}) \in \mathbb{R}^{2R\times 2R}$ are the gradient and Hessian of the objective function as defined in Appendix D. According to [19] the initial point will be suitable if it lies in **dom** J and the sublevel set

$$\{\dot{\mathbf{C}} \in \mathbf{dom}\ J \mid J(\dot{\mathbf{C}}) \leq J(\dot{\mathbf{C}}^{(0)})\} \tag{7.31}$$

is closed. The objective function in this problem is continuous and with domain **dom** $J = \mathbb{R}^{2R}$. Thus, the objective function is closed (which means that all sublevel sets are closed) and, as a result, the initial sublevel set condition is satisfied by any $\dot{\mathbf{C}}^{(0)}$. A practical starting point is to assume that the correcting signal is all zero, i.e. $C_{q_k}^{(0)} = 0,\ k = 1, \ldots, R$.

Practical considerations

Two important criteria should be considered for a real implementation of the proposed method: the transmitted power and the computational complexity.

Transmitted power. Since no power control is performed, the optimal solution to the formulated problem could result in correcting tones with very large magnitudes, leading not only to a considerable increase in the transmitted power, but also to significant interference to the neighboring subcarriers if the receiver is not perfectly synchronized. To avoid this, one could reformulate (7.21) to introduce power control on the correcting tones as

$$\begin{aligned} \min_{\dot{\mathbf{C}}\in\mathbb{R}^{2R}} \quad & J(\dot{\mathbf{C}}) \\ \text{subject to} \quad & |C_{q_k}| \leq \alpha, \quad k = 1, \ldots, R. \end{aligned} \tag{7.32}$$

where α is the maximum allowed subcarrier magnitude. Conventional methods for solving convex problems with inequality constraints are usually very complex. However, in this particular case, since both the objective and constraint functions are convex, a solution that scarcely increases the complexity of the unconstrained problem can be used. Let us define χ as the set of reserved tone amplitudes that assure $J(\dot{\mathbf{C}}) < \mathrm{OCM}_0$, and ψ as the set of reserved tones with a magnitude smaller than or equal to α. Then, since both sets are convex and they overlap, the problem is to find a point in the intersection of the two sets such that OCM_0 is as low as possible. A common method to solve such problems is called projection onto convex sets (POCS) [27]. The POCS algorithm for the proposed problem is as follows:

1. Set $m = 0$ and define $C_{q_k}^{(m)} = 0,\ k = 1, \ldots, R$.
2. Compute $C_{q_k}^{(m+1)}\ k = 1, \ldots, R$ according to (7.29) and (7.30) so that $J(\dot{\mathbf{C}}^{(m+1)}) < J(\dot{\mathbf{C}}^{(m)})$.
3. Project $C_{q_k}^{(m+1)}\ k = 1, \ldots, R$ onto ψ to force the power-constraint as

$$C_{q_k}^{(m+1)} := \begin{cases} C_{q_k}^{(m+1)} & \text{if } |C_{q_k}^{(m+1)}| \leq \alpha \\ \alpha \frac{C_{q_k}^{(m+1)}}{|C_{q_k}^{(m+1)}|} & \text{otherwise.} \end{cases} \tag{7.33}$$

4. Increase m and go to step 2 unless the stopping criterion is fulfilled.

To see that both χ and ψ are convex and they overlap one can focus, as an example, on Figure 7.7. The set χ is determined by the contour lines, each one representing a different OCM_0. The set ψ is denoted by the black dashed lines, here, an amplitude constraint of $\alpha = 0.5$ is used.

Figure 7.8 shows the PSD of an original and a CM-reduced OFDM signal. $N = 256$ subcarriers with $R = 16$ reserved tones at positions

$$\mathcal{Q}_{16} = \{5, 16, 25, 40, 65, 84, 102, 108, 131, 140, 160, 183, 200, 209, 230, 247\}$$

are used. The PSD is computed by means of periodogram, as the average PSD of the $L = 4$ oversampled signal in an interval of 50 OFDM symbols, i.e. symbol shaping with rectangular windowing is assumed. As it can be observed, after applying CM-reduction the reserved tones still have an average power lower than that of the data bearing tones. One should note that in the problem of minimizing OCM (7.21) power control is inherently considered since large magnitudes in the correcting tones are, in general, avoided. Otherwise, the power of the transmitted signal and, thus, OCM would increase. However, even though large magnitudes in the correcting tones scarcely occurs, the magnitudes of some of the correcting tones in a particular OFDM symbol might be higher than the data bearing tones. To avoid this, the previously described power control algorithm based on POCS can be used. Let us evaluate the effect of the power control on the CM-reduction capabilities of the proposed method. Similar to PAPR, CM-reduction can be evaluated in terms of the complementary cumulative density function (CCDF), that is, the probability that CM of an OFDM symbol exceeds a given threshold. Figure 7.9 shows the CCDF of RCM of an OFDM signal with $N = 256$ subcarriers, and $R = 16$ and $R = 32$ reserved tones at the positions defined by $\mathcal{Q}_{16}$ and

$$\begin{aligned} \mathcal{Q}_{32} = \{&5, 11, 16, 23, 25, 33, 40, 54, 65, 71, 84, 90, 102, 105, 108, 125, 131, \\ &138, 140, 147, 160, 172, 183, 192, 200, 204, 209, 218, 230, 239, 247, 253\}, \end{aligned}$$

respectively.

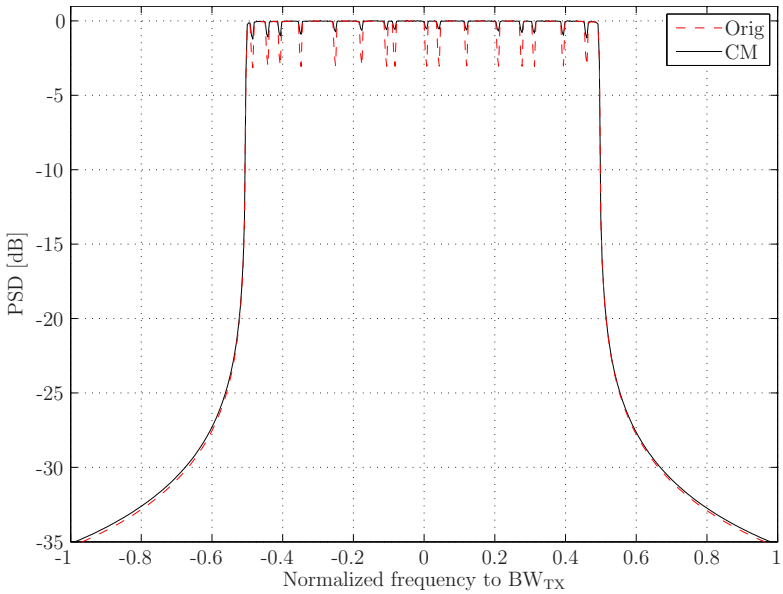

Figure 7.8: PSD of original and CM-reduced 256-OFDM systems with rectangular windowing and reserved tones at positions defined by $\mathcal{Q}_{16}$.

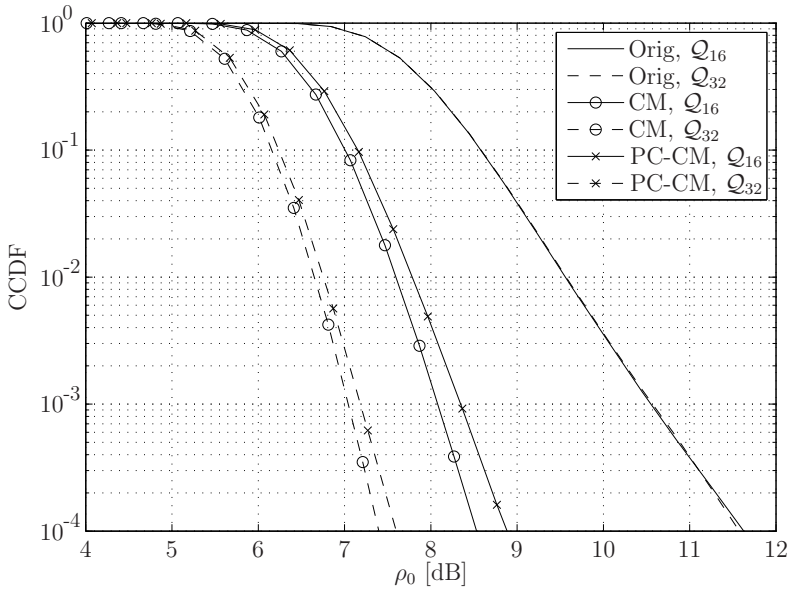

Figure 7.9: CCDF of RCM of 256-OFDM signals with reserved tones at positions defined by $\mathcal{Q}_{16}$ and $\mathcal{Q}_{32}$. Results for original (Orig), unconstrained (CM) and power-constrained (PC-CM) CM-reduced signals are shown.

A CM-reduced OFDM signal and a power-constrained CM-reduced OFDM signal where the amplitude of the correcting tones is forced to have a maximum power equal to the average power of the data bearing tones, i.e. $\alpha = 1$, are used. As it can be observed, when power-constraint is used, the CM-reduction capabilities are slightly degraded in both configurations. However, a larger degradation is experienced for lower number of reserved tones since more power per correcting tone is required to reduce CM.

Computational complexity. The optimal solution to TR for CM-reduction is found by first computing the gradient and Hessian of the objective function and then solving the matrix equation in (7.30). The complexity of computing $\nabla J(\dot{\mathbf{C}})$ is of order $\mathcal{O}(RN)$ multiplications and accumulations (MAC) and the complexity of computing $\nabla^2 J(\dot{\mathbf{C}})$ is of order $\mathcal{O}(R^2N)$ MAC. To solve the so-called Newton system in (7.30) one should take advantage of the symmetry and positive definiteness of $\nabla^2 J(\dot{\mathbf{C}})$ in order to minimize the number of computations. The most common approach is to, first, form the Cholesky factorization of $\nabla^2 J(\dot{\mathbf{C}})$, i.e. to compute a lower triangular matrix $\mathbf{L}$ that satisfies $\mathbf{L}\mathbf{L}^{\mathsf{T}} = \nabla^2 J(\dot{\mathbf{C}})$. Second, solve $\mathbf{L}\mathbf{a} = -\nabla J(\dot{\mathbf{C}})$ by forward substitution to obtain $\mathbf{a}$ and then solve $\mathbf{L}^{\mathsf{T}}\Delta\dot{\mathbf{C}} = \mathbf{a}$ by backward substitution to compute the Newton step [19]. Such procedure has a complexity of order $\mathcal{O}(R^3)$. Thus, the complexity associated with implementing TR for CM-reduction of an OFDM signal by using the proposed method is linear with the length of the symbol vector (i.e. linear with the number of data bearing tones) and cubic with the number of reserved tones. As a result, the length of the symbol vector, or equivalently, the number of subcarriers in the OFDM system is not a constraint in terms of complexity. However, the number of reserved tones, R, should be small to avoid a large increase in the complexity requirements. Note that in TR, increasing R also results in reducing both spectral and power efficiencies. Thus, reserving as small number of tones as possible is a design key.

Another important aspect is to determine the convergence speed of the iterative process. A common way to determine when the algorithm should be stopped is by checking if the error at each iteration, $J(\dot{\mathbf{C}}^{(m)}) - p^*$ where p^* is the infimum of J, is lower than a predefined value ϵ. However, this increases the computational complexity since it requires computing the so-called Newton decrement [19] at each iteration. Moreover, the Newton decrement is not valid as stopping criterion for a power-constrained optimization problem. The reason is that the error of the approximation is computed with respect to the optimal point of J which may not be a feasible solution to the constrained problem. Thus, the maximum error criterion might never be fulfilled. Instead, the convergence speed is evaluated by computing the statistical CM reduction at each iteration. Figure 7.10 shows the CM-reduction capabilities of the proposed method at different iterations for a 256-OFDM system with reserved tones at positions $\mathcal{Q}_{16}$. As it can be observed, for both unconstrained and power-constrained CM-reduction, the maximum performance is achieved with only two iterations. Moreover, a solution sufficiently close to the optimum can be obtained by just one iteration.

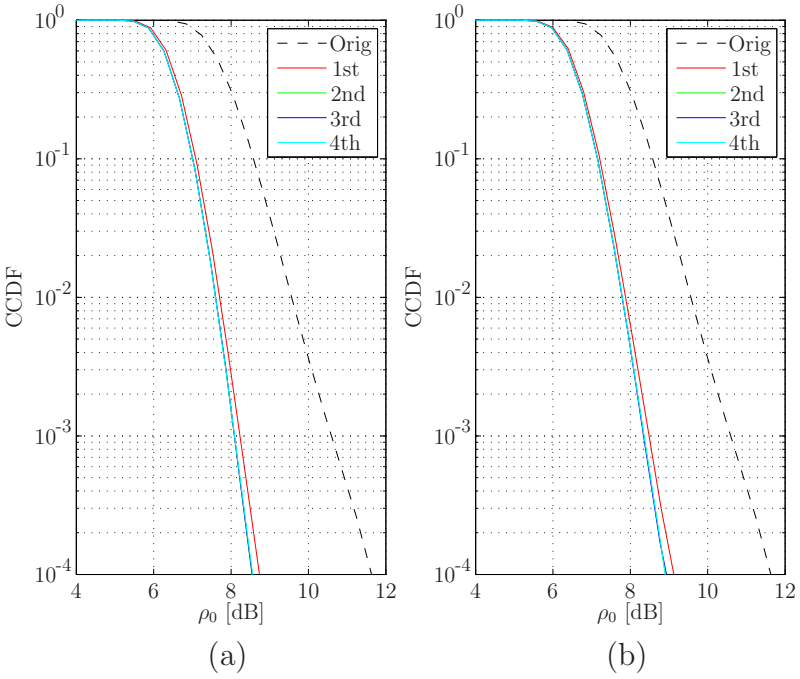

Figure 7.10: CCDF of RCM at each iteration when (a) unconstrained and (b) power-constrained CM-reduction are done. An OFDM system with $N = 256$ subcarriers and correcting tones at positions defined by $\mathcal{Q}_{16}$ is considered.

7.2.2 Suboptimum solution

In Section 7.2.1 it was shown that the complexity of the optimal solution is cubic with the number of correcting tones and, thus, small values of R are desired. Although using few correcting tones is also desired from efficiency point of view, in case that a moderate or large number was used the complexity required to find the optimal solution could be too high for a practical implementation. In this section, a suboptimal method that finds a sufficiently accurate solution with much lower complexity is formulated. The proposed method is based on that presented in Section 7.1 but reformulated for CM-reduction. It consists in (*i*) compute a correcting signal from a clipped version of the original OFDM symbol, (*ii*) filter the correcting signal in order to fulfill the constraints of TR and (*iii*) rescale the resulting signal to reduce CM.

Note that in order to reduce OCM of a signal, large magnitudes in the time domain samples must be avoided. This could be achieved by using a clipping device with a sufficiently low clipping threshold such that a significant number of time domain samples are clipped. However, as discussed in Section 7.1 this would result in a clipping noise that would increase both the out-of-band radiation and modify the data bearing tones, thus increasing BER. To avoid this, frequency domain filtering must be done so that the energy of the correcting signal lies only on the reserved tones. A detailed

description of the proposed method is as follows:

1. Clip the OFDM data symbol s_n to obtain $\tilde{s}_n$:

$$\tilde{s}_n = \begin{cases} s_n & \text{if } |s_n| \leq A \\ A\frac{s_n}{|s_n|} & \text{otherwise,} \end{cases} \tag{7.34}$$

   where A is the clipping threshold.

2. Compute the unconstrained correcting signal as $\tilde{c}_n = \tilde{s}_n - s_n$.

3. Compute the complex amplitudes of the correcting tones by projecting $\tilde{c}_n$ onto the time domain representation of each reserved tone:

$$\bar{C}_{q_k} = \sum_{n=0}^{LN-1} \tilde{c}_n w^*_{n,\,k} \qquad k = 1, \ldots, R. \tag{7.35}$$

   where $w_{n,\,k}$, is computed at initialization according to (7.5) and the asterisk denotes complex conjugate.

4. Compute the TR-constrained correcting signal as

$$\bar{c}_n = \sum_{k=1}^{R} \bar{C}_{q_k} w_{n,\,k}. \tag{7.36}$$

5. Rescale $\bar{c}_n$ to reduce CM of the corrected signal and then compute the CM-reduced signal as $\bar{s}_n = s_n + \mu\bar{c}_n$. Where μ is the scaling factor that is found by solving the following unconstrained convex optimization problem

$$\arg\min_{\mu\in\mathbb{C}} \; J(\mu), \tag{7.37}$$

   with

$$J(\mu) = \sum_{n=0}^{LN-1} \left(\left(\bar{s}_n^{(r)}\right)^2 + \left(\bar{s}_n^{(i)}\right)^2 \right)^3 \tag{7.38}$$

$$\bar{s}_n^{(r)} = s_n^{(r)} + \mu^{(r)}\bar{c}_n^{(r)} - \mu^{(i)}\bar{c}_n^{(i)}, \tag{7.39}$$

$$\bar{s}_n^{(i)} = s_n^{(i)} + \mu^{(r)}\bar{c}_n^{(i)} + \mu^{(i)}\bar{c}_n^{(r)}. \tag{7.40}$$

The reader should note that the above described procedure is similar to that proposed for PAPR-reduction in Section 7.1. In fact they only differ in the clipping threshold that is used and the way the scaling factor μ is computed. Therefore, as in PAPR-reduction, the above method can be applied iteratively to achieve larger CM-reductions. The block diagram of the iterative implementation of this method is, in fact, the same as that depicted in Figure 7.2.

Following the discussions in Section 7.2.1, the scaling factor μ can be found by means of the iterative Newton's method. As in the optimal method, simulation results suggest that very few steps are required to approach the infimum of J. However, here the complexity of each iteration is reduced to order $\mathcal{O}(N)$ and, thus, it is similar to that of low-complexity PAPR-reducing methods [34]. The reader is referred to Appendix D for further information.

Figures 7.11 and 7.12 show the PSD and the CCDF of RCM of a 256-OFDM system with optimal and suboptimal CM-reduction. In the optimal approach two iterations are done to compute the complex amplitude of the correcting tones by means of Newton's method. In the suboptimum, three iterations of the above described procedure are done. At each iteration the scaling factor is computed by using two iterations of the Newton's method. The PSD is computed assuming rectangular windowing as in Figure 7.8. It can be observed that the CM-reduction capabilities of the suboptimal approach are very close to those of the optimal method and that, this is achieved by using a similar power in the correcting tones. Moreover, simulation results suggest that for large number of correcting tones, where the complexity of the optimal approach might be too large for a practical implementation, both approaches have the same CM-reduction capabilities.

7.2.3 Performance evaluation

In this section the performance of the proposed CM-reducing methods when a nonlinearity is present, is evaluated by comparing the PSD and BER of conventional OFDM systems with those of CM-reduced OFDM systems. Moreover, comparisons with equivalent PAPR-reduced signals are done.

In the simulations we setup an OFDM system with $N = 256$ subcarriers and 16-QAM and 64-QAM baseband modulations. $R = 16$ and $R = 32$ reserved tones according to the previously described distributions, $\mathcal{Q}_{16}$ and $\mathcal{Q}_{32}$, are used. A soft limiter is considered, since it models a situation where digital predistortion is used to linearize the HPA [59]. Figure 7.13 shows the PSD of original and CM-reduced OFDM signals when a soft limiter operating at IBOs of 3dB or 5dB is present at the output of the transmitter. In order to assure that the out-of-band radiation is computed by only considering the distortion introduced by the nonlinearity, the PSD is computed by means of periodogram as the average of the PSD, computed by FFT, of the $L = 4$ oversampled signal in each OFDM symbol interval. TR is independent of the mapping. Thus, assuming that the same average power is transmitted, the same PSD will be obtained regardless of the mapping. As it can be observed in Figure 7.13, when CM-reduction is used, the distortion term is significantly reduced. For the simulated setup, the in-band distortion is approximately reduced by 4.25dB and 10.7dB for IBOs of 3dB and 5dB, respectively. The interference at the center of the adjacent channel is reduced by 2.1dB and 8.1dB for the same operating points.

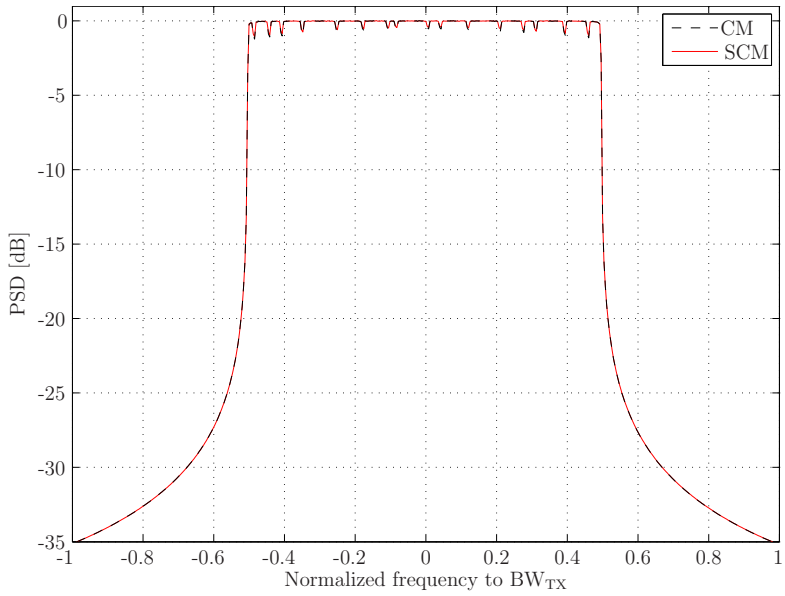

Figure 7.11: PSD of optimally (CM) and suboptimally (SCM) CM-reduced 256-OFDM signals with rectangular windowing and reserved tones at positions defined by $\mathcal{Q}_{16}$.

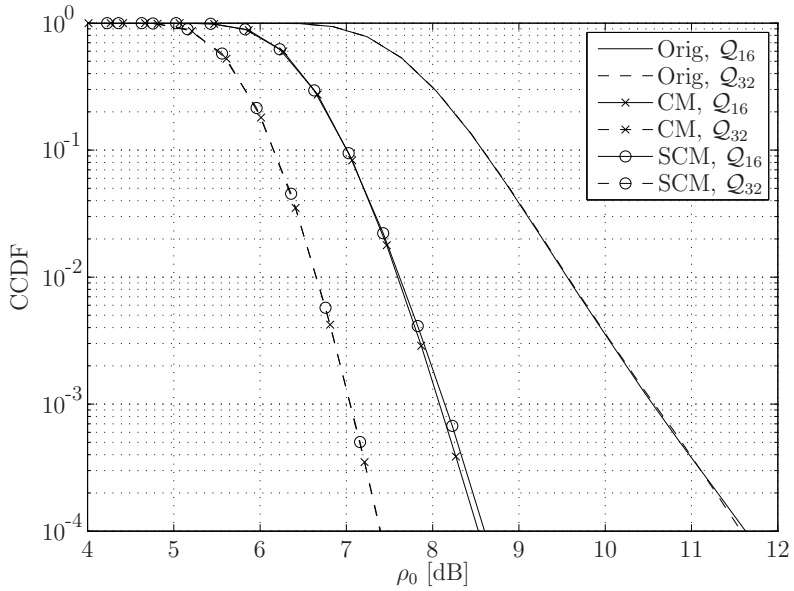

Figure 7.12: CCDF of RCM of CM-reduced 256-OFDM signals with reserved tones at positions $\mathcal{Q}_{16}$ and $\mathcal{Q}_{32}$. Results for original (Orig), optimally (CM) and suboptimally (SCM) CM-reduced signals are shown.

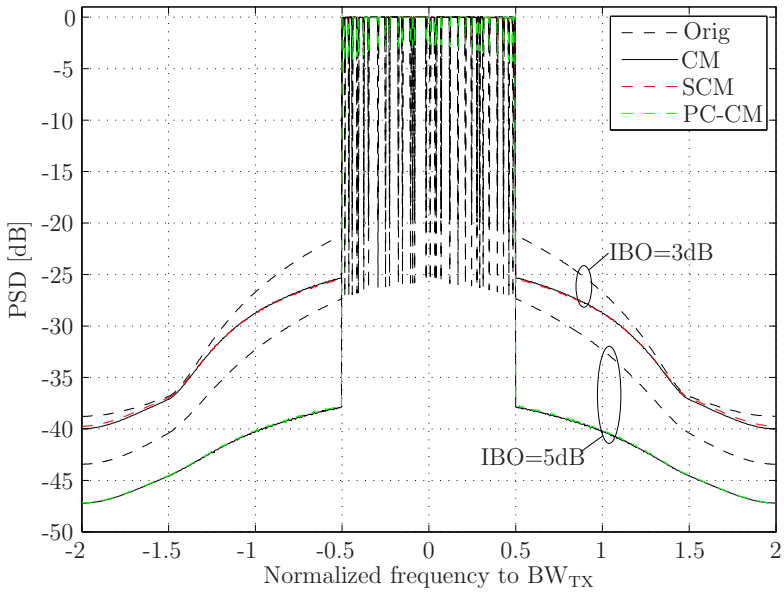

Figure 7.13: PSD of several 256-OFDM signals with reserved tones at positions defined by $\mathcal{Q}_{32}$ when a soft limiter is present. Original (Orig), optimally (CM), suboptimally (SCM) and power-constrained (PC-CM) CM-reduced OFDM signals are considered.

In Section 7.2.1, it was observed that when a power-constraint in the correcting tones was considered, the CM-reduction capabilities were slightly reduced. There, the maximum power of the correcting tones was limited to the average power of the data bearing tones. However, since the average power of the correcting tones is significantly lower than the data bearing tones, a more realistic restriction is to limit the maximum power of the correcting tones to that of the data bearing tones, i.e. use $\alpha = 1.34$ and $\alpha = 1.52$ for 16-QAM and 64-QAM, respectively. The PSD for the power-constrained CM-reduced OFDM signal in Figure 7.13 is computed by using an IBO of 5dB in the soft limiter and $\alpha = 1.34$, i.e. 16-QAM mapping is assumed. As it can be observed, the same reduction of the distortion term as for unconstrained CM-reduction is achieved. Another important aspect to emphasize in Figure 7.13 is that the reduction of the distortion term achieved by the proposed low-complexity suboptimal solution is the same as that of the optimal one.

Figures 7.14 and 7.15 show the error probabilities in AWGN channels of original and CM-reduced OFDM signals when a soft limiter is present. In Figure 7.14 the soft limiter is set to operate at IBOs of 3dB and 4dB for 16-QAM and 64-QAM mapping, respectively. In Figure 7.15 the soft limiter is set to operate at IBOs of 4dB and 5dB. As it can be noticed a large performance improvement is obtained when applying CM-reduction. However, this improvement depends on the number of reserved tones and the mapping. On one hand, it was previously observed that the more correcting tones were used the larger the CM-reduction capabilities would be. Thus, as expected, a larger BER performance improvement is achieved with $\mathcal{Q}_{32}$. On the other hand,

in Figure 7.13 one could observe that if the same CM-reduction method was used, an equal reduction of the distortion term was obtained independent of the mapping. However, since 64-QAM is more sensitive to the in-band distortion compared to 16-QAM, a larger improvement in the BER performance is obtained with 64-QAM when the distortion term is reduced by the same factor.

Figure 7.14 also shows the BER performance improvement achieved by the suboptimal method. The performance in this case is very close to that of the optimal solution. In Figure 7.15, power-constrained CM-reduction is also evaluated where the maximum magnitude of the correcting tones is forced not to exceed that of the data bearing tones. As it can be observed, both unconstrained and power-constrained results are very close.

Finally, Figures 7.16 and 7.17 compare the performance of CM-reduced OFDM systems with PAPR-reduced OFDM systems. Since the aim is to compare practical implementations of the OFDM systems, in both cases the low-complexity suboptimal methods with no power control are considered. For CM-reduction the suboptimal method presented in this section is used, while PAPR-reduction uses the method presented in Section 7.1. It is important to remark that both methods are indeed very similar and that they both have complexity requirements of order $\mathcal{O}(N)$. In fact, they all follow the structure shown in Figure 7.2 and only differ in the clipping threshold that is used and the way the scaling factor μ is computed. The scaling factor for CM-reduction is computed according to Section 7.2.2 so that OCM of each OFDM symbol is minimized. For PAPR-reduction the SGP algorithm proposed in [68] is used, which aims to reduce the peak factor of each OFDM symbol, is used.

It can be observed in Figure 7.16 that by using CM-reduction not only a larger reduction of the out-of-band radiation is achieved (approximately 1dB at the center of the adjacent channel) but also the magnitude of the reserved tones is much lower than the required for PAPR-reduction. For CM-reduction the maximum average-power in the correcting tones is 0.29dB lower than the average power of the data-bearing tones while for PAPR-reduction it is 0.75dB higher. On the other hand it can be noticed in Figure 7.17 that the BER performance improvement of CM-reduction is larger than that of PAPR-reduction.

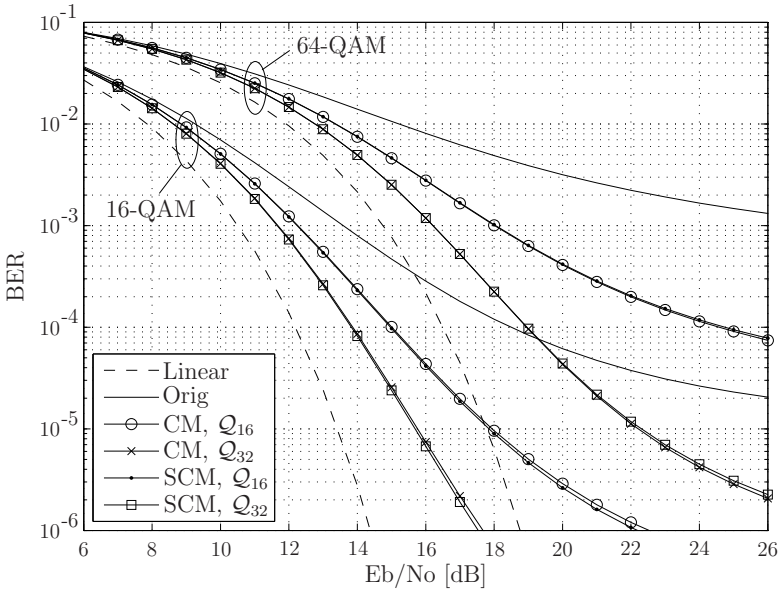

Figure 7.14: BER performance of original (Orig), optimally (CM) and suboptimally (SCM) CM-reduced 256-OFDM signals with reserved tones at positions $\mathcal{Q}_{16}$ and $\mathcal{Q}_{32}$ when a SL is present. The SL is set to operate at IBOs of 3dB and 4dB for 16-QAM and 64-QAM, respectively

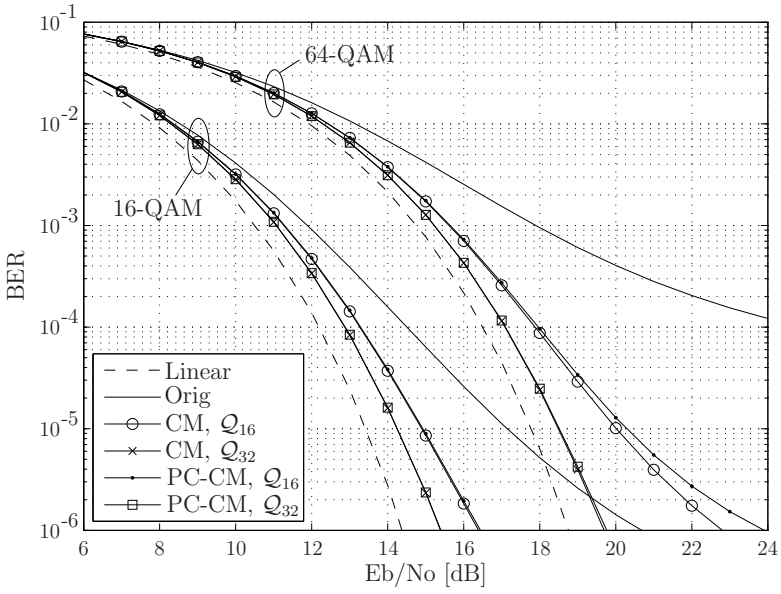

Figure 7.15: BER performance of original (Orig), unconstrained (CM) and power-constrained (PC-CM) CM-reduced 256-OFDM signals with reserved tones at positions $\mathcal{Q}_{16}$ and $\mathcal{Q}_{32}$ when a SL is present. The SL is set to operate at IBOs of 4dB and 5dB for 16-QAM and 64-QAM, respectively

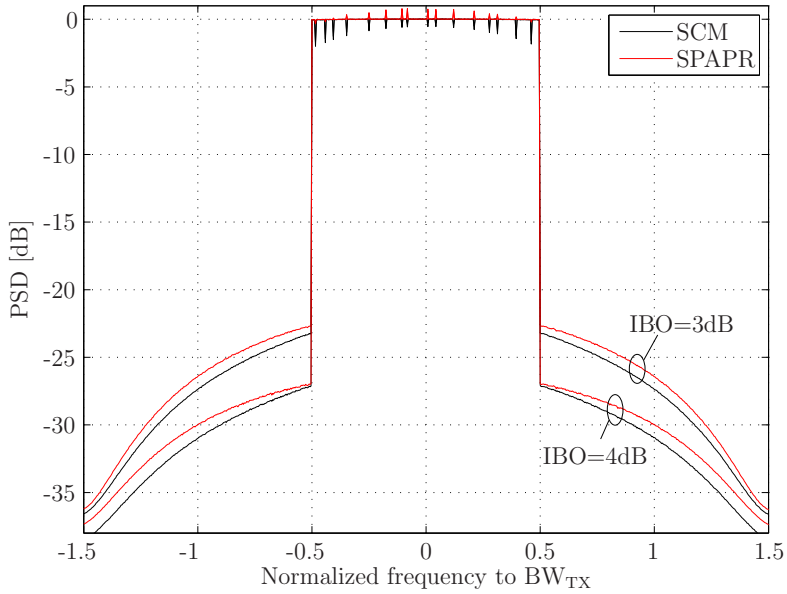

Figure 7.16: PSD of several 256-OFDM signals with reserved tones at positions defined by $\mathcal{Q}_{16}$ when a SL operating at IBOs of 3dB and 5dB is present. Equivalent suboptimally CM-reduced (SCM) and suboptimally PAPR-reduced (SPAPR) OFDM systems are considered.

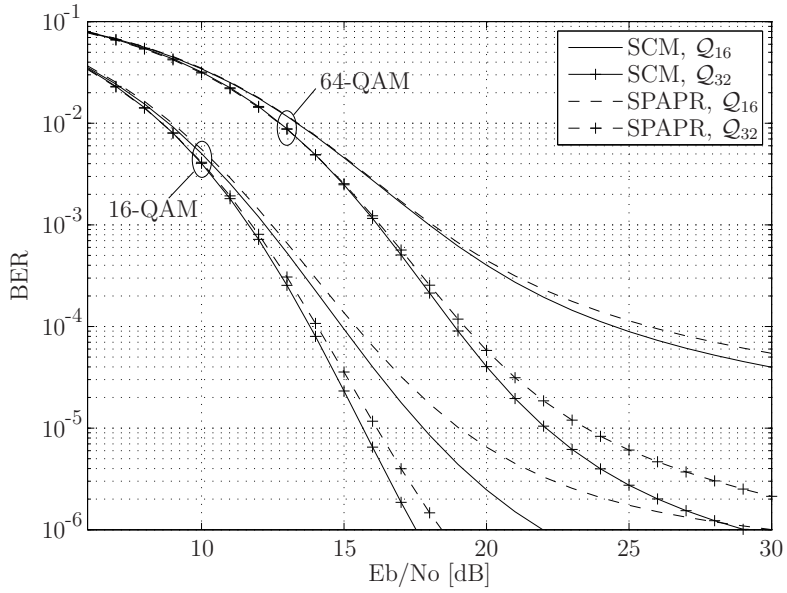

Figure 7.17: BER performance of suboptimally CM-reduced (SCM) and suboptimally PAPR-reduced (SPAPR) 256-OFDM signals with reserved tones at positions $\mathcal{Q}_{16}$ and $\mathcal{Q}_{32}$ when a SL is present at the output of the transmitter. The SL is set to operate at IBOs of 3dB and 4dB for 16-QAM and 64-QAM, respectively.

Chapter 8

Controlled spectral outgrowth technique

In Chapter 5 several techniques to reduce the envelope fluctuations of the transmitted signal were introduced. Most of the techniques have important drawbacks that must be considered, such as reducing the power and bandwidth efficiencies and requiring transmission of additional information. In this chapter a new technique to reduce the envelope fluctuations of the transmitted signal, termed as controlled spectral outgrowth (CSO), is discussed. In CSO PAPR/CM-reduction is achieved by increasing the out-of band radiation of the nearby subcarriers in a controlled way such that it is transparent to the receiver, the spectral efficiency is maintained and the power efficiency is scarcely reduced.

The key idea in CSO is to take advantage of the radio frequency (RF) specifications defined in standardization. One should take into account that, as long as the regulatory masks and the constraints on the power radiated outside the nominal channel are fulfilled, the transmitter is, in principle, allowed to radiate outside the assigned bandwidth. Although this out-of-band signal is not processed by the receiver it can be used to reduce the envelope fluctuations.

It can be observed that in CM-reduction by TR, the average power of the correcting tones is significantly lower than that of the data bearing tones, even if few subcarriers are reserved for CM-reduction (see Figure 7.8). Therefore it is reasonable to believe that if a large number of correcting tones is used the required power on each of them will be much lower than that of the data bearing tones. Moreover, such assumption might even hold for PAPR-reduction. Unlike TR, in CSO the major constraint is not the number of tones to be used for PAPR/CM-reduction, but the power allocated to each tone and the total power radiated in adjacent channels. Nevertheless, since a large number of tones is used for PAPR/CM-reduction and they are expected to have a power much lower than the data bearing tones, it seems that CSO can be a promising technique to reduce the envelope variations.

CSO is specially interesting in the Antarctic project to which this PhD thesis is related. The aim of the Antarctic project is to design a robust unidirectional system for long haul communications through the ionosphere between the Spanish Antarctic Base in Livingston Island and the Ebro Observatory in Spain. The advantages of using CSO in such communication link are two fold, the power efficiency is scarcely decreased and no spectrum emission mask must be fulfilled, which increases the PAPR/CM-reduction capabilities. In long haul communications, where the signal travels through many different countries and even different continents, it is very difficult, not to say impossible, to have reserved transmission channels. Specially if one takes into account that the frequencies for which a channel is available depends strongly on the time of the day and the season of the year. Therefore, in order not to generate significant interference, low power transmission is required. It was previously discussed that for multicarrier communication, reducing the envelope fluctuations of the transmitted signal is a design key. Nevertheless if our system is strongly power limited we can not spend too much power on that. This basically means that we have to use power-efficient PAPR/CM-reducing techniques. On the other hand, the fact that our system is not subject to any standard means that no regulatory masks or constraints on the power radiated outside the transmission channel exist. This basically means that the flexibility of CSO to allocate the out-of-band power increases and, thus, that larger PAPR/CM-reduction capabilities can be achieved.

The description of CSO provided in this chapter as well as the simulation results do not consider any regulatory restrictions and therefore no power spectrum emission masks nor constraints on the power radiated outside the nominal channel are used. The reason is that this technique was specifically designed to be used within the Antarctic project. Notwithstanding, the usage of CSO in new and emerging wireless systems such as 3GPP-LTE [3], where regulatory restrictions do exist, is considered, even though no results nor specific details of its implementation are provided in this thesis.

8.1 Description of the method

In CSO, PAPR/CM-reduction is achieved by increasing the out-of band radiation over the nearby subcarriers in a controlled way. It is interesting to notice that CSO is a special case of TR, in the sense that one has to determine the complex amplitude of each correcting tone in order to reduce the envelope fluctuations of the transmitted signal. Therefore, the implementation of CSO will be similar to the suboptimal solution described in Chapter 7 for TR, i.e. clipping and frequency-domain filtering. Nevertheless, since the number of PAPR/CM-reducing tones is large, FFT/IFFT will be used to compute the correcting signal instead of projecting the clipped signal onto the correcting tones. As it will be discussed later this assures lower complexity requirements for most practical implementations.

Let us start by defining $\mathbf{S}$ as the length-N complex baseband modulated symbol vector. The reader should note that in order to be able to define the complex amplitude of the nearby subcarriers one can not use a length-N IFFT in the OFDM modulator. Instead oversampling by means of zero padding the complex baseband modulated symbol vector must be done. In previous chapters oversampling was done by appending an all-zeros vector at the end of the complex baseband modulated symbol vector. Since in CSO one deals with the nearby subcarriers it is better to implement the zero padding by adding the zeros in the middle of the symbol vector rather than appending them at the end. Being $\mathbf{S}$ the length-N OFDM symbol vector, the L-times oversampled symbol vector $\mathbf{S}^{\text{zp}}$ is created by inserting $(L-1)N$ zeros at the $\lfloor N/2 \rfloor$-th position of $\mathbf{S}$; $\forall\ L > 1$ such that $LN \in \mathbb{N}$.

In CSO the correcting (or PAPR/CM-reducing) signal is obtained by first clipping the original OFDM symbol vector, then computing the so-called unconstrained correcting signal and, finally, by frequency domain filtering the previously computed unconstrained correcting signal. The clipped OFDM symbol in the time domain is defined as

$$\tilde{s}_n = \begin{cases} s_n & \text{if } |s_n| \leq A \\ A\frac{s_n}{|s_n|} & \text{otherwise} \end{cases} \tag{8.1}$$

where A is the clipping threshold and s_n is the n-th sample of the original OFDM symbol $\mathbf{s} = \frac{1}{\sqrt{N}}\text{IFFT}(\mathbf{S})$. Subsequently, the unconstrained correcting signal is computed by subtracting the original OFDM symbol vector from the clipped one, $\tilde{\mathbf{c}} = \tilde{\mathbf{s}} - \mathbf{s}$. Let us now define $\mathcal{S}_C$ as the set of subcarrier indexes nearby to the band edges

$$\mathcal{S}_C = \{\lfloor M/2 \rfloor, \ldots, \lfloor M/2 \rfloor + \lfloor \eta M/2 \rfloor - 1, N - \lceil M/2 \rceil - \lceil \eta M/2 \rceil, \ldots, N - \lceil M/2 \rceil - 1\}$$

where η is the *spectral spreading factor* satisfying both $\eta M \in \mathbb{N}$, so that an integer number of out-of-band subcarriers are added, and $\eta \leq \frac{N}{M} - 1$ to assure Nyquist sampling rate. The procedure to compute the correcting signal is as follows. First compute $\tilde{\mathbf{C}} = \text{FFT}(\tilde{\mathbf{c}})$, next define the peak reducing signal in the frequency domain as

$$C_k = \begin{cases} \tilde{C}_k & \forall k \in \mathcal{S}_C \\ 0 & \text{otherwise} \end{cases} \tag{8.2}$$

where C_k is the k-subcarrier of the constrained correcting signal $\mathbf{C}$ and, finally, apply an IFFT to obtain the time domain PAPR/CM-reducing signal $\mathbf{c} = \text{IFFT}(\mathbf{C})$.

8.1.1 Iterative implementation

Similar to TR, the previously described method can be applied iteratively to achieve a larger reduction of the envelope fluctuations. The iterative implementation is depicted in Figure 8.1 and can be described as follows:

1. Compute $\mathbf{S}^{\text{zp}}$ by zero padding $\mathbf{S}$ and then apply an IFFT (plus amplitude normalization) to get $\mathbf{s}$. Define $\bar{\mathbf{s}}^{(0)} = \mathbf{s}$ and set $i = 0$.

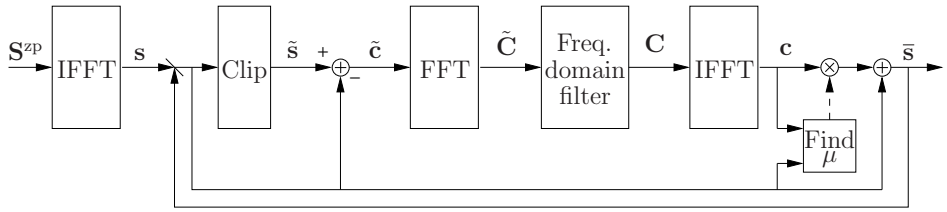

Figure 8.1: Block diagram of the iterative implementation of the proposed method.

2. Clip $\bar{\mathbf{s}}^{(i)}$ to get $\tilde{\mathbf{s}}^{(i)}$.
3. Compute $\tilde{\mathbf{c}}^{(i)} = \tilde{\mathbf{s}}^{(i)} - \bar{\mathbf{s}}^{(i)}$ and $\tilde{\mathbf{C}}^{(i)} = \mathrm{FFT}(\tilde{\mathbf{c}}^{(i)})$.
4. Obtain $\mathbf{C}^{(i)}$ as described in (8.2). If $\mathbf{C}^{(i)} = \mathbf{0}$ return $\bar{\mathbf{s}}^{(i)}$ and terminate. Otherwise, apply an IFFT to get $\mathbf{c}^{(i)}$.
5. Compute $\bar{\mathbf{s}}^{(i+1)} = \bar{\mathbf{s}}^{(i)} + \mu \mathbf{c}^{(i)}$.
6. Increment i, go to step 2 if the maximum number of iterations has not been reached and the target PAPR/CM has not been achieved. Otherwise, return $\bar{\mathbf{s}}^{(i)}$ and terminate.

The above described procedure can be used to reduce either PAPR or CM. In fact, both implementations only differ in the clipping threshold that is used and the way the scaling factor μ in step 5 is computed. For PAPR-reduction the optimal scaling factor is found by solving the following minimax optimization problem

$$\mu = \arg\min_{\mu \in \mathbb{C}} ||\bar{\mathbf{s}} + \mu \mathbf{c}||_{\infty}. \tag{8.3}$$

To reduce the computational complexity one can use the SGP approach proposed in [68]. On the other hand, CM-reduction requires solving the following unconstrained convex optimization problem

$$\mu = \arg\min_{\mu \in \mathbb{C}} \sum_{n=0}^{LN-1} \left(\left(\bar{s}_n^{(r)}\right)^2 + \left(\bar{s}_n^{(i)}\right)^2 \right)^3, \tag{8.4}$$

with

$$\bar{s}_n^{(r)} = s_n^{(r)} + \mu^{(r)} \bar{c}_n^{(r)} - \mu^{(i)} \bar{c}_n^{(i)}, \tag{8.5}$$
$$\bar{s}_n^{(i)} = s_n^{(i)} + \mu^{(r)} \bar{c}_n^{(i)} + \mu^{(i)} \bar{c}_n^{(r)}. \tag{8.6}$$

Which, as discussed in Section 7.2 and Appendix D.2 can be found by means of an unconstrained convex optimization problem. In the expressions above for CM-reduction, the superindexes (r) and (i) are used to denote real and imaginary parts, respectively. For simplicity the iteration index is omitted.

8.1.2 Computational complexity

Let us recall from Chapter 7 that the complexity of computing the scaling factor μ for both PAPR and CM reduction are of order $\mathcal{O}(N)$. Therefore, the computational complexity of the above described method is mainly due to the FFT and IFFT operations used for frequency domain filtering, which are of order $\mathcal{O}(LN \log LN)$. One should note that in TR the unconstrained correcting signal was projected onto the reserved tones, while in CSO a frequency domain filter based on FFT/IFFT is used. The reason is that since in TR a few number of correcting tones is used it is more efficient to compute the correcting signal by means of projection, hence the complexity for TR is of order $\mathcal{O}(N)$. On the other hand, in CSO a large number of correcting tones is used, therefore if one computes the correcting signal by means of projection the complexity tends to be of order $\mathcal{O}((LN)^2)$, specially for large values of η. By using a frequency domain filter based on FFT/IFFT one assures that the complexity of the system is of order $\mathcal{O}(LN \log LN)$ regardless of the desired spectral spreading factor.

It is interesting to notice that in order to compute the optimal solution for CM reduction one could use a formulation similar to the one described in Section 7.2. To fulfill the spectrum emission mask constraint one can use a similar approach to that proposed in Section 7.2 for subcarrier power control. However since in CSO a large number of subcarriers is used, the complexity of computing the optimal solution would be too high for a practical implementation.

8.1.3 Choice of the parameters

Three parameters describe the behavior of the CSO method: the clipping threshold, the number of iterations and the spectral spreading factor (η). The optimum parameters depend on the signal metric, the number of subcarriers and the mapping scheme, and must be computed numerically. In this chapter, a 256-subcarrier OFDM system employing QPSK, 16-QAM and 64-QAM with PAPR-reduction is evaluated. Maximum peak-power reduction is achieved with $\eta = 0.375$, four iterations (using SGP approach [68]) and a clipping threshold of 4.8dB, 5dB and 5.3dB for QPSK, 16-QAM and 64-QAM, respectively.

8.2 Performance evaluation

Even though it was previously discussed that CM is a more appropriate metric, in this chapter, the performance of the proposed technique is evaluated in terms of its capability to reduce the PAPR of an OFDM signal. PAPR is computed as stated in (7.14) to avoid misleading PAPR-reductions due to potential increases in the average power of the PAPR-reduced signal and therefore to assure that the PAPR-reduction just comes from the peak power reduction.

A total oversampling of $L = 8$ is used to better approximate the analog PAPR, which is of great interest since it represents the PAPR of the transmitted signal at the input of the power amplifier. In order to reduce the computational complexity an oversampling of $L = 4$ is used in CSO method and the obtained peak reduced signal is subsequently oversampled to $L = 8$. Lower oversampling factors in CSO computation lead to poorer peak power reductions.

8.2.1 Convergence speed

In this section the convergence speed of the proposed technique, with and without SGP, is evaluated. To determine the convergence speed the PAPR-reduction capabilities for different number of iterations are computed. Figure 8.2 shows the peak power reduction results at different iterations when an OFDM system with 256 subcarriers and QPSK mapping is used. As it can be observed, the peak power reduction at a symbol clip probability of 10^{-4} is 2.31dB. Maximum peak reduction is not obtained until the 9-th iteration. Figure 8.3 shows the PAPR reduction of the CSO method at different iterations when the peak reducing signal is scaled by the SGP approach of μ. There are two advantages with respect to the non-SGP implementation: larger peak reduction is achieved and only 4 iterations are needed to achieve the maximum peak reduction. Furthermore, it is interesting to notice that a 2.2dB of PAPR reduction at 10^{-4} symbol clip probability is achieved with just one iteration.

8.2.2 Spectral spreading factor

This section evaluates the effect of the spectral spreading factor in both the peak power reduction capabilities and the increase of the transmitted power. The effect of η over the PAPR is shown in Figure 8.4. As one would expect, the PAPR reduction capability improves as η increases. However, a saturation on the peak power reduction capabilities is observed around $\eta = 0.375$.

Let us now evaluate the increase in the transmitted power. The PSD of the transmitted signal is first considered. Figure 8.5 shows the power spectral density of a CSO-based peak reduced OFDM system with 256 subcarriers employing QPSK. Several results are shown for different values of η, moreover, for $\eta = 0.375$ the PSD of the described OFDM system with 16-QAM and 64-QAM mapping is also shown. Two statements shall be made: (i) the larger the spectral spreading factor is, the smaller the amplitude of the out-of-band subcarriers will be, and (ii) under the same conditions lower power increase occurs when larger constellation sizes are used. Table 8.1 shows the power increase of the transmitted signal when the peak power is reduced by CSO using several values of η and different mapping schemes. It can be observed that a lower increase of the signal power is obtained at larger values of η.

An interesting conclusion is that even though a saturation in the PAPR-reduction occurs as η increases, a lower increase in the transmitter power is required. In other

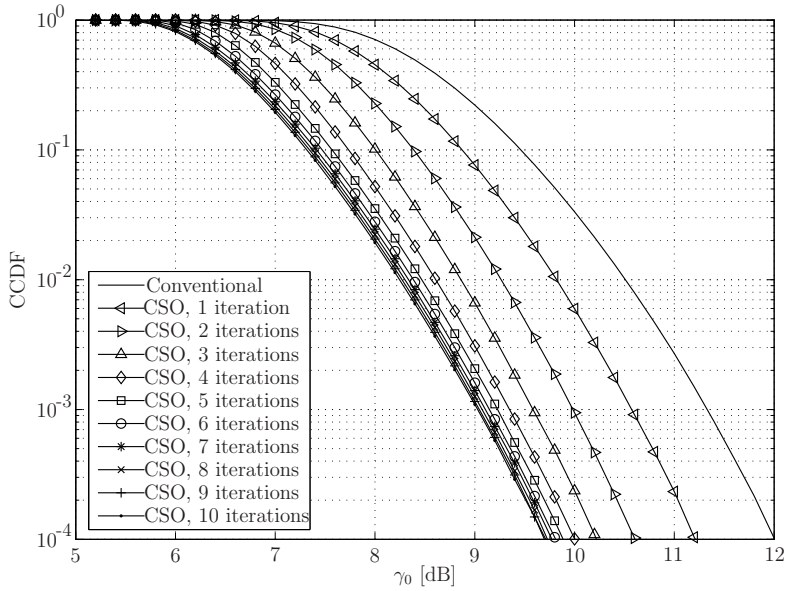

Figure 8.2: Convergence speed of the CSO method, with $\mu = 1$, applied to a QPSK-mapped 256-subcarrier OFDM system.

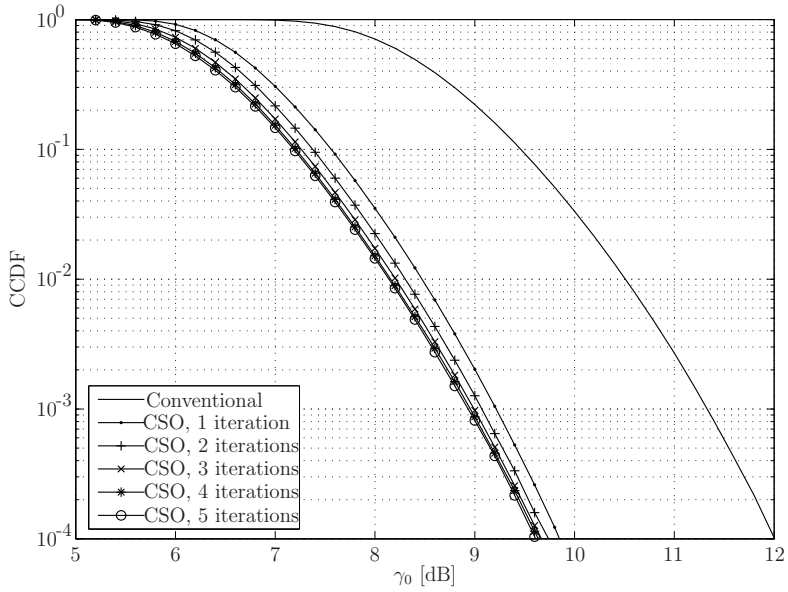

Figure 8.3: Convergence speed of the CSO-SGP method applied to a QPSK-mapped 256-subcarrier OFDM system.

Power increase [dB]	QPSK	16-QAM	64-QAM
$\eta = 0.125$	0.238	0.227	0.202
$\eta = 0.25$	0.172	0.159	0.133
$\eta = 0.375$	0.136	0.124	0.101
$\eta = 0.5$	0.111	0.101	0.080

Table 8.1: Power increase in dB due to the peak power reduction by CSO, in a 256-subcarrier OFDM system.

words, one can achieve the same peak-power reduction by using a large spectral spreading factor for a very small increase in the transmitter power. For non-regulated communication links such as the Antarctic one, this means that the envelope fluctuations of the transmitted signal can be significantly reduced by scarcely reducing the power efficiency. On the other hand, for those systems that are subjected to regulatory restrictions such as spectrum emission masks and maximum power radiated outside the nominal channel, this suggests that a very large spectral spreading factor could be used. The reason is that the power required in each correcting tone would be very small and, as a consequence the spectrum mask restriction could be easily fulfilled. Notice, that the limitation in the spectral spreading factor is in practice given by the oversampling factor used in the computation of the PAPR/CM-reducing signal.

8.2.3 Effect of the mapping scheme

Figure 8.6 shows the CCDF of PAPR of a 256-subcarrier OFDM system employing PAPR-reduction by CSO and QPSK, 16-QAM and 64-QAM mapping schemes. For comparison purposes the results of equivalent conventional and ACE-based PAPR-reduced OFDM systems [68] are also shown. In CSO, $\eta = 0.25$ and the clipping thresholds in Section 8.1.3 are used. For ACE the parameters defined in [68] are considered. As it can be observed, the peak power reduction of the CSO method is independent of the modulation scheme. ACE achieves better peak reductions if large PAPR can be accepted (over 5.8dB, 7.38dB and 8.24dB in QPSK, 16-QAM and 64-QAM, respectively) and CSO offers better results below this values. Note that the PAPR reduction capabilities of the ACE method will decrease if some of the subcarriers are used as pilots (no modification of their amplitude and phase is allowed). Furthermore, PAPR reduction by ACE depends on the modulation scheme, and the symbol power increase is greater than in CSO, which degrades the BER performance of the system. ACE power increase is 0.91dB in QPSK, 0.47dB in 16-QAM and 0.43dB in 64-QAM.

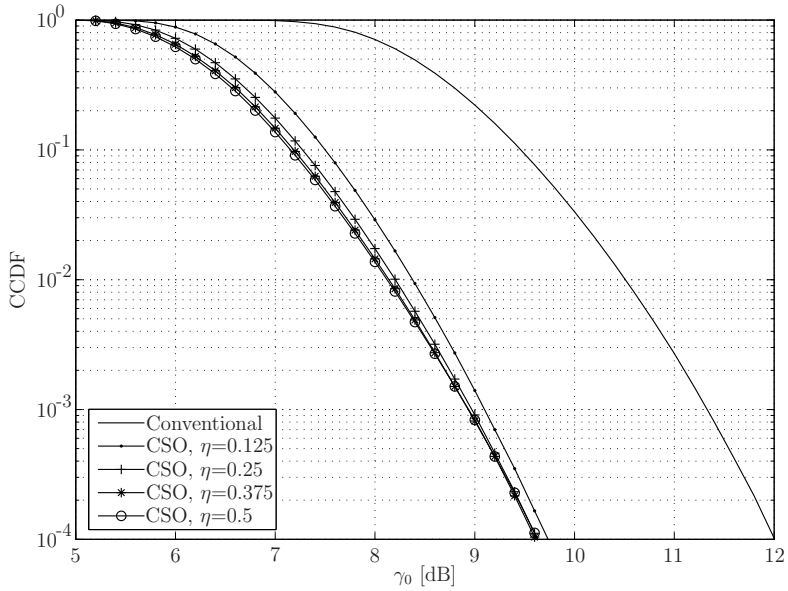

Figure 8.4: The effect of η on the PAPR results is a QPSK-mapped 256-subcarrier OFDM system.

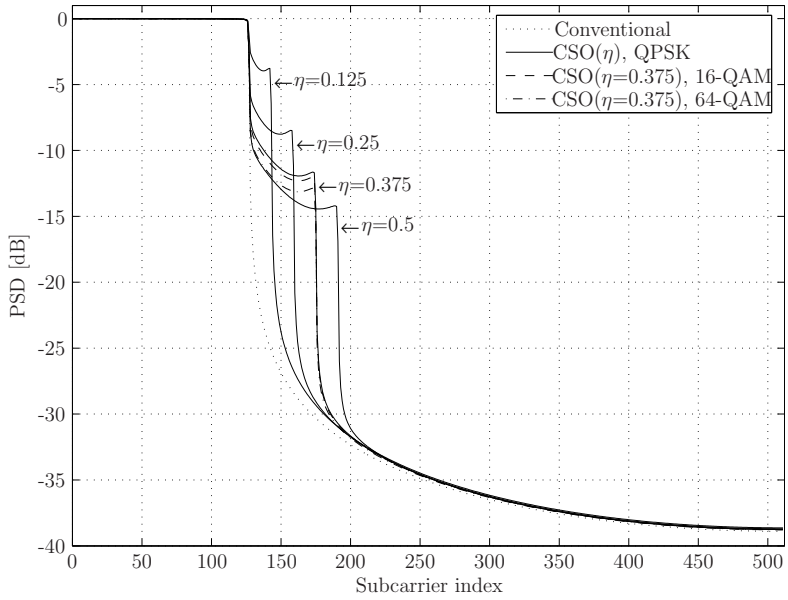

Figure 8.5: PSD results of the CSO method applied to a 256-subcarrier OFDM system.

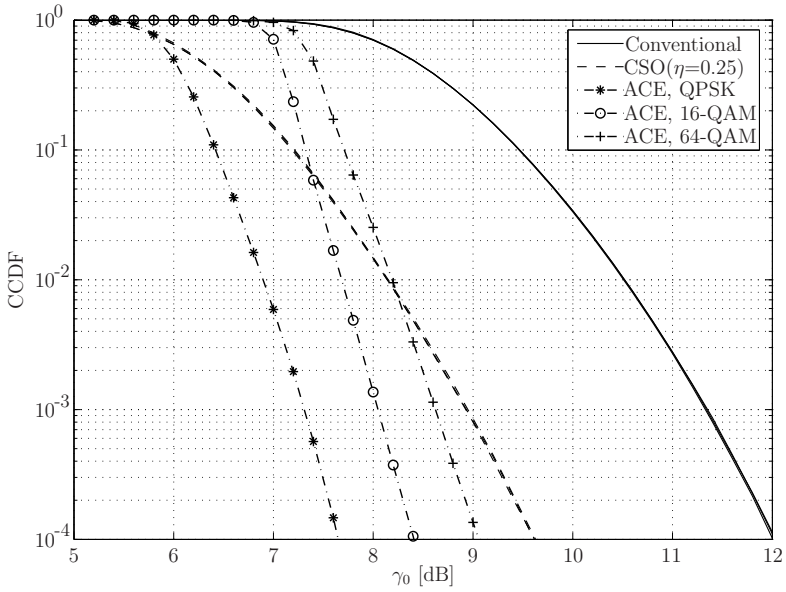

Figure 8.6: PAPR results of the CSO and ACE methods applied to a 256-subcarrier OFDM system.

8.3 Considerations for regulatory restrictions

In this chapter no regulatory restrictions are considered and therefore no spectrum emission masks nor constraints on the power radiated outside the nominal channel are used. This section presents some considerations that should be taken into account when using CSO in systems subject to regulatory restrictions. Nevertheless no results nor specific details of its implementation are provided.

Before defining the regulations regarding radio transmissions to be considered in CSO, one should note that different restrictions will apply depending on the system and equipment under consideration. For instance, in the downlink the base station is using the whole channel bandwidth, therefore, the spectral outgrowth is affecting other channels (i.e. transmissions from other systems). In such a case, when implementing CSO, one must take into account those regulations regarding restrictions on the signal transmitted outside the assigned channel bandwidth, namely *out-of-band emissions*. In the uplink, if FDMA is used for user separation, it is not enough to satisfy the regulations affecting the out-of-band emissions since a large interference might be caused to other user transmissions within the same operating band, specially to those transmitting in adjacent frequency resources. In this case regulations regarding the so-called *in-band emissions* must be considered in CSO. If all frequency resources are assigned to the same user, only those regulations regarding the out-of-band emissions should be considered.

8.3.1 Out-of-band emissions

According to 3GPP RF specifications, which are based on ITU-R recommendations and radio regulations, the *unwanted emissions* are divided into *out-of-band emissions* and *spurious emissions* [4]. The out-of-band emission is defined as "emission on a frequency, or frequencies, immediately outside the necessary bandwidth which results from the modulation process, but excluding spurious emissions" while the spurious emission is defined as "emission on a frequency, or frequencies, which are outside the necessary bandwidth and the level of which may be reduced without affecting the corresponding transmission of information". Spurious emissions include harmonic emissions, parasitic emissions, intermodulation products and frequency conversion products but exclude out-of-band emissions. Of course regulations exist for both type of unwanted emissions but in CSO only those regarding the out-of-band emissions are considered.

According to 3GPP RAN4 specifications there are three ways of specifying the out-of-band emissions, namely *occupied bandwidth*, *spectrum emission mask* and *adjacent channel leakage ratio (ACLR)* [4].

Occupied bandwidth

The occupied bandwidth is defined by ITU-R as the width of a frequency band such that, below the lower and above the upper frequency limits, the mean power emitted are each equal to a specified percentage $\beta/2$ of the total mean power of a given emission. Unless otherwise specified by the Radiocommunication Assembly for the appropriate class of emission, a value of $\beta = 1\%$ should be taken. In such case, the occupied bandwidth is the bandwidth containing the 99% of the total integrated mean power of the transmitted spectrum on the assigned channel. When the occupied bandwidth is used as a regulatory requirement then it can not be larger than the so-called *channel bandwidth*[1] defined in the specifications.

In order to fulfill such regulatory requirement, CSO must be designed so that the power increase resulting from the spectral outgrowth does not exceed 0.0432dB. Note that, the limitation in the spectral outgrowth is defined with respect to the channel bandwidth and not the nominal bandwidth. Therefore, the signal power outside the nominal bandwidth but within the channel bandwidth should not be considered.

Spectrum emission mask

The spectrum emission mask is used to specify the so-called *permissible out-of-band spectrum* of an emission, that is, the power density of emissions above and below the

[1]The channel bandwidth is defined as the RF bandwidth supporting a single RF carrier configured to use a given nominal bandwidth. The nominal bandwidth is the theoretical bandwidth that a given transmission scheme is supposed to occupy. For instance in an OFDM system the nominal bandwidth is defined by $N \cdot \Delta f$, where N is the total number of subcarriers and Δf is the subcarrier spacing. The channel bandwidth is, of course, larger than the nominal one.

necessary bandwidth. The spectrum emission mask does not specify any limits inside the necessary bandwidth, moreover it only applies to frequencies close to the edge of the assigned channel bandwidth. For frequencies far from the edge of the channel bandwidth the spurious requirements are applicable. Due to complexity restrictions in CSO only power at frequencies nearby the nominal bandwidth can be generated, thus, the spurious requirements do not have to be considered.

Adjacent channel leakage ratio

The adjacent channel leakage ratio (ACLR) is the ratio of the filtered mean power centered at the assigned channel frequency to the filtered mean power centered on an adjacent channel frequency. The filter to be used for mean power computation is regulation specific. For instance in 3GPP-LTE both rectangular measurement bandwidth filter and root raised cosine bandwidth filter are contemplated.

It may seem that the ACLR requirement can be obtained by integrating the spectrum emission mask within the assigned and adjacent channel frequencies. Nevertheless, both regulatory requirements are independent and they take into account different restrictions. The purpose of the ACLR requirement is to capture the average behavior over a carrier and therefore to limit the maximum power radiated over the adjacent channels, while the purpose of the spectrum emission mask is to take into account the variations in the spectrum emissions resulting from variations in power allocations. In order to assure that both requirements can be fulfilled at the same time, the ACLR limit is set to be somewhat stricter than the integration of the spectrum emission mask. This means that the spectral outgrowth in CSO can not be designed to be equal to the spectrum emission mask.

8.3.2 In-band emissions

In-band emission regulations must be considered in the FDMA uplink as long as all frequency resources are not assigned to the same user. The in-band emission is a measure of the interference falling into non-allocated frequency resources. According to 3GPP RAN4 specifications, two different measures, and therefore limitations, of the in-band emissions exist, the so-called relative and absolute emissions.

The absolute emission computes the interfering power falling into each non-allocated frequency resource. Within each frequency resource, the corresponding in-band emission is computed by integrating all the interfering components, i.e. by using a rectangular measurement bandwidth filter. In an OFDM-based system this can be easily computed by adding the energy of all the subcarriers within the frequency resource. On the other hand, the relative emission at each frequency resource is the ratio of the corresponding absolute emission and the overall power within allocated frequency resources. The limitations on the maximum allowable in-band emission at each frequency resource are set in such a way that the further the non-allocated frequency resource is

from the allocated one, the lower the interference level is allowed. Figure 8.7 shows an example of in-band emission requirement based on the specifications for 3GPP-LTE uplink. A nominal transmission bandwidth of 9 MHz consisting of 50 frequency resources of 180 KHz each is used. 10 frequency resources in the center of the band are allocated for transmission.

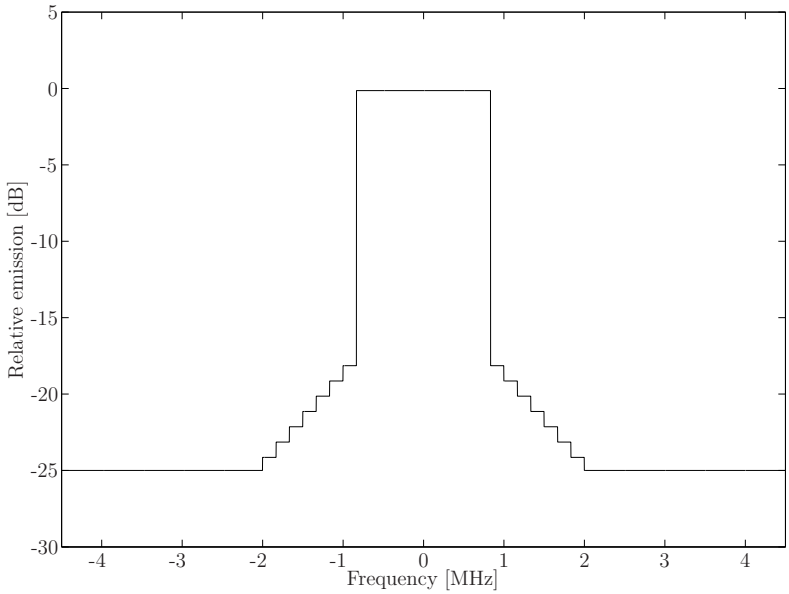

Figure 8.7: Example of in-band emission requirements.

Chapter 9

Multiuser detection of nonlinearly distorted MC-SS signals

There are different strategies to counteract the nonlinear effects in MC and MC-SS systems. In this chapter receiver side techniques to reduce the multiple access interference caused by the nonlinearity are consider. In that sense a new multiuser detector based on microstatistic filtering is proposed. Conventional detectors, such as the minimum mean-squared error MUD (MMSE-MUD), are designed for linear channels and, as a result, might not exhibit enough performance improvement when the multiple access interference is caused by a nonlinear amplification of the transmitted signal. The presented detector uses piece-wise linear filtering in conjunction with threshold decomposition of the input signal, which introduces a nonlinear effect, to improve performance when a nonlinearity is present. As it will be shown the proposed multiuser detector provides better or at least the same performance as a corresponding MMSE-MUD.

The success of spread-spectrum in mobile communications and OFDM in digital broadcasting and wireless LANs motivated many researchers to investigate on the combination of both techniques. As a multicarrier system, MC-SS is very sensitive to nonlinear amplification and therefore it is very important to design efficient techniques to counteract the nonlinear effect. Unlike OFDM systems, MC-SS also exploits the code domain and therefore further techniques must be used. One of the consequences of the nonlinear amplification is that the properties of the spreading sequences are somehow destroyed. Particularly in synchronous MC-SS systems, where orthogonal spreading codes are used to reduce MAI, the nonlinearity destroys the orthogonality thus increasing MAI.

Many techniques can be found in the literature to reduce the sensitivity of MC-SS systems to nonlinear amplification (see Chapter 5). In this chapter we focus on receiver side methods. Receiver side strategies usually combine iterative decoding and multiuser detection so that both nonlinearity compensation and MAI are taken into account [38, 89]. In [89], a MUD that performs a joint detection, estimation and can-

cellation of the nonlinear distortion effects was introduced and in [38], a receiver based on an iterative block decision feedback equalizer, combined with estimation and cancellation of the nonlinear distortion effects was proposed. The major drawback of such solutions is that they increase the receiver complexity significantly. Complexity is mainly given by the number of iterations which, in fact, increases with the number of active users. Moreover these techniques require that predistortion is used at the transmitter side. In order to reduce the complexity, [73] proposes to iteratively optimize the signal constellation of each active user, via a multiuser approach, such that the inter-symbol interference at the relevant decision devices is minimized. However, [73] also requires predistortion at the transmitter side.

In this chapter a novel microstatistic filter based MUD (MSF-MUD) that uses complex-valued multi-channel microstatistic filters (C-M-MSF) for the detection of nonlinearly distorted MC-SS symbols is presented [66]. The key idea is to use a nonlinear but piece-wise linear structure in order to model the nonlinear behavior of the transmitter power amplifier. Then, prior to the detection stage, compensation of the received complex valued symbols is done. The transmitter nonlinearity is modeled by using a training sequence and following the minimum mean-squared error criterion. Simulation results show that the proposed detector outperforms conventional ones [99] when low spreading factors (SF) and user loads no greater than 50% are used. For other system configurations similar performance is obtained. This improvement is achieved with an acceptable increase of the computational complexity in comparison with that of conventional minimum mean-squared error MUD (MMSE-MUD). Moreover, the complexity of a MSF-MUD based receiver is much smaller than those of [38, 73, 89] and, in opposite to those, the proposed scheme neither requires predistortion at the transmitter nor iterative decoding at the receiver.

9.1 Multiuser detection

Multiuser detection refers to the process of demodulating one or more user data streams from a non-orthogonal multiplex [80]. The motivation for multiuser detection is, hence, to reduce the MAI between different data streams (which may belong to different users and applications) before the demodulation stage. For instance, in synchronous transmissions, where different streams are multiplexed in the code domain, orthogonal spreading codes are used and, therefore, one might believe that, in principle, it is not necessary to use multiuser detection techniques since no MAI occurs. However, since the signal at the receiver is corrupted by a time-dispersive channel, the orthogonality at the receiver is lost and therefore MAI occurs, thus requiring the use of MUDs. A nonlinear amplifier also destroys the orthogonality of the spreading codes and therefore it becomes necessary to use multiuser detection techniques.

Even though it is not the objective of this chapter to provide a deep study of the

different multiuser detection strategies, we believe that providing some background is necessary to ease the comprehension of the formulation of MUDs based on microstatistic filtering. Therefore, in the remainder of this section, some basic discussion for the implementation of MUDs will be provided. The reader is referred to [99] for further information.

In this thesis only synchronous MC-SS systems are considered. Following the formulation in Chapter 2, it is assumed that K data symbols are spread by using stream-specific spreading codes of length L_{sc} and transmitted on several narrow-band subcarriers. Let d_m and $\mathbf{c}^{(m)}$ denote the m-th data symbol and the m-th spreading code, the CDMA signal is generated as

$$\mathbf{C} = \sum_{m=0}^{K-1} \mathbf{C}^{(m)} = \sum_{m=0}^{K-1} d_m \mathbf{c}^{(m)}. \tag{9.1}$$

For the sake of simplicity in the mathematical formulation, each chip C_k of the CDMA signal $\mathbf{C} = [C_0, \ldots, C_{L_{\text{sc}}-1}]$ is assumed to be transmitted in the k-th subcarrier. Therefore, the complex amplitude of the k-th subcarrier can be expressed as

$$S_k = C_k = \sum_{m=0}^{K-1} d_m c_k^{(m)}, \qquad k = 0, \ldots, L_{\text{sc}} - 1. \tag{9.2}$$

The most natural strategy to demodulate the different transmitted streams when code division multiplexing is used is by means of a bank of matched filters, as shown in Figure 9.1. Each filter is matched to one of the different spreading codes such that the output of each matched filter is computed as

$$y_m = \left\langle \mathbf{R}, \mathbf{c}^{(m)} \right\rangle = \sum_{k=0}^{L_{\text{sc}}-1} R_k \left(c_k^{(m)} \right)^*, \qquad m = 0, \ldots, K. \tag{9.3}$$

where R_k is the amplitude of the k-th subcarrier at the receiver. In nonlinear AWGN channels R_k is determined as

$$\begin{aligned} R_k &= \frac{1}{\sqrt{N}} \sum_{n=0}^{LN-1} r_n e^{-j2\pi kn/LN} \\ &= \frac{1}{\sqrt{N}} \sum_{n=0}^{LN-1} f(s_n) e^{-j2\pi kn/LN} + W_k, \qquad k = 0, \ldots, N-1, \end{aligned} \tag{9.4}$$

with $f(\cdot)$ being the nonlinear function of the transmitter amplifier and W_k the noise component defined as in equation (4.17).

Let us now assume that a linear amplifier is used, i.e. $f(x) = x$. In such case the expression in (9.4) reduces to $R_k = S_k + W_k$ and, therefore, from (9.2) and (9.3) the

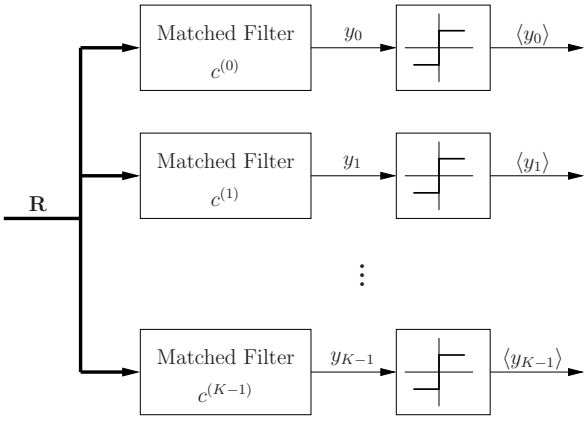

Figure 9.1: Bank of single user matched filters.

output of the m-th matched filter becomes

$$\begin{aligned} y_m &= \sum_{k=0}^{L_{\text{sc}}-1} \left(\sum_{n=0}^{K-1} d_n c_k^{(n)} + W_k \right) \left(c_k^{(m)} \right)^* \\ &= d_m + \sum_{n \neq m} d_n \rho_{nm} + n_m \end{aligned} \tag{9.5}$$

where

$$n_m = \sum_{k=0}^{L_{\text{sc}}-1} W_k \left(c_k^{(m)} \right)^* \tag{9.6}$$

is a Gaussian random variable with zero mean and variance σ_n^2 and

$$\rho_{nm} = \sum_{k=0}^{L_{\text{sc}}-1} c_k^{(n)} \left(c_k^{(m)} \right)^* \tag{9.7}$$

is the correlation between the n-th and m-th spreading codes. Notice that the spreading codes satisfy $\rho_{mm} = 1$. In the case of synchronous transmission orthogonal spreading codes are used. Therefore, $\rho_{nm} = 0,\ n \neq m$ and the matched filter output (9.5) reduces to

$$y_m = d_m + n_m \tag{9.8}$$

which, as in OFDM, it is composed of the transmitted baseband data symbol d_m and a AWGN of power σ_n^2. Since the presence of other users can not decrease the error probability, one concludes that the bank of single-user matched filters is optimal in the special case of synchronous orthogonal CDMA.

Let us now return to nonlinearly distorted MC-SS systems. The orthogonality of the spreading codes is lost after the nonlinearity, therefore, using multiuser detection

techniques is required. A common approach to eliminate the interference between the different spreading codes is by introducing some special signal processing technique between the bank of matched filters and the decision stages as shown in Figure 9.2. A widely accepted solution in estimation theory to the problem of estimating the data symbols being sent d_m on the basis of observations y_m is to choose the function $\hat{d}_m(\mathbf{y})$ that minimizes the mean-squared error,

$$E\left[|d_m - \hat{d}_m(\mathbf{y})|^2\right], \qquad m = 0, \ldots, K-1. \tag{9.9}$$

The notation $\hat{d}_m(\mathbf{y})$ is used to stress that the estimation is based on the output of the matched filters $\mathbf{y}$. Nevertheless, in the remainder the estimated data symbol is referred to as $\hat{d}_m$. According to [99] the MMSE linear detector for the m-th user chooses the length-K vector $\mathbf{m}_m$ that minimizes

$$E\left[|d_m - \mathbf{m}_m^{\mathsf{T}}\mathbf{y}|^2\right], \qquad m = 0, \ldots, K-1. \tag{9.10}$$

We now have K uncoupled optimization problems (one for each data symbol) which can be solved simultaneously by choosing the $K \times K$ matrix $\mathbf{M} = [\mathbf{m}_0, \mathbf{m}_1, \ldots, \mathbf{m}_{K-1}]$ that achieves

$$\min_{\mathbf{M} \in \mathbb{C}^{K \times K}} E\left[||\mathbf{d} - \mathbf{M}\mathbf{y}||^2\right], \tag{9.11}$$

where the output of the bank of mathed filters, $\mathbf{y}$, is expressed as

$$\mathbf{y} = \mathbf{\Gamma}\mathbf{d} + \mathbf{n} \tag{9.12}$$

and $\mathbf{\Gamma}$ is the correlation matrix of the nonlinearly distorted spreading codes and $\mathbf{n}$ is the noise vector with zero mean and covariance matrix equal to $\sigma_n^2\mathbf{\Gamma}$. The reader should note that since orthogonal spreading codes are used, the expression of the output of the bank of matched filters when a nonlinearity is present at the transmitter side, (9.12), is equal to that previously derived in (9.8) for linear amplification but considering the cross-correlation terms due to the loss of orthogonality caused by the nonlinear amplifier. It can be shown that, assuming the average power of the received data symbols is $\sigma^2 = 1$, the matrix $\mathbf{M}$ that satisfies (9.11) is [99]

$$\mathbf{M} = [\mathbf{\Gamma} + \sigma_n^2\mathbf{I}^{K \times K}]^{-1} \tag{9.13}$$

and, therefore, the decision variables are obtained as

$$\hat{\mathbf{d}} = [\mathbf{\Gamma} + \sigma_n^2\mathbf{I}^{K \times K}]^{-1}\mathbf{y}, \tag{9.14}$$

where $\mathbf{I}^{K \times K}$ is the $K \times K$ identity matrix. Both $\mathbf{\Gamma}$ and σ_n can be computed by using a training sequence prior to the transmission of the information. For further information refer to [99].

An intuitive approach to eliminate the interference caused by any of the other streams can be derived by directly observing the output of the bank of matched filters

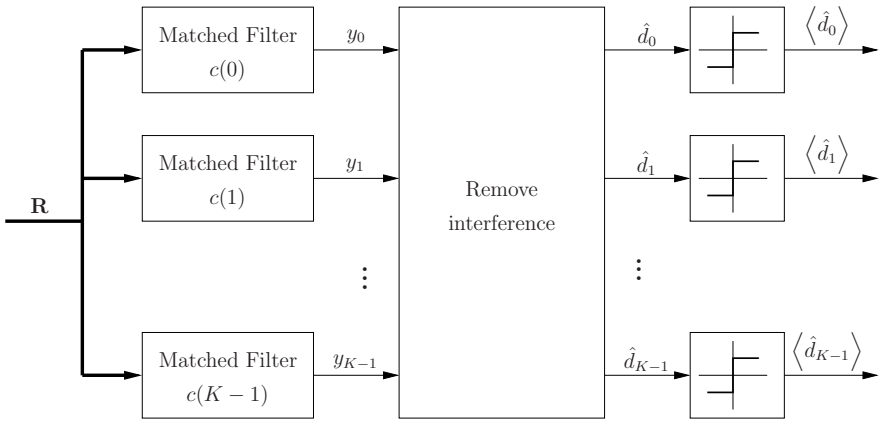

Figure 9.2: Multiuser detector.

in (9.12). Note that if the received signal is not corrupted by noise, the decision variables can be easily obtained by multiplying the output of the matched filters by the inverse of the correlation matrix $\mathbf{\Gamma}$ as

$$\hat{\mathbf{d}} = \mathbf{\Gamma}^{-1}\mathbf{y}, \tag{9.15}$$

Since $\mathbf{\Gamma}$ is the responsible for the correlation that introduces MAI, by multiplying with the inverse of the correlation matrix, the output of the matched filters is, thus, decorrelated. Therefore, this solution is referred in the literature to as decorrelating detector [99]. It can be observed by comparing (9.14) and (9.15) that both solutions are similar except that in the latter the noise term in not taken into account[1].

So far, three types of detection strategies have been addressed, namely single-user matched filter, decorrelating multiuser detector and MMSE linear multiuser detector. The single-user matched filter receiver is optimized to fight the background white noise exclusively, whereas the decorrelating detector is designed to eliminate the multiuser interference disregarding the background noise. In contrast, the MMSE linear detector can be seen as a compromise solution that takes into account the relative importance of each interfering user and the background noise. In fact, as shown in [99], both the conventional receiver and the decorrelating receiver are limiting cases of the MMSE linear detector. A common characteristic of the two multiuser detectors that have been previously formulated is that the decision variables are obtained from linear transformations of the signal at the output of the bank of matched filters. Generally, the major source of MAI in orthogonal CDMA systems is generated by the time-dispersive channel. Since a time dispersive channel produces a linear transformation of the signal being sent, it seams reasonable to assume that such multiuser detectors will show a good performance. On the other hand, when the loss of orthogonality is generated by means of nonlinear signal processing, such as in a nonlinear amplifier, it is doubtful that it can be

[1]In fact, the decorrelating detector is derived without assuming the noise component.

solved my means of linear signal processing. This is the major motivation for our work.

9.2 Piecewise linear filtering

The previous section provided some background regarding multiuser detection that is necessary to understand the proposed MUD. Nevertheless, before considering the formulation of MSF-based MUDs, the implementation of microstatistic filters (MSF) must be described. This will be addressed in the remainder of this section according to the proposals in [7] and [71].

A non-recursive discrete-time filter is represented by the equation

$$y_n = \sum_{i=0}^{q-1} a_i x_{n-i}, \tag{9.16}$$

where x_n is the input signal and $a_0, a_1, \ldots, a_{q-1}$ are the filter coefficients. In microstatistic filtering the input signal x_n is threshold decomposed into L_{th} subsignals $\tilde{x}_n(j),\ j = 1, 2, \ldots, L_{\text{th}}$ in such way that the expression

$$x_n = \sum_{j=1}^{L_{\text{th}}} \tilde{x}_n(j) \tag{9.17}$$

is satisfied[2]. The signal at the output of the piecewise linear (PWL) filter is computed as

$$y_n = \sum_{i=0}^{q-1} \mathbf{a}_i^{\mathsf{T}} \mathbf{T}\mathbf{D}(x_{n-i}) = \sum_{i=0}^{q-1} \mathbf{a}_i^{\mathsf{T}} \tilde{\mathbf{x}}_{n-i} \tag{9.18}$$

where $\tilde{\mathbf{x}}_n = [\tilde{x}_n(1), \ldots, \tilde{x}_n(L_{\text{th}})]^{\mathsf{T}}$ is the threshold decomposition of x_n and $\mathbf{a}_i,\ i = 0, 1, \ldots, q-1$, are the vector coefficients of length L_{th}. Notice that in (9.16) the filter coefficients were scalars a_i multiplying x_{n-i}. When threshold decomposition is done a different scalar, denoted as $a_i(j)$, is used to multiply each segment of the input signal $\tilde{x}_{n-i}(j)$, with $i = 0, 1, \ldots, q-1$ and $j = 1, 2, \ldots, L_{\text{th}}$. Let us define

$$H_j(z) = \sum_{i=0}^{q-1} a_i(j) z^{-i}. \tag{9.19}$$

Then, as shown in Figure 9.3 the PWL filter in (9.18) can be represented as a sequence of three operations in cascade: signal threshold decomposition (also referred to as segmentation), linear multichannel filtering and a final addition.

[2]A more detailed explanation of the threshold decomposition procedure will be addressed later. Moreover, as it will be seen, segmentation into L_{th} subsignals is used when the input signal is complex valued. For real signals $2L_{\text{th}}$ segments are used.

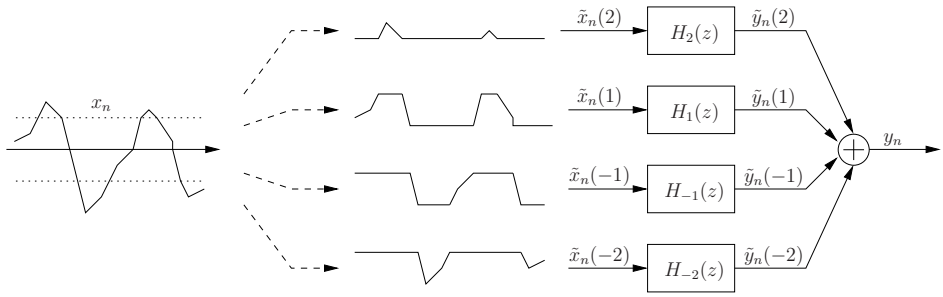

Figure 9.3: Block scheme of the conventional microstatistic filter.

The parameter set for these filters is composed of two different entities, namely the length-q vector coefficients $\{\mathbf{a}_i\}$ and the $L_{\text{th}} - 1$ thresholds used for segmentation $\{\lambda_j\}$. There are several strategies to determine the parameter set such as least squares estimation [71]. Nevertheless, the details concerning the design procedure will be addressed in Section 9.3, specifically for multiuser detection.

9.2.1 Threshold decomposer

Let us first assume a real PWL filter. In that case the real threshold decomposer, **rTD**, decomposes the real input signal x_n into $2L_{\text{th}}$ signals,

$$\mathbf{rTD}(x_n) = [\tilde{x}_n(-L_{\text{th}}), \ldots, \tilde{x}_n(-1), \tilde{x}_n(1), \ldots, \tilde{x}_n(L_{\text{th}})]^{\mathsf{T}}, \tag{9.20}$$

in such a way that each signal $\tilde{x}_n(j)$ just contains the part of the signal with an amplitude in the corresponding interval. Notice that the real segmentation of x_n into the $2L_{\text{th}}$ output signals $\tilde{x}_n(j)$ is denotted as $\mathbf{rTD}(x_n)$. Let us now define the vector

$$\mathbf{L} = [l(-L_{\text{th}}), \cdots, l(-1), l(0), l(1), \cdots, l(L_{\text{th}})]^{\mathsf{T}} \tag{9.21}$$

as the real-valued threshold levels of the threshold decomposer, which satisfy $l(-L_{\text{th}}) < \cdots < l(-1) < l(0) < l(1) < \cdots < l(L_{\text{th}})$ with $l(-L_{\text{th}}) = -\infty$, $l(L_{\text{th}}) = \infty$ and $l(0) = 0$. To compute the output signals of the threshold decomposer, one must first check whether x_n is positive or negative. If x_n is positive then the negative segments are set to 0, i.e. $\tilde{x}_n(j) = 0$ for $j = -L_{\text{th}}, -L_{\text{th}} + 1, \ldots, -1$, and the positive segments are computed as

$$\tilde{x}_n(j) = \begin{cases} 0 & \text{if } x_n < l(j-1) \\ x_n - l(j-1) & \text{if } l(j-1) \le x_n < l(j) \\ l(j) - l(j-1) & \text{if } l(j) \le x_n \end{cases} \tag{9.22}$$

for $j = 1, 2, \ldots, L_{\text{th}}$. On the other hand, if x_n is negative then $\tilde{x}_n(j) = 0$ for $j = 1, 2, \ldots, L_{\text{th}}$, and

$$\tilde{x}_n(j) = \begin{cases} 0 & \text{if } x_n > l(j+1) \\ x_n - l(j+1) & \text{if } l(j+1) \ge x_n > l(j) \\ l(j) - l(j+1) & \text{if } l(j) \ge x_n \end{cases} \tag{9.23}$$

for $j = -L_{\text{th}}, -L_{\text{th}}+1, \ldots, -1$.

Let us now consider the decomposition of complex signals. Analogous to the real case, the complex threshold decomposer, **cTD**, decomposes the complex input signal x_n into L_{th} signals, as

$$\mathbf{cTD}(x_n) = [\tilde{x}_n(1), \ldots, \tilde{x}_n(L_{\text{th}})]^{\mathsf{T}}, \tag{9.24}$$

in such way that the expression in (9.17) is satisfied. In order to define the behavior of a complex threshold decomposer, let us assume that the complex-valued signal x_n is expressed in the form

$$x_n = X_n e^{j\phi_n} \tag{9.25}$$

where $X_n = |x_n|$ and $\phi_n = \arg(x_n)$. According to [64] only the modulus of the complex signal should be segmented, since performing a threshold decomposition of ϕ_n does not result in any clear benefit as the phase term is uniformly distributed over the interval $[-\pi, \pi)$. Therefore, the general expression of a complex decomposer in (9.24) can be rewritten as

$$\begin{aligned} \tilde{\mathbf{x}}_n &= \mathbf{cTD}(x_n) = [\tilde{x}_n(1), \ldots, \tilde{x}_n(L_{\text{th}})]^{\mathsf{T}} \\ &= \mathbf{rTD}(X_n)e^{j\phi_n} = [\tilde{X}_n(1), \ldots, \tilde{X}_n(L_{\text{th}})]^{\mathsf{T}} e^{j\phi_n} \end{aligned} \tag{9.26}$$

where $\tilde{x}_n(j) = \tilde{X}_n(j)e^{j\phi_n}$ and the segmentation of the absolute value of x_n is computed as

$$\tilde{X}_n(j) = \begin{cases} 0 & \text{if } X_n < l(j-1) \\ X_n - l(j-1) & \text{if } l(j-1) \le X_n < l(j) \\ l(j) - l(j-1) & \text{if } l(j) \le X_n \end{cases} \tag{9.27}$$

for $j = 1, 2, \cdots, L_{\text{th}}$, since X_n is always a non-negative value and, thus the negative segments ($j < 0$) are meaningless. As a result, the parameters $l(j)$ constituting the vector $\mathbf{L} = [l(1), \cdots, l(L_{\text{th}})]^{\mathsf{T}}$ are the positive real-valued threshold levels of the threshold decomposer, which satisfy $0 = l(0) < l(1) < \ldots < l(L_{\text{th}}) = \infty$ [65].

9.2.2 Linear multichannel filtering

The second step in a PWL filter, after threshold decomposition, is the linear multichannel filtering. Here each segment is filtered separately by using a different so-called *microstatistic filter*. It is not the purpose of this section to provide a deep study of microstatistic filtering, therefore the reader is referred to [7] and [71] for further details. Instead, we will see how can the original formulation presented in [7] be modified to obtain a filtering structure more suitable for our multiuser detection problem.

According to (9.18) the signal at output of each microstatistic filter is computed as

$$\tilde{y}_n(j) = \sum_{i=0}^{q-1} a_i(j)\tilde{x}_{n-i}(j) \tag{9.28}$$

and thus the output signal of the PWL filter can be expressed as

$$y_n = \sum_{j=1}^{L_{\text{th}}} \sum_{i=0}^{q-1} a_i(j)\tilde{x}_{n-i}(j). \tag{9.29}$$

Let us observe that each sample of the output signal y_n is computed by adding all the signals at the outputs of the L_{th} microstatistic filters, $\tilde{y}_n(j)$, and that at the same time they are computed by filtering the corresponding input segment. Therefore, each sample of the output signal y_n is computed by considering all the samples of threshold decomposed signals at present and previous instants (up to $q-1$ instants before). Let us now assume that instead of having a continuous input signal x_n we have a length-N block-based signal $x_n^{(m)}$ where m is the block index and the blocks are independent from each other. Then, the filtering should be done within the N samples that constitute each block and, moreover, it could consider both previous and later samples to the one being filtered. In that case the n-th sample of the m-th output block signal of the PWL filter could be expressed as

$$y_n^{(m)} = \sum_{j=1}^{L_{\text{th}}} \sum_{i=0}^{N} h_{i,n}(j)\tilde{x}_i^{(m)}(j), \tag{9.30}$$

where $h_{i,n}(j)$ is the filter coefficient that weighs the contribution of the j-th segment of the i-th input sample to the n-th output sample. This is depicted in Figure 9.4 and it is the basis for MSF-based multiuser detection. Notice that for simplicity the block index m is not shown.

9.3 MSF-based MUD

In Section 9.1 some background for the implementation of MUDs was provided. Later, in Section 9.2, the concept of microstatistic filtering was addressed and also a modification of the original formulation for block-based signals was presented. In this section, the previous concepts will be merged to implement a MSF-based MUD. According to [62] microstatistic filtering is a promising technique for the implementation of MUDs since a good sub-optimum performance with reduced complexity can be achieved.

Figure 9.5 shows the block scheme of a MSF-based MUD. First the frequency-domain MC-SS signal at the output of the OFDM block is fed to a bank of matched filters. As in conventional multiuser detection each filter is matched to one of the different spreading codes such that the output of each matched filter is computed as described in (9.3). The output signals of the matched filters are then fed to a C-M-MSF which is designed to remove the interference between the different streams. The output of the C-M-MSF are the decision variables used in the demodulation stage. As it can be observed, a MSF-based MUD has the same structure as an MMSE or

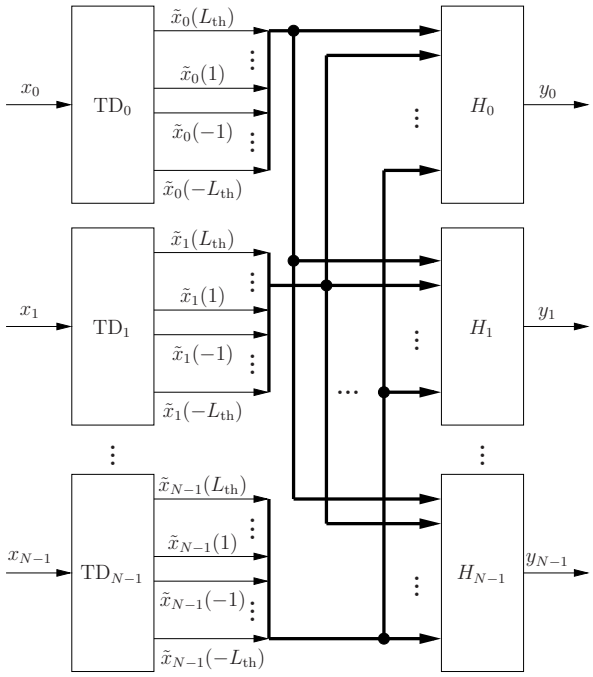

Figure 9.4: Block scheme of the modified multichannel microstatistic filter.

decorrelating receiver. However, in the MSF-MUD a C-M-MSF is placed between the bank of matched filters and the decision stages.

In the remainder of this section, a more specific formulation of the MSF for multiuser detection will be given. Note that since the MSF is now part of the multiuser detection stage a different nomenclature than that used in Section 9.2 will be considered. As it can be observed in Figure 9.5 the C-M-CMF is formed by K complex-valued threshold decomposers and a set of K multi-channel Wiener filters (WF). The input variables are denoted as $y_k,\ k = 0, 1, \ldots, K-1$. After threshold decomposition, the notation $\tilde{y}_k(j),\ k = 0, 1, \ldots, K-1$ and $j = 1, 2, \ldots, L_{\mathrm{th}}$ is used to denote the j-th segment of the k-th input variable. The threshold decomposer $\mathbf{TD}_k$ is used to decompose the k-th input variable. Finally, the m-th output variable, generated by the m-th Wiener filter, is denoted as $\hat{d}_m,\ m = 0, 1, \ldots, K-1$. Notice that the subindex k is used to distinguish the different input variables and threshold decomposers, while m is used for the output variables and Wiener filters. Both k and m may take any integer value in the range $[0, K-1]$.

9.3.1 Threshold decomposers

The variables at the output of the matched filter will, in general, be complex-valued and therefore complex segmentation must be done. According to Section 9.2.1 and by considering the nomenclature used for multiuser detection, the output of the k-th

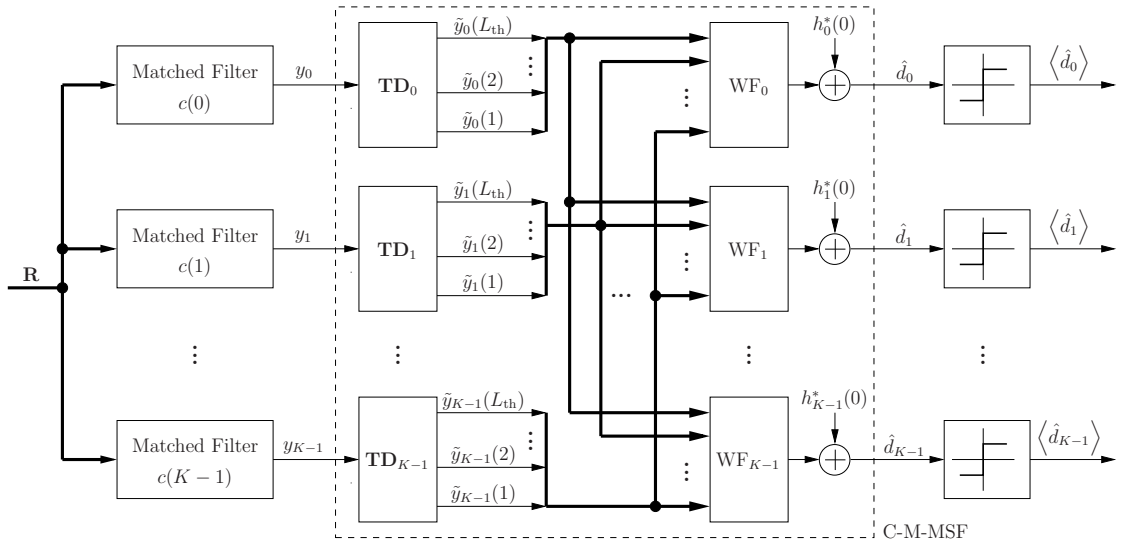

Figure 9.5: Block scheme of a MSF-based MUD.

threshold decomposer is computed as

$$\begin{aligned}\tilde{\mathbf{y}}_k &= \mathbf{TD}_k(y_k) = [\tilde{y}_k(1), \ldots, \tilde{y}_k(L_{\text{th}})]^{\mathsf{T}} \\ &= [\tilde{Y}_k(1), \ldots, \tilde{Y}_k(L_{\text{th}})]^{\mathsf{T}} e^{j\phi_k}\end{aligned} \tag{9.31}$$

where $\tilde{y}_k(j) = \tilde{Y}_k(j)e^{j\phi_k}$, $\phi_k = \arg(y_k)$ and $\tilde{Y}_k(j)$ is the j-th segment of Y_k computed as

$$\tilde{Y}_k(j) = \begin{cases} 0 & \text{if } Y_k < l_k(j-1) \\ Y_k - l_k(j-1) & \text{if } l_k(j-1) \le Y_k < l_k(j) \\ l_k(j) - l_k(j-1) & \text{if } l_k(j) \le Y_k \end{cases} \tag{9.32}$$

for $j = 1, 2, \cdots, L_{\text{th}}$. Let us recall that the parameters $l_k(j)$ constituting the vector $\mathbf{L}_k = [l_k(1), \cdots, l_k(L_{\text{th}})]^{\mathsf{T}}$ are the positive real-valued threshold levels of the k-th threshold decomposer, which satisfy $0 = l_k(0) < l_k(1) < \ldots < l_k(L_{\text{th}}) = \infty$ [65]. The reader should note that since a different threshold decomposer is used for each of the K input signals, they might have a different configuration. Nevertheless, in most practical situations the segmentation of all the input variables can be done by using the same thresholds, i.e. all threshold decomposers may have the same configuration.

9.3.2 Wiener filters

In Section 9.2, the PWL filter was reformulated to consider block-based signals. Moreover, it was claimed that the new formulation, in opposite to the conventional one, should be considered for MSF-based multiuser detection. Let us now discuss the suitability of the new formulation. In a MC-SS system, a given number of data symbols is transmitted within each OFDM symbols. Due to the properties of OFDM no interference is generated between data symbols from different OFDM symbols and thus

it is not necessary to consider the data symbols that are transmitted in other OFDM blocks. Moreover, it should be taken into account that when the orthogonality of the spreading codes is lost, interference to all the data symbols within the same OFDM block is generated. Therefore, it is more convenient to use the modified MSF structure rather than the original one.

The reader should note that the objective of the microstatistic filters in multiuser detection is to filter out the interference that has corrupted the decision variables. As it will be subsequently described, to achieve it special training sequences will be used in order to obtain the statistical properties of both the desired and interfering signals with the aim of achieving a MMSE estimation of the decision variables. In fact this type of filtering is widely employed in signal processing by means of the so-called Wiener filters. Therefore, in the remainder, the microstatistic filters will be referred to as Wiener filters.

The signals obtained after threshold decomposition are fed into the set of K multichannel Wiener filters. From (9.30) and by considering the modification introduced in Figure 9.5, the output of the m-th Wiener filter is computed as

$$\hat{d}_m = (h_m(0))^* + \sum_{j=1}^{L_{\text{th}}} \sum_{k=0}^{K-1} (h_{k,m}(j))^* \, \tilde{y}_k(j), \tag{9.33}$$

where $h_{k,m}(j)$ is the filter coefficient that weighs the contribution of the j-th segment of the k-th input sample to the m-th output sample. Moreover a constant term $h_m(0)$ is applied to the C-M-MSF structure in order to obtain an unbiased estimation of the desired signal at the output of the m-th Wiener filter. Let the response of the m-th Wiener filter be

$$\mathbf{H}_m = [h_m(0), \mathbf{h}_{0,m}^{\mathsf{T}}, \mathbf{h}_{1,m}^{\mathsf{T}}, \cdots, \mathbf{h}_{K-1,m}^{\mathsf{T}}]^{\mathsf{T}}, \tag{9.34}$$

$$\mathbf{h}_{k,m} = [h_{k,m}(1), h_{k,m}(2), \ldots, h_{k,m}(L_{\text{th}})]^{\mathsf{T}} \tag{9.35}$$

where $m = 0, 1, \ldots, K-1$ and $\mathbf{h}_{k,m}$ is a vector with the filter coefficients that weigh the contribution of the L_{th}-segments of the k-th input sample to the m-th output sample. Let the input signal of the Wiener filters be

$$\tilde{\mathbf{Y}} = [1, \tilde{\mathbf{y}}_0^{\mathsf{T}}, \tilde{\mathbf{y}}_1^{\mathsf{T}}, \cdots, \tilde{\mathbf{y}}_{K-1}^{\mathsf{T}}]^{\mathsf{T}}, \tag{9.36}$$

where $\tilde{\mathbf{y}}_k$ is the output of the k-th threshold decomposer as defined in (9.31). Then, the expression of the output of the m-th Wiener filter, WF_m, in (9.33) can be rewritten as

$$\hat{d}_m = \mathbf{H}_m^{\mathsf{H}} \tilde{\mathbf{Y}}. \tag{9.37}$$

where the superscript H denotes Hermitian transposition.

9.3.3 Design procedure

Before being able to use the microstatistic filter one has to determine the threshold levels and the coefficients of the Wiener filters. This is done by transmitting a special training sequence and by following the MMSE criterion. Let us define the set of threshold levels from all threshold decomposers as $\mathbf{L} = [\mathbf{L}_0; \mathbf{L}_1; \cdots; \mathbf{L}_{K-1}]$. Then, according to the MMSE criterion, the optimum values for $\mathbf{L}$ and $\mathbf{H}_m$ are obtained as the solution that minimizes the cost functions

$$\mathrm{MSE}(\mathbf{H}_m, \mathbf{L}) = E\left[e_m e_m^*\right], \tag{9.38}$$

where $e_m = d_m - \hat{d}_m$, d_m is the desired data symbol at the output of the m-th Wiener filter and $\hat{d}_m$ is the estimated data symbol according to (9.37). Let us recall from Section 9.3.1 that in multiuser detection the segmentation of all input variables can generally be done by using the same thresholds. In such cases, the set of threshold levels from all threshold decomposers is defined as $\mathbf{L} = \mathbf{L}_0 = \mathbf{L}_1 = \cdots = L_{K-1}$, instead of concatenating the values of all the threshold decomposers. This, simplifies the design of the MSF-based MUD without any loss of performance.

Before $\mathrm{MSE}(\mathbf{H}_m, \mathbf{L})$ minimization, it is necessary to determine the number of threshold levels that are used for segmentation, i.e. L_{th}. Generally, this will represent a trade-off between the expected performance of the MSF-based MUD and the complexity requirements. The solution of the optimization problem can be obtained by means of an iterative process, where each iteration consists of three basic steps [65]. In the first step, the vector $\mathbf{L}$ is estimated. Several methods can be found in the literature to determine the threshold levels. However, since providing a broad study of microstatistic filters lies behind the scope of this thesis the reader is referred to [63] for further information. In the second step, the optimum coefficients of the K Wiener filters are computed based on the estimation of the vector $\mathbf{L}$ as

$$\mathbf{H}_k^{\mathrm{MSE}} = \mathbf{R}^{-1}\mathbf{P}_k, \tag{9.39}$$

where $\mathbf{R} = E\left[\tilde{\mathbf{Y}}\tilde{\mathbf{Y}}^{\mathsf{H}}\right]$ is the autocorrelation matrix of the input variables of the Wiener filter, $\tilde{\mathbf{Y}}$, and $\mathbf{P}_k = E\left[d_k\mathbf{Y}\right]$ is the cross-correlation vector of the desired data symbols d_k and $\mathbf{Y}$. Both, $\mathbf{R}$ and $\mathbf{P}_k$ are estimated by using a training sequence. During the last step, the cost functions in (9.38) are evaluated to determine whether another iteration is required or not. The iterative process is stopped either when the cost functions are minimized or the error is acceptable from an application point of view. In such case, the resulting values for $\mathbf{L}$ and $\mathbf{H}_k^{\mathrm{MSE}}$ are used for microstatistic filtering. The reader is referred to [66], [65] and [63] for further details regarding the design procedure of C-M-CMF.

Even though the above described algorithm is able to determine the optimum parameters of the C-M-CMF under MMSE criterion, the associated complexity is too large for a practical implementation. Thus, a suboptimum solution is used in this

chapter to significantly reduce both the required complexity while at the same scarcely reduce performance. This solution relies on the fact that, according to simulation results, the threshold levels can be found independently of the system configuration (baseband modulation, spreading factors, etc). Thus, the training algorithm will only have to determine the coefficients of the Wiener filter, that is, only run the second and third steps of the above described iterative process.

The structure of a MSF-based MUD is very similar to that of a conventional linear MMSE-MUD [99]. In fact, it was previously shown that MSF-based MUDs can be obtained from linear MMSE-MUDs by just substituting the set of multi-channel linear filters in the MMSE-based MUD, located between the bank of matched filters and decision devices, by the C-M-MSF. It is interesting to notice that MMSE-based MUDs are a special case of MSF-based MUDs where $L_{\text{th}} = 1$, i.e. no threshold decomposition is done. As a result, it seems reasonable to assume that MSF-based MUD has to provide better or at least the same performance than a corresponding linear MMSE-MUD. This is achieved at the expense of higher computational complexity requirements at the receiver. The complexity of the MSF-based MUD is greater than that of the linear MMSE-MUD in $(L_{\text{th}} - 1)K$ complex-valued MAC. Further details concerning MSF-MUD can be found in [63].

9.4 Performance evaluation

In the remaining of this chapter the performance of the proposed MSF-based MUD when a nonlinearity is present will be evaluated [66]. The remainder of this section is organized as follows. First the configuration of the MC-SS system under consideration is described. Then the choice of the MSF parameters is discussed and the performance improvement capabilities with respect to a linear MMSE-receiver is evaluated. Finally, some numerical computations of bit error probabilities in AWGN channels with nonlinear amplification are presented.

9.4.1 System configurations

In this chapter we setup a conventional MC-CDMA system, operating at different user loads, with length-16 and length-32 Hadamard spreading codes and 16-QAM, 64-QAM and 256-QAM baseband modulation schemes. A downlink scenario is considered, thus, perfect user synchronization is assumed. In order to minimize the performance degradation introduced by the nonlinearity the spreading sequences are chosen so that average PAPR is minimized. Moreover, according to [57] an oversampling rate of $L = 4$ is used to avoid aliasing the out of band distortion into the data bearing tones.

Two major types of power amplifiers are typically used in wireless communication systems, TWTA and SSPA [57]. Comparatively, TWTA introduces more significant

distortion than SSPA. Since our intention is to provide stringent conditions to evaluate algorithms, TWTA will be considered. In this chapter we use the widely accepted Saleh baseband model for TWTA [86] defined by the amplitude-to-amplitude modulation and amplitude-to-phase modulation characteristics in (3.24) and (3.25), with $\kappa_G = 2$, $\chi_G = \chi_\Phi = 1$ and $\kappa_\Phi = \pi/3$.

At the receiver side, a conventional MMSE-MUD and the proposed MSF-MUD are used. The complexity of MSF-MUD is $\mathcal{O}(L_{\text{th}}K)$ MAC operations. In order to minimize the complexity requirements just one threshold level is used for decomposition, i.e. L_{th}=2. Thus, the complexity of the MSF-MUD application described in this chapter is $\mathcal{O}(2K)$ MAC operations. Which means that the complexity requirements with respect to MMSE-MUD is increased in just one MAC per user.

9.4.2 Choice of the parameters and performance

In this section we first discuss choice of the parameters in the C-M-MSF with the aim of increasing the performance of the proposed MUD and, then, evaluate the performance improvement capabilities with respect to a conventional MMSE-MUD based receiver. Performance evaluation is computed by means of error vector magnitude (EVM) of the constellation at the output of the MUD. Let $\hat{d}_k$ and d_k denote the constellation point at the output of the MUD and the ideally received constellation point, respectively, EVM is computed as

$$\text{EVM} = 10\log_{10}\left(E[|\hat{d}_k - d_k|^2]/P_{ref}\right) \tag{9.40}$$

where P_{ref} is the power of the outmost ideal constellation point.

Let us start by determining the parameters of the C-M-MSF. The complexity associated with determining the optimal parameters might be too high for a practical implementation. Nevertheless, if the threshold levels can be determined during the design of the system, then the receiver will only have to compute the response of the Wiener filters, given a predefined threshold decomposition, thus reducing the complexity considerably. In Figure 9.6 the EVM reduction of the proposed MSF-MUD with respect to MMSE-MUD as a function of the threshold level is shown. As it can be seen, maximum performance improvement is obtained when a relative threshold level around 0.6 is used. It is important to state that extensive simulations have been done to determine the threshold levels that provide best performance for each system configuration even though, for the sake of simplicity, only some simulation results are shown. In fact, after evaluating the extensive simulation results, on realizes that, when Hadamard codes are used, maximum performance is generally obtained if the threshold level is set to 0.6, independently of the back-off, baseband modulation, spreading factor and user load. For the remaining cases, the performance degradation with respect to the optimum relative threshold level was so small that could be neglected.

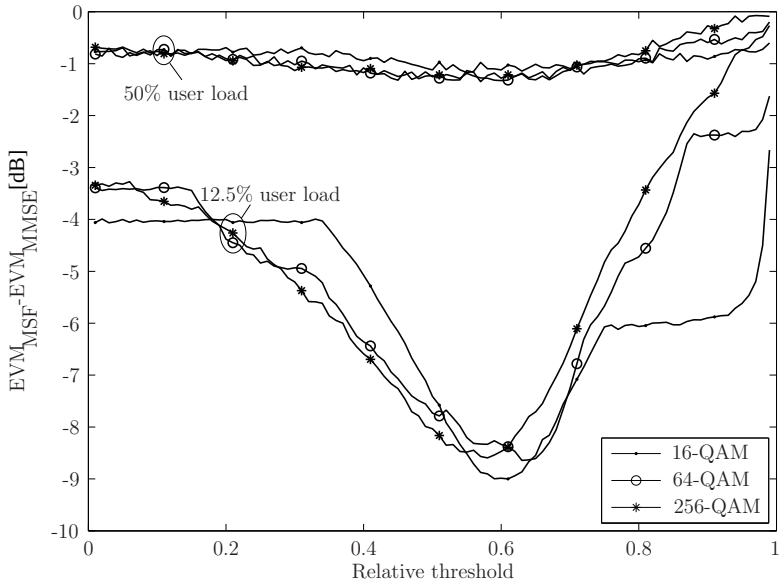

Figure 9.6: EVM reduction with respect to MMSE-MUD as a function of the threshold level. 16, 64 and 256-QAM, length-32 Hadamard codes with 12.5% and 50% user loads, and Saleh NL operating at IBO=20dB are used.

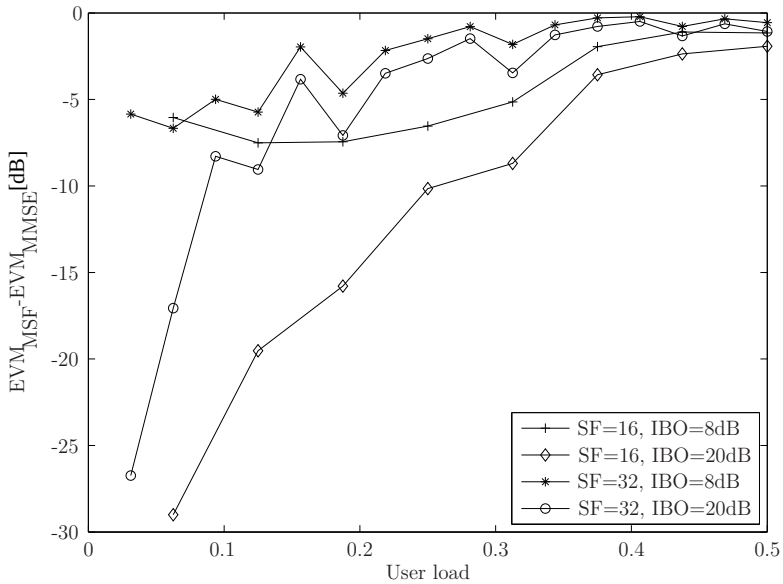

Figure 9.7: EVM reduction with respect to MMSE-MUD as a function of the user load. Hadamard codes of length 16 and 32, 16-QAM baseband modulation and Saleh NL operating at IBO=8dB and IBO=20dB are used.

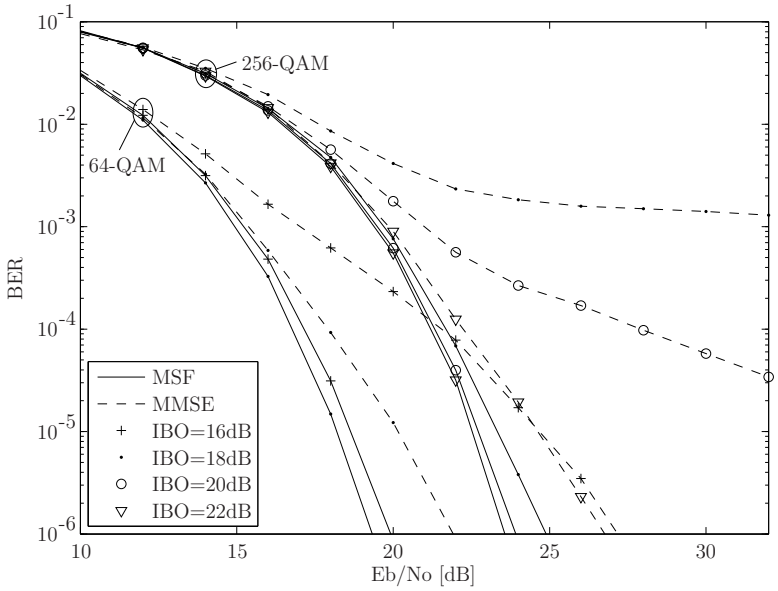

Figure 9.8: BER performance of a nonlinearly distorted MC-CDMA system using MSF-MUD and MMSE-MUD. 12.5% user load and SF=16 are used.

Another important aspect to notice in Figure 9.6 is that, independently of the relative threshold level, the performance of the proposed MUD is always better than or, at least, equal to that of MMSE-MUD. This is further analyzed in Figure 9.7 where EVM reduction using different user loads and system configurations is evaluated. Here, 16-QAM and a threshold level of 0.6 are used. Although simulation results show that the performance of the proposed MUD is never worse than that of conventional MMSE-MUD, it can be seen that a high performance improvement is only obtained for low user loads and low spreading factors.

9.4.3 Numerical results

In this section the BER characteristics of the proposed MSF-MUD are evaluated using different system configurations. Moreover, in order to compare the performance of both detectors, the error rate of a conventional MMSE-MUD is also computed. According to the conclusions from Section 9.4 the MSF-MUD is configured to use a relative threshold level equal to 0.6 independently of the system configuration.

Figure 9.8 to Figure 9.10 show the BER characteristics of a nonlinearly distorted MC-CDMA system using length-16 Hadamard spreading codes with 12.5%, 31.25% and 50% user loads, respectively. It can be seen that for both low spreading factors and low to moderate user loads (see Figure 9.8 and Figure 9.9) a high performance improvement, in terms of BER, is obtained by using MSF-MUD compared to MMSE-MUD. Let us first evaluate the back-off requirements to achieve BER performances close to those obtained in linear AWGN channels. For MMSE-MUD and 64-QAM(256-QAM),

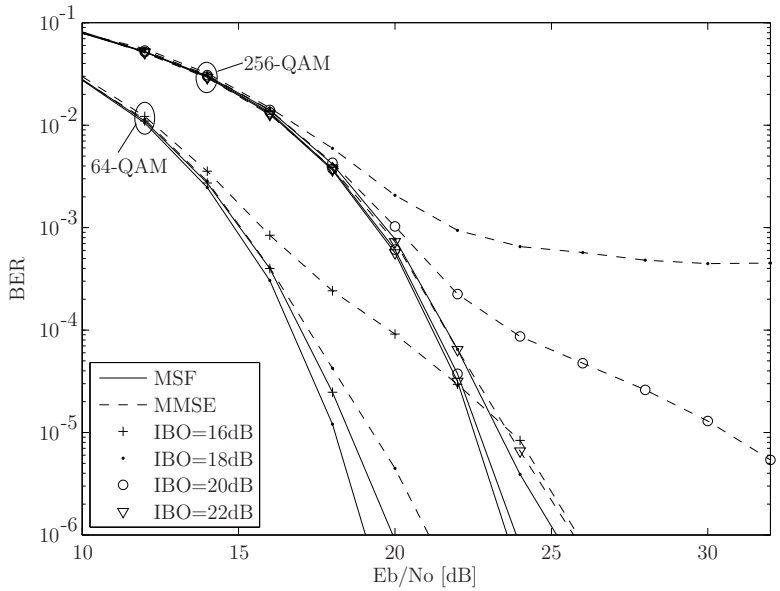

Figure 9.9: BER performance of a nonlinearly distorted MC-CDMA system using MSF-MUD and MMSE-MUD. 31.25% user load and SF=16 are used.

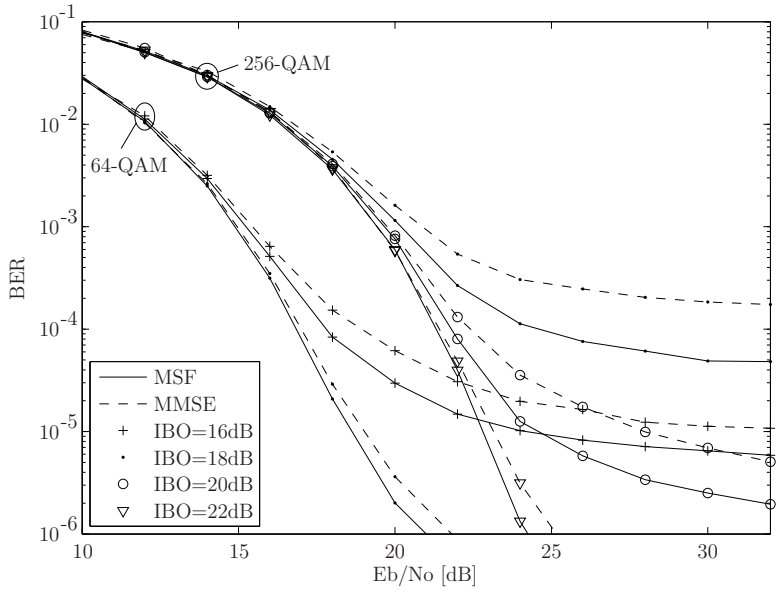

Figure 9.10: BER performance of a nonlinearly distorted MC-CDMA system using MSF-MUD and MMSE-MUD. 50% user load and SF=16 are used.

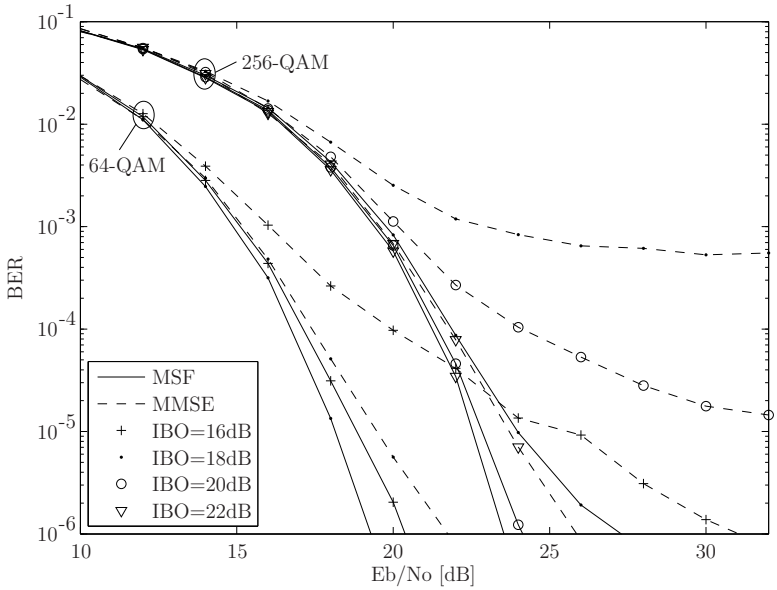

Figure 9.11: BER performance of a nonlinearly distorted MC-CDMA system using MSF-MUD and MMSE-MUD. 12.5% user load and SF=32 are used.

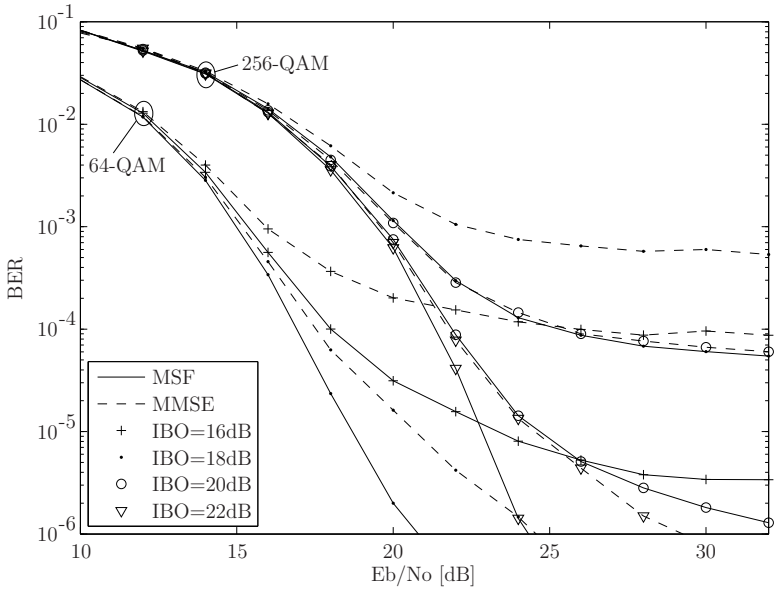

Figure 9.12: BER performance of a nonlinearly distorted MC-CDMA system using MSF-MUD and MMSE-MUD. 31.25% user load and SF=32 are used.

IBOs of 20dB(24dB) are required to achieve BER performances close to linear AWGN ones, while 16dB(20dB) of IBO is enough if MSF-MUD is used. Thus, a reduction of 4dB in the amplifier IBO requirements is achieved. On the other hand, by focusing on the signal-to-noise ratio requirements to achieve a target BER of 10^{-6} one can notice that for 64-QAM mapping and IBO=16dB, the required Eb/No for MSF-MUD is around 6dB to 7dB lower than that required for MMSE-MUD. Let us now consider the half-loaded system in Figure 9.10. As it was discussed in Section 9.4, here some performance improvement is still reached although it is not as important as for 12.5% and 31.25% user loads.

Figure 9.11 and Figure 9.12 show the BER characteristics of a nonlinearly distorted MC-CDMA system using length-32 Hadamard spreading codes with 12.5% and 31.25% user loads, respectively. The BER performance for 50% user load is not shown since it is very similar to that in Figure 9.10, where a spreading factor of 16 is used. As it can be observed from Figure 9.11 and Figure 9.12, when a spreading factor of 32 and low to moderate user loads are used a high performance improvement with respect to MMSE-MUD is still obtained.

From the presented simulation results we conclude that MSF-MUD provides a great performance improvement compared to MMSE-MUD in low user loads scenarios with short spreading factors.

Part III

Concluding remarks

Chapter 10

Conclusions

In this thesis an analysis of the effect of nonlinearities in MC and MC-SS systems was presented. Moreover, based on the presented analysis, efficient ways to reduce the sensitivity of such systems to nonlinear amplification were proposed.

The presented theoretical analysis was based on the widely known Bussgang theorem but extended to sub-Gaussian distributed signals. If the signal is Gaussian distributed then, from the Bussgang theorem, the effect of a nonlinearity reduces to a constant rotation and attenuation of the constellation plus the addition of an uncorrelated distortion noise. In practice, since the attenuation and rotation of the constellation is constant, it will be automatically compensated by the receiver through the channel equalization block. Therefore, only the distortion term is responsible for the performance degradation. Another implication from the Bussgang theorem is that the power of the distortion term introduced to each OFDM symbol is constant. Therefore, all OFDM symbols make an equal contribution to the out-of-band radiation. Moreover, since in most cases the distortion term can be seen as an AWGN, it results that the nonlinearity basically reduces the SNR.

For sub-Gaussian distributed signals the Bussgang theorem does not hold, moreover, the transmitted signal can not be modeled as a stationary and ergodic process. Nevertheless, one can still assume that the OFDM symbol at the output of the nonlinearity is equal to an attenuated and rotated version of the input symbol plus a distortion term. In such cases neither the attenuation/rotation nor the power of the distortion term are constant among different OFDM symbols. However, the average distortion term is still constant regardless of the system configuration. This implies that the error probability of sub-Gaussian distributed signals is further increased compared to that of Gaussian distributed ones. Another consequence is that the average interference introduced to neighboring communication systems is the same regardless of the system configuration. However, some OFDM symbols generate interference levels significantly larger than the average.

The analysis of the effect of nonlinearities in OFDM-based multicarrier systems has

a direct implication on the performance of practical wireless communication systems. When the number of subcarriers in the system is large (e.g. in broadcasting applications such as DVB or in the downlink of mobile systems) the signal can be assumed to be Gaussian distributed and, therefore, the previous discussion based on the Bussgang theorem holds. On the other hand, when the number of subcarriers is low (e.g. in the uplink of OFDMA-based wireless systems) the Gaussianity assumption, ergodicity and stationarity do not hold. Therefore one has to consider the extension of the Bussgang theorem presented in this thesis. A direct consequence from the presented analysis is that a worse performance is obtained for OFDM systems with low number of subcarriers when a nonlinear amplifier is present. This is of special relevance for low-cost power amplifiers in mobile handsets where linearity characteristics may be far from ideal.

In this thesis, the suitability of the signal metrics was also discussed and it was shown that CM is more related to the amount of distortion introduced by a nonlinearity than PAPR. Therefore, we believe that in order to increase the robustness of multicarrier systems to nonlinear distortion CM-reduction, instead of PAPR-reduction, should be considered. The performance improvement capabilities of several well-known PAPR-reducing techniques were also investigated. As it was observed, the spectral outgrowth is reduced but a BER performance improvement does not always occur.

Apart from presenting an analysis of the effect of nonlinearities in multicarrier systems, several strategies to increase the robustness of those systems to nonlinear amplification were also considered. One strategy is to reduce the envelope fluctuations of the transmitted signal. Here, even though it was previously shown that CM is a more suitable metric compared to PAPR, both PAPR and CM reduction are considered. Two major type of PAPR/CM-reducing techniques are addressed in this thesis: TR and CSO. Nevertheless, the clues to reformulate most of the PAPR-reducing techniques to CM-reduction are also given.

TR was first proposed for PAPR-reduction. In fact, several methodologies to implement TR have been proposed in the past few years. In this thesis, a new low complexity technique that achieves higher PAPR-reduction with lower computational complexity than the other methods in the literature is first proposed. Next, the TR technique is reformulated to CM-reduction and an optimal and a low-complexity suboptimal solution are presented. Moreover, since both suboptimal implementations for PAPR and CM are similar, a comparison of the performance improvement capabilities of both methods was also presented. Simulation results showed that larger performance improvement with lower power in the correcting tones is obtained by using CM.

A new technique to reduce the envelope fluctuations that was termed as controlled spectral outgrowth (CSO) was also proposed. The key idea of CSO is to take advantage of the RF specifications defined in standardization to reduce PAPR/CM of the transmitted signal. The advantage of this technique is that it is transparent to the receiver, the spectral efficiency is maintained and the power efficiency is scarcely reduced. In

fact, almost none of the other techniques in the literature fulfills such requirements. CSO is specially interesting in the Antarctic project to which this PhD thesis is related, since the power efficiency is scarcely reduced and no spectrum emission mask must be fulfilled.

Apart from proposing transmitter side techniques to reduce the envelope fluctuations, a receiver side technique to reduce the multiple access interference introduced by the nonlinearity in MC-SS systems was also considered. Let us recall that one of the consequences of nonlinear amplification in MC-SS systems is that the properties of the spreading codes are destroyed. This thesis considered a multiuser detector that is based on microstatistic filtering capable of providing a better or at least the same performance than conventional multiuser detectors. Another advantage of the proposed solution, in oppose to other receiver side solutions for nonlinearly distorted MC-SS systems, is that the computational complexity is slightly increased compared to that of conventional receivers.

Finally this thesis concludes with the presentation of part of the work that was undertaken at Ericsson AB regarding the analysis of the effect of nonlinearities in the uplink of LTE systems.

Chapter 11

Future work

One of the major contributions of this thesis was to provide an analysis of the effect of nonlinearities in multicarrier systems. For MC-SS systems, we did a small study where we discussed the major considerations that should be taken into account, but no detailed analysis was provided. From the experience obtained in this thesis we believe that a deep study of MC-SS systems should be done prior to considering the proposal of new techniques. This would most likely give us the clues for defining techniques that are really efficient when reducing the sensitivity of MC-SS systems to nonlinear amplification.

Despite the fact that a deep analysis for MC-SS systems has not yet been addressed, we believe that a good strategy is to exploit the code domain to define further techniques to counteract the effect of nonlinearities. A possible solution in that sense is to exploit unused spreading codes, or alternatively reserve some spreading codes, for reducing the envelope fluctuations of the transmitted signal. This solution has been formulated for CM-reduction and preliminary results suggest that a significant reduction of the cubic metric can be obtained.

Another important problem is to find specific solutions for the future generation of wireless communication systems. In Appendix A, the reader can find an analysis of the effect of nonlinearities in LTE uplink. Even though no specific solutions are discussed, the presented work gave us the clues to define some strategies to counteract the effect of nonlinearities in LTE uplink. Those are currently being evaluated.

During the past few years, using multiple antennas in the transmitter and/or the receiver has become more popular since it can further improve the performance of wireless systems. However, using multiple antennas in the transmitter means that it will also be equipped with multiple power amplifiers. Even though one could, in principle, use the strategies that were originally designed for single antenna systems individually to each of the power amplifiers in the transmitter, we believe that it is better to investigate on strategies that provide a unified solution for the multiple antenna transmitter. Moreover, it should be taken into account that since there are

different strategies to exploit the multiple antennas in the transmitter/receiver it is most likely that different solutions to counteract the effect of nonlinearities should be provided.

Part IV

Appendices

Appendix A

Analysis of LTE uplink

In this appendix we present a study of the signal metrics and nonlinearity effects in the single carrier frequency division multiple access (SC-FDMA) transmission scheme adopted in the LTE uplink. The presented study combines analytical formulation and numerical computation and covers all the different configurations of the current release of LTE. SC-FDMA modulation is known to have small variations in the instantaneous power and provides therefore low sensitivity to nonlinear power amplifiers.

In this appendix we discuss strategies to improve the robustness of the LTE uplink towards nonlinear distortion even further. As it will be shown the effect of the nonlinearity in SC-FDMA is independent of the pre-coder size. Nevertheless, distortion decreases towards smaller constellation sizes. This is of advantage since at the cell edge, where more power is required, the user terminal is generally required to employ low constellation sizes. We will also show that when the size of the pre-coder is small the error probability can be significantly reduced by employing advanced receiver techniques.

This work has been undertaken at Ericsson Research and it is published in this thesis with the authorization of Ericsson AB.

A.1 Introduction

The *Third Generation Partnership Project* (3GPP) is the standard-developing body that specifies the third generation of mobile communication systems and evolutions thereof. In Release 8 an evolved universal terrestrial radio access network termed as Long Term Evolution (LTE) was considered. 3GPP-LTE is intended to be a mobile communication system that can take the telecommunication industry into the 2020s [28]. In LTE no backward compatibility with WCDMA and HSPA is required and therefore, it exploits new technologies that were not previously considered in mobile systems.

The requirements for LTE regarding throughput, mobility, coverage, etc. are very strict. Therefore, among other challenges it is crucial to minimize the impact of non-

linear amplification on the performance of the system. Reducing the sensitivity to nonlinear amplification is of special relevance for mobile terminals. In LTE, the radio access for the uplink is based on single carrier frequency division multiple access (SC-FDMA). The reason is that not only it features small variations in the instantaneous power of the transmitted signal but also the possibilities for both FDMA with flexible bandwidth assignment and low-complexity high-quality equalization in the frequency domain [28]. For the base station using low cost and low power consuming amplifiers, although far from irrelevant, is not such an important design key. In turn, other requirements such as high robustness to frequency-selective fading and flexible scheduling in time and frequency domain are more important. Therefore, orthogonal frequency division multiple access (OFDMA) is used in the LTE downlink.

The analysis of nonlinearities effects in OFDM has widely been addressed in the literature [29]. Moreover many transmitter and receiver strategies to improve performance have been proposed. However, for SC-FDMA there are still a lot of open issues. In this appendix we study the signal metrics and the effect of nonlinear power amplifiers (PA) in the performance of LTE uplink [32]. Moreover, from the presented analysis we discuss the strategies to be considered to increase robustness of LTE uplink towards nonlinearity effects. The remainder of this appendix is organized as follows. First, in Section A.2 the basis of SC-FDMA and a brief study of the time domain signal is presented. Next, in Section A.3 we analyze the cubic metric (CM) and peak-to-average power ratio (PAPR) characteristics of the SC-FDMA transmission scheme. In Section A.4, we evaluate the effect of nonlinearities in the error probability and spectrum of the transmitted signal. Finally, in Section A.5, we draw some conclusions from the presented work.

A.2 The SC-FDMA signal

In SC-FDMA, a block of N data symbols from some modulation alphabet, such as QPSK or 16-QAM, is first applied to a size-N discrete Fourier transform (DFT). The output of the DFT is then applied to consecutive inputs of a size-M inverse DFT (IDFT), where $M \geq N$, and the unused inputs of the IDFT are set to zero. Note that the SC-FDMA signal is generated by first pre-coding the data symbols by means of the DFT operation and, then applying it to consecutive subcarriers of an OFDM system. Since the DFT pre-coding can alternatively be seen as spreading in the frequency domain, the SC-FDMA transmission scheme is also known as DFT-spread OFDM (DFTS-OFDM).

Let d_i, $i = 0, \ldots, N-1$ be the complex data symbols, then the signal at the output of the pre-coder can be expressed as

$$S_k = \frac{1}{\sqrt{N}} \sum_{i=0}^{N-1} d_i e^{-j2\pi i(k-N/2)/N}, \qquad k = 0, \ldots, N-1. \tag{A-1}$$

In the OFDM block the N pre-coded data symbols are transmitted over N consecutive subcarriers. Consider a baseband OFDM symbol $s(t)$ defined over the time interval $t \in [0, T_s)$,

$$s(t) = \frac{1}{\sqrt{N}} \sum_{k=0}^{N-1} S_k e^{j2\pi(k+k_0)t/T_s}, \tag{A-2}$$

where k_0 is the position of the first subcarrier. For the sake of simplicity in the mathematical formulation, in the remainder of this section $k_0 = 0$ is assumed. The generalization to $k_0 \neq 0$ will be considered in Section A.3. If the signal in (A-2) is sampled at a frequency LN/T_s, where $L = M/N$ is the oversampling factor and N/T_s is the Nyquist rate, the complex samples can be described as

$$s_n = \frac{1}{\sqrt{N}} \sum_{k=0}^{N-1} S_k e^{j2\pi kn/M}, \qquad n = 0, \ldots, M-1. \tag{A-3}$$

The expression above can be computed by means of a length-M scaled IDFT. Therefore, from (A-1) and (A-3) the DFTS-OFDM signal can be expressed as

$$\begin{aligned} s_n &= \frac{1}{\sqrt{N}} \sum_{k=0}^{N-1} \left(\frac{1}{\sqrt{N}} \sum_{i=0}^{N-1} d_i e^{-j2\pi ik/N} \cdot e^{j\pi i} \right) e^{j2\pi kn/M} \\ &= \frac{1}{N} \sum_{i=0}^{N-1} (-1)^i d_i \sum_{k=0}^{N-1} e^{j2\pi k(n-Li)/M} \\ &= \frac{1}{N} \sum_{i=0}^{N-1} d'_i \sum_{k=0}^{N-1} e^{j2\pi k(n-Li)/M}. \end{aligned} \tag{A-4}$$

Note that for the mapping schemes used in LTE uplink $(-1)^i d_i$ is always a point of the constellation, therefore we denote it as d'_i.

Let us analyze the SC-FDMA signal at sample positions multiple of the spreading factor. If $n = Lr$, the time domain signal in (A-4) reduces to

$$\begin{aligned} s_{Lr} &= \frac{1}{N} \sum_{i=0}^{N-1} d'_i \sum_{k=0}^{N-1} e^{j2\pi k(r-i)/N} \\ &= \frac{1}{N} \left(d'_r \underbrace{\sum_{k=0}^{N-1} e^{j2\pi k0/N}}_{N} + \sum_{\substack{i=0 \\ i \neq r}}^{N-1} d'_i \underbrace{\sum_{k=0}^{N-1} e^{j2\pi k(r-i)/N}}_{0} \right) \\ &= d'_r, \end{aligned} \tag{A-5}$$

which means that the Lr-th sample of the time-domain SC-FDMA signal is equal to the data symbol $\pm d_r$. If r is even then the time-domain signal at the Lr-th sample will

be equal to d_r, otherwise it will take the value $-d_r$. The samples at positions $n \neq Lr$ describe the transition of the time-domain signal between the values d'_r and d'_{r+1}. The above formulation was done assuming that the spreading factor is an integer value. If $L \notin \mathbb{Z}$ then the SC-FDMA signal will take values equal to d'_k at time instants different than the sampling instants and, therefore, it will only occur in the analog signal.

As an example, Figure A.1 shows the instantaneous power of an oversampled SC-FDMA signal with $N = 64$ and QPSK mapping. The envelope at multiples of T_s/N is marked with dots. Since QPSK mapping is used the envelope at these normalized time instants is always equal to 1. However, between those samples the signal fluctuates. This is similar to the effect observed when a rectangular pulse is low-pass filtered.

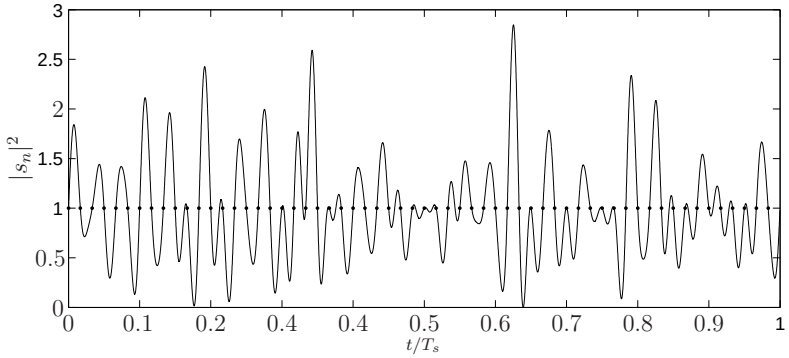

Figure A.1: Envelope of an oversampled signal with $N = 64$ and QPSK mapping.

A.3 Analysis of the signal metrics

In this section we analyze the CM and PAPR characteristics of the SC-FDMA transmission scheme. In LTE uplink each user terminal can employ a wide range of system configurations, including different modulation schemes and frequency resources. In order to provide a broad study of the envelope fluctuations of the SC-FDMA signal we analyze the effect of the different configurations in the signal metrics.

A.3.1 Definition of the signal metrics

Two signal metrics are used in the literature: PAPR and CM. The PAPR of a symbol $s(t)$ is defined as the ratio between its peak power and average power of the transmitted signal,

$$\mathrm{PAPR}\left(s(t)\right) = \frac{\|s(t)\|^2_\infty}{\sigma^2}. \tag{A-6}$$

To evaluate the PAPR characteristics it is customary to compute the complementary cumulative density function (CCDF). CM is defined by 3GPP as [2]

$$\mathrm{CM}|_{\mathrm{dB}} = (\mathrm{RCM}|_{\mathrm{dB}} - \mathrm{RCM}_{\mathrm{ref}}|_{\mathrm{dB}})/K, \tag{A-7}$$

where RCM is called the raw CM, which for a signal $x(t)$, is defined as

$$\mathrm{RCM}\left(x(t)\right)\Big|_{\mathrm{dB}} = 20\log\left[\mathrm{rms}\left[\left(\frac{|x(t)|}{\mathrm{rms}[x(t)]}\right)^3\right]\right]. \tag{A-8}$$

$\mathrm{RCM}_{\mathrm{ref}}|_{\mathrm{dB}}$ is the RCM of the reference signal and K is an empirical slope factor that is used to complete the estimate of the PA power de-rating. In LTE $\mathrm{RCM}_{\mathrm{ref}}$=1.52dB and K=1.56 is used, furthermore an offset of 0.77dB can be used depending on the nominal bandwidth [2]. CM is often computed over a large signal period corresponding to a large number of SC-FDMA symbols such that a single value for each SC-FDMA system is obtained [28]. Since CM and RCM are linearly related, in order to provide a more general study, in this appendix we will provide values for RCM.

A.3.2 Oversampling

Let us first consider the effect of oversampling in the SC-FDMA signal. In Figure A.1 we observed that the envelope of an oversampled SC-FDMA signal differs from that of a non-oversampled, thus, affecting the PAPR and CM properties of the SC-FDMA signal. We should take into account that, in practice, the signal that undergoes non-linear distortion is in the analog domain. Therefore, in order to better approximate PAPR and CM of the analog signal, they must be computed by using oversampling. Extensive simulations of the probabilistic distribution of the PAPR and CM of each SC-FDMA symbol using different configurations and oversampling factors were done. It was observed that, as we expected there is a difference between oversampled and non-oversampled signals. However, an oversampling factor $L = 2$ is enough to compute the analog signal metrics with sufficient accuracy.

Note that from the above discussion it follows that, as long as $L > 2$, PAPR and CM of an SC-FDMA signal employing a pre-coder of size N is the same regardless of the size of the IFFT.

A.3.3 Frequency resources

The next issue we investigate is the effect of the frequency resources allocation. Two aspects must be considered, the frequency position and the occupied bandwidth.

Let us start by considering the frequency position. The expression of the SC-FDMA signal in (A-4) was derived assuming that the subcarriers were allocated at consecutive positions starting from 0. In general, the first subcarrier is placed at a position $k_0 \neq 0$. In shuch case, the expression of the SC-FDMA signal is found

to be $s_n(k_0) = s_n\ e^{j2\pi k_0/M}$, for $n = 0, \ldots, M-1$. It can be easily shown that $\text{PAPR}\left(\mathbf{s}^{(i)}(k_0)\right) = \text{PAPR}\left(\mathbf{s}^{(i)}\right)$ and that $\text{CM}\left(\mathbf{s}^{(i)}(k_0)\right) = \text{CM}\left(\mathbf{s}^{(i)}\right)$. As a result, we can affirm that in LTE uplink the PAPR and CM characteristics of two users using the same number of resource blocks and modulation scheme but transmitting at different frequency positions, will be the same.

Let us now consider the effect of the occupied bandwidth, i.e. number of allocated subcarriers. In opposite to the previous cases providing an analytical formulation is not straightforward and therefore, conclusions will be drawn from numerical simulations. Extensive simulations with different configurations were done, however, since the same behavior was observed, for the sake of clarity only some simulation results are shown. Figure A.2.a shows the distribution of PAPR of SC-FDMA signals using 64-QAM mapping and different occupied bandwidths. The raw CM is shown in Table A.1. As it can be observed PAPR increases with the number of active subcarriers while RCM remains approximately constant.

A.3.4 Baseband modulation

The last issue we investigate is the effect of the modulation scheme. Let us first consider that no oversampling is done, $L = 1$. In this case, it follows from (A-5) that the time-domain SC-FDMA signal is constituted by the data symbols transmitted consecutively. Let I_q, $q = 1, 2, \ldots, Q$ be the different symbols of a Q-ary QAM constellation. Then, assuming that a large number of subcarriers is used so that all data symbols appear with equal probability in each SC-FDMA symbol, the average PAPR and RCM of the SC-FDMA signal is

$$\text{PAPR} = 3 \cdot \frac{\sqrt{Q}-1}{\sqrt{Q}+1}, \tag{A-9}$$

$$\text{RCM} = \sqrt{\frac{1}{Q \cdot \sigma^3} \sum_{q=1}^{Q} |I_q|^6}. \tag{A-10}$$

For {QPSK, 16-QAM, 64-QAM} we obtain PAPR={0, 2.5, 3.7}dB and RCM={0, 2.9, 3.5}dB . As it can be observed, the PAPR and CM characteristics of the SC-FDMA signal are strongly related to the mapping scheme being used. Larger constellation sizes result in larger average PAPR and CM. This can be verified in the simulation results presented in Figure A.2.b and Table A.1. As we expected the signal metrics always increase with the modulation size, regardless of the occupied bandwidth.

A.4 Performance in nonlinear AWGN channels

In this section we evaluate the performance of SC-FDMA systems when a nonlinearity is present. Moreover, we consider the information provided by the signal metrics and

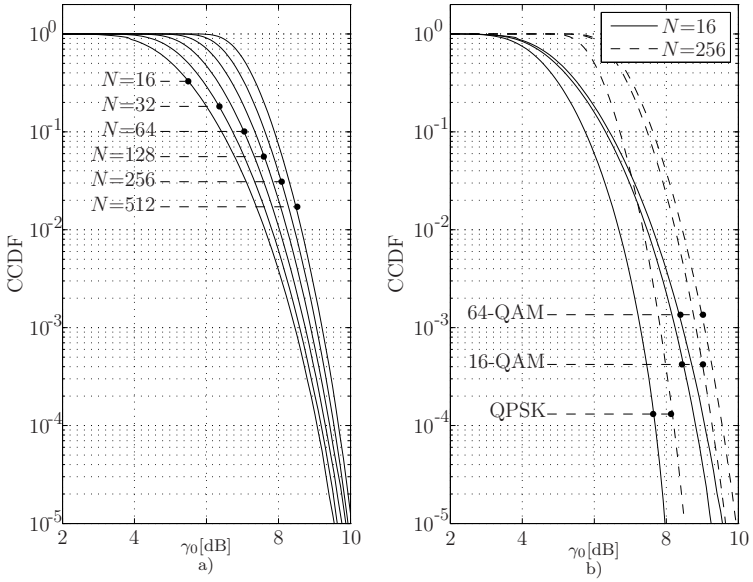

Figure A.2: Analog PAPR of an SC-FDMA system for a) different occupied bandwidths with 64-QAM mapping and b) different modulation schemes.

RCM [dB]	N=16	N=32	N=64	N=128	N=256	N=512
QPSK	4.0	3.7	3.6	3.5	3.5	3.5
16-QAM	5.4	5.2	5.0	4.9	4.9	4.9
64-QAM	5.7	5.5	5.3	5.2	5.2	5.2

Table A.1: Analog RCM for different occupied bandwidths and modulation schemes.

discuss their capabilities to predict the nonlinearity effects. In the simulations two type of nonlinearities are used, namely Saleh and soft limiter [57]. The Saleh model is defined by the following amplitude-to-amplitude modulation (AM/AM) and amplitude-to-phase modulation (AM/PM) characteristics,

$$\mathrm{G}(u) = \frac{\kappa_G \cdot u}{1 + \chi_G \cdot u^2}, \qquad \Phi(u) = \frac{\kappa_\Phi \cdot u^2}{1 + \chi_\Phi u^2}. \tag{A-11}$$

In the expressions above we chose $\kappa_G = 2$, $\chi_G = \chi_\Phi = 1$ and $\kappa_\Phi = \pi/3$. The soft limiter is defined as

$$\mathrm{G}(u) = \begin{cases} u \text{ if } u \leq 1 \\ 1 \text{ otherwise} \end{cases}, \qquad \Phi(u) = 0. \tag{A-12}$$

The Saleh model is used to evaluate the performance in highly nonlinear amplifiers that not only introduce amplitude but also phase distortion. The soft limiter is used to model the case when pre-distortion is done at the transmitter. The operating point of the nonlinearity is defined by the so called input back-off (IBO) which corresponds to the ratio between the saturated and average input powers.

A.4.1 Out-of-band emission

In Section A.3 we analyzed the signal metrics in SC-FDMA. It was shown that both CM and PAPR decrease towards smaller constellation sizes, therefore we expect that nonlinear distortion also decreases with the constellation size. Figure A.3 shows the power spectral density (PSD) of an SC-FDMA signal at the output of a soft limiter operating at IBO=4dB. As we expected, the out-of-band emission increases with Q. The out-of-band emission is generated by the distortion term introduced by the nonlinearity, therefore lower spectral spreading means also lower in-band distortion and, as a result, higher modulation quality.

In standardization the modulation quality is typically specified by means of the so-called error vector magnitude (EVM) in such a way that the EVM requirements increase with the constellation size. Note that this means that if the user employs QPSK it will be able to use larger transmission power (thus lower IBO) than if it employed 64-QAM. We should take into account that when the user terminal is far from the base station or the link quality is poor, it will usually be asked to employ low constellation sizes and large transmission powers. Therefore, the fact that the user terminal can use a higher transmission power when employing low constellation sizes is positive, since it allows large transmission power in such stringent conditions. Following the previous discussion, the property that in SC-FDMA lower modulation sizes imply higher modulation quality is of advantage for cellular communication systems. Note that this means that the user terminal will be allowed to use even larger transmission power when it is far from the base station or the link quality is poor.

Another important aspect to be considered is the effect of the pre-coder size. As it was observed in Figure A.2 and Table A.1, PAPR increases with N while CM remains approximately constant. We should take into account that one of the purposes of quantifying the envelope fluctuations is to determine the PA power de-rating. Therefore, one would expect that both metrics have the same behavior. In [2] and [1], after analyzing certain OFDM-type signals that are considered to meet the LTE goals, it was shown that CM predicts PA power de-rating more accurately than PAPR. The spectrum shown in Figure A.3 was obtained regardless of the pre-coder size. This means that the distortion term introduced by a nonlinear amplifier is independent of N. Therefore, as it was already discussed in 3GPP, CM seems to be a more suitable metric to determine the required PA power de-rating.

A.4.2 Detection issues

In this section we evaluate the effect of nonlinearities in the bit error rate (BER) performance. Let us model the SC-FDMA system as a stochastic process $\mathcal{S}$ such that each symbol $s^{(i)}(t)$, $t \in [0, T_s)$, is a different realization of $\mathcal{S}$. Let us define $s_d^{(i)}(t)$ as the output signal of a nonlinear amplifier with input signal $s^{(i)}(t)$. Conventional receivers only process the part of $s_d^{(i)}(t)$ that corresponds to a linear amplification of $s^{(i)}(t)$, while

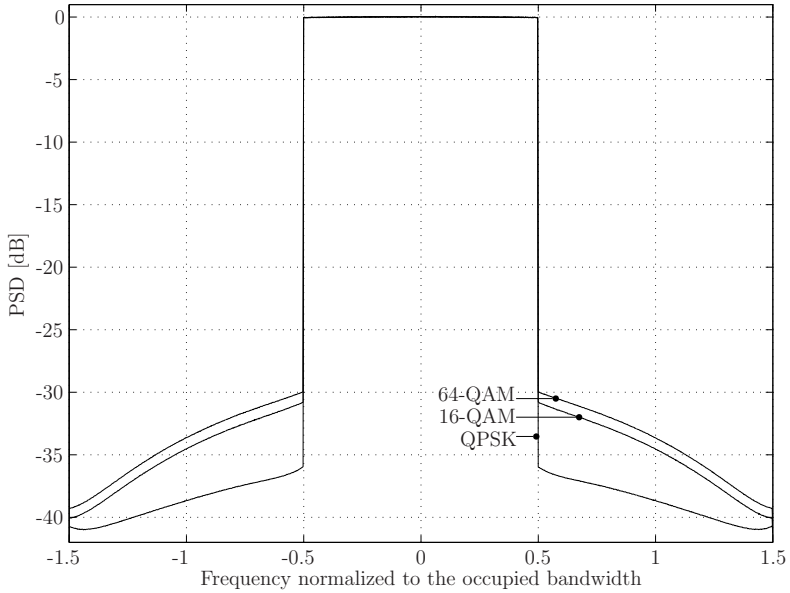

Figure A.3: PSD of an SC-FDMA/OFDM system when a soft limiter operating at IBO=4dB is present.

the remainder of the signal is seen as distortion. Therefore, we can express the output signal as

$$s_d^{(i)}(t) = \alpha^{(i)} s^{(i)}(t) + d^{(i)}(t), \tag{A-13}$$

where $d^{(i)}(t)$ is the distortion term and $\alpha^{(i)}$ is a complex amplification term that depends on the outcome i of $\mathcal{S}$. The value of $\alpha^{(i)}$ that minimizes the mean-squared error (MSE) of the unbiased input and output signals is found to be [79]

$$\alpha^{(i)} = \frac{\langle s_d(t), s(t)\rangle_i - \langle s_d(t)\rangle_i \langle s(t)\rangle_i^*}{\langle |s(t)|^2\rangle_i - \langle s(t)\rangle_i \langle s(t)\rangle_i^*}, \tag{A-14}$$

where $\langle x(t), y(t)\rangle_i = \frac{1}{T_s}\int_0^{T_s} x^{(i)}(t)(y^{(i)}(t))^* dt$ is the inner product of $x^{(i)}(t)$ and $y^{(i)}(t)$, and $\langle x(t)\rangle_i = \frac{1}{T_s}\int_0^{T_s} x^{(i)}(t) dt$ is the time average of $x^{(i)}(t)$.

In LTE uplink SC-FDMA is used. In such case, the process $\mathcal{S}$ is nonstationary regardless of N. To see it, let us consider as an example an SC-FDMA system employing QPSK. A realization of such process was depicted in Figure A.1. It can be observed that the envelope at multiples of T_s/N is always constant while it takes different values in-between. In fact, this will occur for all realizations since, as we previously showed, the signal at multiple of T_s/N takes always values equal to $\pm d_r$ while it might take a larger set of values between these time instants. Therefore, the autocorrelation function of $s(t)$ at t_1 and t_2 will be a function of both t_1 and the time difference $\tau = t_2 - t_1$, $R_{ss}(t, \tau)$. Since the process is nonstationary, the term $\alpha^{(i)}$ will in fact be a function of time, $\alpha^{(i)}(t)$. As a result, the constellation within an SC-FDMA symbol will not be constantly attenuated and rotated, instead warping will occur.

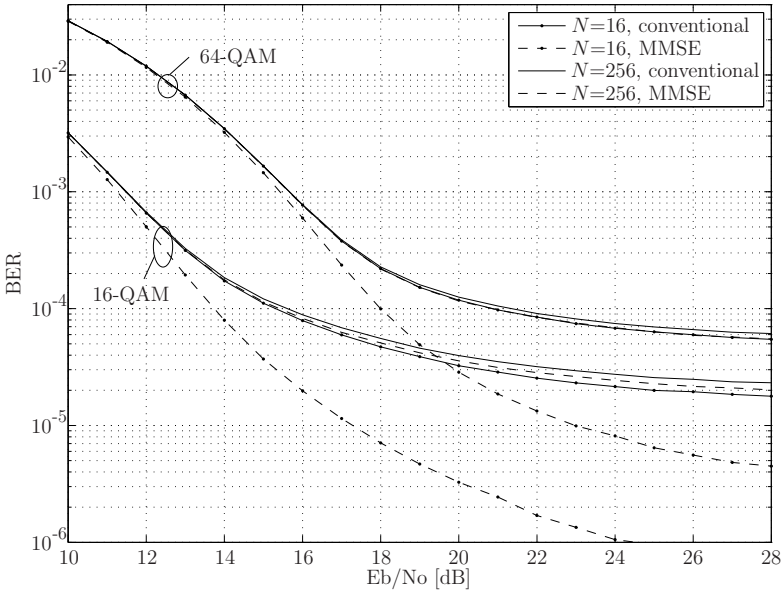

Figure A.4: BER performance of an SC-FDMA system when a Saleh nonlinearity operating at IBO={11,15}dB for {16,64}-QAM is present.

Furthermore, if low values of N are used, $\mathcal{S}$ will not be ergodic and the time average of each realization might be different than zero. Therefore, the complex amplification term $\alpha^{(i)}$ will be different for different SC-FDMA symbols. Conventional receivers typically neglect the realization-varying complex amplification term, instead it is assumed to be constant. Therefore, compensating for this realization-varying complex amplification term enables us to improve performance. We should take into account that since the term $\alpha^{(i)}$ is in fact a function of time, the more data symbols are transmitted in an SC-FDMA symbol, the more the term $\alpha^{(i)}$ for each realization will approach to the average value. Therefore, for small N larger improvements are expected than for large N.

As an example Figure A.4 shows the error probability of an SC-FDMA system employing N={16, 256} and {16, 64}-QAM. A Saleh nonlinearity operating at IBO={11, 15}dB for {16, 64}-QAM is present. For each setup, the BER achieved by a conventional receiver and an advanced receiver is shown. The advanced receiver, denoted as minimum MSE (MMSE) compensates each SC-FDMA symbol individually. It can be observed that, as we expected, the improvement in BER is larger for small N than for large N. Numerical simulation employing a soft limiter were also done and also here a larger improvement of the BER performance was observed for low values of N.

We previously discussed that in SC-FDMA, $\mathcal{S}$ is nonstationary and therefore constellation warping occurs. In the simulation results shown in Figure A.4 we only compensated the realization-varying complex amplification term but not the constellation warping. Therefore, if further processing is done at the receiver to compensate the

constellation warping the error rate probabilities will be even more reduced.

A.5 Conclusions

In this appendix we presented a study of the signal metrics and nonlinearity effects in LTE uplink. It was shown that CM is independent of N but increases with the constellation size. In fact, since the distortion term that causes the spectral spreading follows the same behavior we conclude that —as it was already discussed in 3GPP— CM is a more suitable metric to predict the effect of nonlinearities. In this appendix we also evaluated the BER performance. We observed that for conventional receivers BER is independent of the pre-coder size. However, for low N it can be significantly improved by compensating the realization-varying complex amplification term.

Appendix B

Lower bound of the error probability of nonlinearly distorted OFDM signals

In this appendix the lower bound of the error probability of nonlinearly distorted OFDM signals is derived. It is shown that for a conventional linear receiver, sub-Gaussian distributed OFDM signals undergoing nonlinear AWGN channels have larger error probabilities than Gaussian distributed ones. In practice, this means that the error rate of an OFDM system with low number of subcarriers is higher than that of an OFDM system with large number of subcarriers.

Let γ be the signal to noise-plus-disotion ratio (SNDR) at the input of the receiver. Assuming that the distortion term is Gaussian, for a given signal power σ^2 and AWGN power σ_W^2 the relation between γ and σ_D^2 is

$$\gamma = g(\sigma_D^2) = \frac{\sigma^2}{\sigma_W^2 + \sigma_D^2}. \tag{B-1}$$

Let $f_D(\sigma_D^2)$ be the PDF of the nonlinear distortion term. Since $g(\sigma_D^2)$ is monotonic and the inverse function $\sigma_D^2 = g^{-1}(\gamma)$ exists the PDF of the SNDR is found to be [79]

$$f_\Gamma(\gamma) = f_D\left(\frac{\sigma^2}{\gamma} - \sigma_W^2\right)\frac{\sigma^2}{\gamma^2}. \tag{B-2}$$

From (B-1) and (B-2) the probability of error of sub-Gaussian distributed OFDM signals in (6.20) can be rewritten as

$$P_e = \int_0^{\sigma^2/\sigma_W^2} P_e^{(G)}(\gamma)\, f_\Gamma(\gamma)\; d\gamma, \tag{B-3}$$

where $P_e^{(G)}\left(\frac{\sigma^2}{\sigma_W^2+\sigma_D^2}\right)$ is the probability of error assuming a received signal power of σ^2 and a Gaussian noise of power $\sigma_W^2 + \sigma_D^2$. Note that (B-3) is, in fact, the expected value

of $P_e^{(G)}(\gamma)$, $P_e = E\left[P_e^{(G)}(\gamma)\right]$. According to [74] for PSK and QAM constellations $P_e^{(G)}(\gamma)$ is a convex function of γ. Therefore, since γ is in the domain of $P_e^{(G)}(\cdot)$, from the Jensen's inequality it follows that [19]

$$P_e = E\left[P_e^{(G)}(\gamma)\right] \geq P_e^{(G)}(E[\gamma]). \tag{B-4}$$

The equality only holds for large N where σ_D^2 is constant for all OFDM symbols. However, since $E[\gamma]$ is independent of the number of subcarriers, it follows that $P_e^{(G)}(E[\gamma])$ is also independent of N. As a result, $P_e^{(G)}(E[\gamma])$ in (B-4) is in fact equal to the analytical error probability of a Gaussian distributed OFDM signal undergoing a nonlinear amplifier [29].

Appendix C

Raw CM of a complex Gaussian distributed random variable

In Chapter 6 we stated that, assuming the OFDM signal is complex Gaussian distributed, its raw CM is $\sqrt{6}$. In this appendix, the mathematical formulation required to show it is provided.

Let the real and imaginary parts of a complex random variable be Gaussian distributed with zero mean and variance $\sigma^2/2$. Then its magnitude is known to be a Rayleigh distributed random variable X with a probability density function as defined in (4.1). Let us now define the following transformation $Y = g(X) = X^p$. The expected value of $g(X)$ is found to be [79]

$$\begin{aligned} E\left[X^p\right] &= \int_{-\infty}^{\infty} x^p f_X(x) dx \\ &= \frac{2}{\sigma^2} \int_0^{\infty} x^{(p+1)} e^{-\frac{x^2}{\sigma^2}} dx. \end{aligned} \tag{B-1}$$

Note that $f_X(x) = 0$ for $x < 0$. By defining $t = \frac{x^2}{\sigma^2}$, (B-1) can be rewritten as

$$\begin{aligned} E\left[X^p\right] &= \sigma^p \int_0^{\infty} e^{-t} t^{p/2} dt \\ &= \sigma^p \cdot \Gamma\left(1 + p/2\right), \end{aligned} \tag{B-2}$$

where $\Gamma(z) = \int_0^{\infty} e^{-t} t^{z-1}$ is the Gamma function. From (4.7) and (B-2) with $p = 6$ the raw CM of a complex Gaussian distributed random variable is found to be

$$\mathrm{RCM}\left(s(t)\right) = \frac{1}{\sigma^3} \sqrt{\sigma^6 \cdot \Gamma\left(4\right)} = \sqrt{6}. \tag{B-3}$$

Appendix D

Derivation of the mathematical formulation for CM-reduction by tone reservation

In Section 7.2, the tone reservation technique, originally derived for PAPR-reduction, was reformulated to reduce CM. Two methods were proposed to compute the complex amplitude of the correcting tones, namely, optimal and suboptimal. This appendix provides the solutions to the optimization problems in Section 7.2 to compute the CM-reducing signal.

D.1 Optimal CM-reduction

Let us first recall from Section 7.2 that the complex amplitude of the CM-reducing tones is found by solving the following unconstrained convex optimization problem

$$\arg \min_{\dot{\mathbf{C}} \in \mathbb{R}^{2R}} J(\dot{\mathbf{C}}) \tag{C-1}$$

where the objective function is defined as

$$J(\dot{\mathbf{C}}) = \sum_{n=0}^{LN-1} \left(\left(\bar{s}_n^{(r)}\right)^2 + \left(\bar{s}_n^{(i)}\right)^2 \right)^3, \tag{C-2}$$

with

$$\bar{s}_n^{(r)} = s_n^{(r)} + \sum_{k=1}^{R} \left(C_{q_k}^{(r)} w_{n,k}^{(r)} - C_{q_k}^{(i)} w_{n,k}^{(i)} \right), \tag{C-3}$$

$$\bar{s}_n^{(i)} = s_n^{(i)} + \sum_{k=1}^{R} \left(C_{q_k}^{(i)} w_{n,k}^{(r)} + C_{q_k}^{(r)} w_{n,k}^{(i)} \right). \tag{C-4}$$

Moreover, it was also shown that to compute the optimal solution one has to solve the following matrix equation

$$\nabla^2 J(\dot{\mathbf{C}})\ \Delta\dot{\mathbf{C}} = -\nabla J(\dot{\mathbf{C}}). \tag{C-5}$$

In the following, the required mathematical formulation is provided. Let us define ξ_n as the instantaneous power of the CM-reduced OFDM signal,

$$\xi_n = \left(\bar{s}_n^{(r)}\right)^2 + \left(\bar{s}_n^{(i)}\right)^2, \tag{C-6}$$

and

$$\gamma_{n,\,k}^{(r)} = \bar{s}_n^{(r)} w_{n,\,k}^{(r)} + \bar{s}_n^{(i)} w_{n,\,k}^{(i)}, \tag{C-7}$$
$$\gamma_{n,\,k}^{(i)} = \bar{s}_n^{(i)} w_{n,\,k}^{(r)} - \bar{s}_n^{(r)} w_{n,\,k}^{(i)}, \tag{C-8}$$
$$\tag{C-9}$$

and

$$\beta_{n,\,k,\,l}^{(r)} = w_{n,\,l}^{(r)} w_{n,\,k}^{(r)} + w_{n,\,l}^{(i)} w_{n,\,k}^{(i)}, \tag{C-10}$$
$$\beta_{n,\,k,\,l}^{(i)} = w_{n,\,l}^{(r)} w_{n,\,k}^{(i)} - w_{n,\,l}^{(i)} w_{n,\,k}^{(r)}, \tag{C-11}$$

as the real and imaginary parts of $\gamma_{n,\,k} = \bar{s}_n \cdot (w_{n,\,k})^*$ and $\beta_{n,\,k,\,l} = w_{n,\,k} \cdot (w_{n,\,l})^*$, respectively. Then, the gradient operator is found to be

$$\nabla J(\dot{\mathbf{C}}) = \left[\frac{\partial\, J(\dot{\mathbf{C}})}{\partial\, C_{q_1}^{(r)}}\ \frac{\partial\, J(\dot{\mathbf{C}})}{\partial\, C_{q_1}^{(i)}}\ \cdots\ \frac{\partial\, J(\dot{\mathbf{C}})}{\partial\, C_{q_R}^{(r)}}\ \frac{\partial\, J(\dot{\mathbf{C}})}{\partial\, C_{q_R}^{(i)}}\right]^{\mathrm{T}}, \tag{C-12}$$

where from (C-1), (C-3), (C-4) and the previous definitions

$$\frac{\partial\, J(\dot{\mathbf{C}})}{\partial\, C_{q_k}^{(r)}} = 6 \sum_{n=0}^{LN-1} \xi_n^2 \gamma_{n,k}^{(r)}, \tag{C-13}$$
$$\frac{\partial\, J(\dot{\mathbf{C}})}{\partial\, C_{q_k}^{(i)}} = 6 \sum_{n=0}^{LN-1} \xi_n^2 \gamma_{n,k}^{(i)}. \tag{C-14}$$

The Hessian is

$$\nabla^2 J(\dot{\mathbf{C}}) = \begin{bmatrix} \frac{\partial^2 J(\dot{\mathbf{C}})}{\partial C_{q_1}^{(r)} \partial C_{q_1}^{(r)}} & \frac{\partial^2 J(\dot{\mathbf{C}})}{\partial C_{q_1}^{(r)} \partial C_{q_1}^{(i)}} & \cdots & \frac{\partial^2 J(\dot{\mathbf{C}})}{\partial C_{q_1}^{(r)} \partial C_{q_R}^{(i)}} \\ \frac{\partial^2 J(\dot{\mathbf{C}})}{\partial C_{q_1}^{(i)} \partial C_{q_1}^{(r)}} & \frac{\partial^2 J(\dot{\mathbf{C}})}{\partial C_{q_1}^{(i)} \partial C_{q_1}^{(i)}} & \cdots & \frac{\partial^2 J(\dot{\mathbf{C}})}{\partial C_{q_1}^{(i)} \partial C_{q_R}^{(i)}} \\ \vdots & \vdots & \ddots & \vdots \\ \frac{\partial^2 J(\dot{\mathbf{C}})}{\partial C_{q_R}^{(r)} \partial C_{q_1}^{(r)}} & \frac{\partial^2 J(\dot{\mathbf{C}})}{\partial C_{q_R}^{(r)} \partial C_{q_1}^{(i)}} & \cdots & \frac{\partial^2 J(\dot{\mathbf{C}})}{\partial C_{q_R}^{(r)} \partial C_{q_R}^{(i)}} \\ \frac{\partial^2 J(\dot{\mathbf{C}})}{\partial C_{q_R}^{(i)} \partial C_{q_1}^{(r)}} & \frac{\partial^2 J(\dot{\mathbf{C}})}{\partial C_{q_R}^{(i)} \partial C_{q_1}^{(i)}} & \cdots & \frac{\partial^2 J(\dot{\mathbf{C}})}{\partial C_{q_R}^{(i)} \partial C_{q_R}^{(i)}} \end{bmatrix}, \tag{C-15}$$

with

$$\frac{\partial^2 J(\dot{\mathbf{C}})}{\partial C_{q_k}^{(r)} \partial C_{q_l}^{(r)}} = 6 \sum_{n=0}^{LN-1} \left[4\xi_n \gamma_{n,l}^{(r)} \gamma_{n,k}^{(r)} + \xi_n^2 \beta_{n,k,l}^{(r)} \right], \tag{C-16}$$

$$\frac{\partial^2 J(\dot{\mathbf{C}})}{\partial C_{q_k}^{(r)} \partial C_{q_l}^{(i)}} = 6 \sum_{n=0}^{LN-1} \left[4\xi_n \gamma_{n,l}^{(i)} \gamma_{n,k}^{(r)} + \xi_n^2 \beta_{n,k,l}^{(i)} \right], \tag{C-17}$$

$$\frac{\partial^2 J(\dot{\mathbf{C}})}{\partial C_{q_k}^{(i)} \partial C_{q_l}^{(r)}} = 6 \sum_{n=0}^{LN-1} \left[4\xi_n \gamma_{n,l}^{(r)} \gamma_{n,k}^{(i)} + \xi_n^2 \beta_{n,l,k}^{(i)} \right], \tag{C-18}$$

$$\frac{\partial^2 J(\dot{\mathbf{C}})}{\partial C_{q_k}^{(i)} \partial C_{q_l}^{(i)}} = 6 \sum_{n=0}^{LN-1} \left[4\xi_n \gamma_{n,l}^{(i)} \gamma_{n,k}^{(i)} + \xi_n^2 \beta_{n,l,k}^{(r)} \right]. \tag{C-19}$$

To reduce the complexity of computing $\nabla^2 J(\dot{\mathbf{C}})$ one can exploit the fact that $\beta_{n,k,l}^{(r)} = \beta_{n,l,k}^{(r)}$, $\beta_{n,k,l}^{(i)} = -\beta_{n,l,k}^{(i)}$ and that since all the second derivatives of the objective function are continuous in $\mathbb{R}^{2R}$, according to Schwarz's theorem (C-15) is symmetric. Moreover, the crossed-term elements in the 2 by 2 block diagonal, where $k = l$, reduce to

$$\frac{\partial^2 J(\dot{\mathbf{C}})}{\partial C_{q_k}^{(r)} \partial C_{q_k}^{(i)}} = \frac{\partial^2 J(\dot{\mathbf{C}})}{\partial C_{q_k}^{(i)} \partial C_{q_k}^{(r)}} = 6 \sum_{n=0}^{LN-1} 4\xi_n \gamma_{n,k}^{(i)} \gamma_{n,k}^{(r)}. \tag{C-20}$$

D.2 Proposed sub-optimal solution

First of all, note that computing the scaling factor μ in the suboptimal solution is equivalent to computing the complex amplitude of an OFDM signal with a single reserved tone. Thus, (7.37) can be formulated as an unconstrained convex optimization problem with a complexity of order $\mathcal{O}(N)$. Let the objective function $J(\mu)$ be as defined in (7.37) then, according to the Newton's method, the problem can be solved by means of an iterative algorithm that computes a sequence of points $\mu^{(0)}, \mu^{(1)}, \ldots, \mu^{(m)}, \ldots \in \mathbb{C}$ which tends to the minimal value as $m \to \infty$. In the iterative algorithm we start from a suitable point $\mu^{(0)} = 1$ and compute the next point as

$$\mu^{(m+1)} = \mu^{(m)} + \Delta\mu^{(m)}, \tag{C-21}$$

where m is the index of the iteration. The descent direction, $\Delta\mu$, is found by solving the Newton system

$$\begin{bmatrix} \frac{\partial^2 J(\mu)}{\partial \mu^{(r)} \partial \mu^{(r)}} & \frac{\partial^2 J(\mu)}{\partial \mu^{(r)} \partial \mu^{(i)}} \\ \frac{\partial^2 J(\mu)}{\partial \mu^{(i)} \partial \mu^{(r)}} & \frac{\partial^2 J(\mu)}{\partial \mu^{(i)} \partial \mu^{(i)}} \end{bmatrix} \begin{bmatrix} \Delta\mu^{(r)} \\ \Delta\mu^{(i)} \end{bmatrix} = - \begin{bmatrix} \frac{\partial J(\mu)}{\partial \mu^{(r)}} \\ \frac{\partial J(\mu)}{\partial \mu^{(i)}} \end{bmatrix}, \tag{C-22}$$

where the elements of the gradient are computed as

$$\frac{\partial\, J(\mu)}{\partial\, \mu^{(r)}} = 6 \sum_{n=0}^{LN-1} \xi_n^2 \gamma_n^{(r)}, \tag{C-23}$$

$$\frac{\partial\, J(\mu)}{\partial\, \mu^{(i)}} = 6 \sum_{n=0}^{LN-1} \xi_n^2 \gamma_n^{(i)}, \tag{C-24}$$

and the elements of the Hessian as

$$\frac{\partial^2\, J(\mu)}{\partial\, \mu^{(r)} \partial\, \mu^{(r)}} = 6 \sum_{n=0}^{LN-1} \left[4\xi_n (\gamma_n^{(r)})^2 + \xi_n^2 \beta_n \right], \tag{C-25}$$

$$\frac{\partial^2\, J(\mu)}{\partial\, \mu^{(r)} \partial\, \mu^{(i)}} = \frac{\partial^2\, J(\mu)}{\partial\, \mu^{(i)} \partial\, \mu^{(r)}} = 6 \sum_{n=0}^{LN-1} 4\xi_n \gamma_n^{(i)} \gamma_n^{(r)}, \tag{C-26}$$

$$\frac{\partial^2\, J(\mu)}{\partial\, \mu^{(i)} \partial\, \mu^{(i)}} = 6 \sum_{n=0}^{LN-1} \left[4\xi_n (\gamma_n^{(i)})^2 + \xi_n^2 \beta_n \right]. \tag{C-27}$$

The terms ξ_n and β_n represent the instantaneous power of the CM-reduced and correcting signals as defined in (C-6) and

$$\beta_n = \left(c_n^{(r)}\right)^2 + \left(c_n^{(i)}\right)^2, \tag{C-28}$$

respectively, and

$$\gamma_n^{(r)} = \bar{s}_n^{(r)} c_n^{(r)} + \bar{s}_n^{(i)} c_n^{(i)}, \tag{C-29}$$

$$\gamma_n^{(i)} = \bar{s}_n^{(i)} c_n^{(r)} - \bar{s}_n^{(r)} c_n^{(i)}. \tag{C-30}$$

are the real and imaginary parts of $\gamma_n = \bar{s}_n \cdot (c_n)^*$.

Bibliography

[1] 3GPP TSG RAN WG1 and 3GPP TSG RAN WG4, TDocs R4-040367, R1-040522 and R1-040642, "Comparison of PAR and Cubic Metric for power de-rating," May 2004.

[2] 3GPP TSG RAN WG1, TDoc R1-060023, "Cubic Metric in 3GPP-LTE," Jan. 2006.

[3] 3GPP TSG RAN WG1, TS 36.211, "Evolved Universal Terrestrial Radio Access (E-UTRA); Physical channels and modulation," Sept. 2007.

[4] 3GPP TSG RAN WG4, TR 36.803, "Evolved Universal Terrestrial Radio Access (E-UTRA); User Equipment (UE) radio transmission and reception," Dec. 2007.

[5] M. Abuelma'atti, "Frequency-Dependent Nonlinear Quadrature Model for TWT Amplifiers," *IEEE Transactions on Communications*, vol. 32, no. 8, pp. 982–986, Aug. 1984.

[6] M. S. Alouini, X. Tang, and A. J. Goldsmith, "An adaptive modulation scheme for simultaneous voice and data transmission over fading channels," *IEEE Journal on Selected Areas in Communications*, vol. 17, no. 5, pp. 837–850, May 1999.

[7] G. R. Arce, "Microstatistics in signal decomposition and the optimal filtering problem," *IEEE Transactions on Signal Processing*, vol. 40, no. 11, pp. 2669–2682, Nov. 1992.

[8] J. Armstrong, "Peak-to-average power reduction for OFDM by repeated clipping and frequency domain filtering," *IEE Electronics Letters*, vol. 38, no. 5, pp. 246–247, Feb. 2002.

[9] H. Atarashi, N. Maeda, S. Abeta, and M. Sawahashi, "Broadband packet wireless access based on VSF-OFCDM and MC/DS-CDMA," in *Proc. IEEE International Symposium on Personal, Indoor and Mobile Radio Communications*, vol. 3, Sept. 2002, pp. 992 – 997.

[10] E.-W. Bai, "An optimal two stage identification algorithm for Hammerstein-Wiener nonlinear systems," in *Proc. of the American Control Conference*, vol. 5, June 1998, pp. 2756–2760.

[11] R. W. Bäuml, R. F. H. Ficher, and J. B. Huber, "Reducing the peak-to-average power ratio of multicarrier modulation by selected mapping," *IEE Electronics Letters*, vol. 32, pp. 2056–2057, Oct. 1996.

[12] A. Behravan, "Evaluation and Compensation of Nonlinear Distortion in Multicarrier Communication Systems," Ph.D. dissertation, Chalmers University of Technology, June 2006.

[13] A. Behravan and T. Eriksson, "Some Statistical Properties of Multicarrier Signals and Related Measures," in *Proc. IEEE Vehicular Technology Conference Spring*, vol. 4, May 2006, pp. 1854 – 1858.

[14] A. Berman and C. Mahle, "Nonlinear Phase Shift in Traveling-Wave Tubes as Applied to Multiple Access Communications Satellites," *IEEE Transactions on Communications*, vol. 18, no. 1, pp. 37–48, Feb. 1970.

[15] S. A. Billings and S. Y. Fakhouri, "Identification of a class of nonlinear systems using correlation analysis," in *Proceedings of IEE*, vol. 125, July 1978, pp. 691–697.

[16] J. A. C. Bingham, "Multicarrier modulation for data transmission: an idea whose time has come," *IEEE Communications Magazine*, vol. 28, pp. 5–14, May 1990.

[17] W. Bosch and G. Gatti, "Measurement and Simulation of Memory Effects in Predistortion Linearizers," *IEEE Transactions on Microwave Theory and Techniques*, vol. 37, no. 12, pp. 1885–1890, Dec. 1989.

[18] S. Boumaiza and F. M. Ghannouchi, "Thermal Memory Effects Modeling and Compensation in RF Power Amplifiers and Predistortion Linearizers," *IEEE Transactions on Microwave Theory and Techniques*, vol. 51, no. 12, pp. 2427–2433, Dec. 2003.

[19] S. Boyd and L. Vandenberghe, *Convex optimization*. New York: Cambridge University Press, 2004.

[20] H. Breiling, S. H. Muller-Weinfurtner, and J. B. Huber, "SLM peak-power reduction without explicit side information," *IEEE Communication Letters*, vol. 5, pp. 239–241, June 2001.

[21] J. Bussgang, "Crosscorrelation function of amplitude-distorted gaussian signals," Research laboratory of electronics, Massachusetts Institute of Technology, Cambridge, Massachusetts, Tech. Rep. 216, Mar. 1952.

[22] X. Cai, S. Zhou, and G. B. Giannakis, "Group-orthogonal multicarrier CDMA," *IEEE Transactions on Communications*, vol. 52, no. 1, pp. 90 – 99, Jan. 2004.

[23] J. K. Cavers, "Amplifier linearization using a digital predistorter with fast adaptation and low memory requirements," *IEEE Transactions on Vehicular Technology*, vol. 39, no. 4, pp. 374–382, Nov. 1990.

[24] H. Chen and A. M. Haimovich, "Iterative estimation and cancellation of clipping noise for OFDM signals," *IEEE Communication Letters*, vol. 7, no. 7, pp. 305–307, July 2003.

[25] S. T. Chung and A. J. Goldsmith, "Degrees of freedom in adaptive modulation: a unified view," *IEEE Transactions on Communications*, vol. 49, no. 9, pp. 1561–1571, Sept. 2001.

[26] L. J. Cimini Jr. and N. R. Sollenberger, "Peak-to-average power ratio reduction of an OFDM signal using partial transmit sequences," *IEEE Communication Letters*, vol. 4, pp. 86–88, Mar. 2000.

[27] F. L. Combettes, "The foundations of set theoretic estimation," *Proceedings of IEEE*, vol. 81, no. 2, pp. 182–208, Feb. 1993.

[28] E. Dahlman, S. Parkvall, J. Sköld, and P. Beming, *3G Evolution. HSPA and LTE for Mobile Broadband*. Academic Press, Elsevier, 2007.

[29] D. Dardari, V. Tralli, and A. Vaccari, "A theoretical characterization of nonlinear distortion effects in OFDM systems," *IEEE Transactions on Communications*, vol. 48, pp. 1755–1764, Oct. 2000.

[30] J. A. Davis and J. Jedwab, "Peak-to-mean power control in OFDM, Golay complementary sequences, and Reed-Muller codes," Hewlett Packard, Tech. Rep. HPL-97-158, Dec. 1997.

[31] ——, "Peak-to-mean power control in OFDM, Golay complementary sequences, and Reed-Muller codes," *IEEE Transactions on Information Theory*, vol. 45, pp. 2397–2417, Nov. 1999.

[32] M. Deumal and R. Baldemair, "Signal metrics and nonlinearity effects in LTE uplink," in *Proc. IEEE Global Telecommunications Conference*, submitted on March 2008.

[33] M. Deumal and A. Behravan, "Unified analysis of nonlinear amplification effects and signal metrics in OFDM systems," *IEEE Transactions on Wireless Communications*, submitted on June 2008.

[34] M. Deumal, A. Behravan, T. Eriksson, and J. L. Pijoan, "Constrained clipping for Peak Power reduction of multicarrier systems by Tone Reservation," in *Proc. IEEE Vehicular Technology Conference Spring*, Apr. 2007, pp. 2195 – 2199.

[35] ——, "Evaluation of performance improvement capabilities of PAPR-reducing methods," *Springer Journal on Wireless Personal Communications*, Oct. 2007.

[36] M. Deumal, A. Behravan, and J. L. Pijoan, "On cubic metric reduction in OFDM systems by tone reservation," *IEEE Transactions on Communications*, submitted on November 2007, under revision for publication since March 2008.

[37] M. Deumal, J. L. Pijoan, I. Gutiérrez, and A. Behravan, "Peak reduction of multicarrier systems by Controlled Spectral Outgrowth," in *Proc. IEEE International Conference on Acoustics, Speech and Signal Processing*, vol. 4, May 2006, pp. 317 – 320.

[38] R. Dinis, P. Silva, and T. Araújo, "Joint Multiuser Detection and Cancelation of Nonlinear Distortion Effects for the Uplink of MC-CDMA Systems," in *Proc. IAESTED Conference on Signal and Image Processing*, Aug. 2006.

[39] H. Durney, "Adaptive Pre-Distortion for Nonlinear High Power Amplifiers in OFDM Systems," Ph.D. dissertation, Universitat Politècnica de Catalunya, Feb. 2004.

[40] P. V. Eetvelt, G. Wade, and M. Tomlinson, "Peak to average power reduction for OFDM schemes by selective scrambling," *IEE Electronics Letters*, vol. 32, pp. 1963–1964, Oct. 1996.

[41] N. Y. Ermolova, N. Nefedov, and S. Haggman, "An iterative method for non-linear channel equalization in OFDM systems," in *Proc. IEEE International Symposium on Personal, Indoor and Mobile Radio Communications*, vol. 1, Sept. 2004, pp. 484–488.

[42] European Telecommunications Standards Institute, EN 300 744, "Digital Video Broadcasting; Framing Structure, channel coding, and modulation for digital terrestrial television," Oct. 2004.

[43] K. Fazel and S. Kaiser, *Multi-Carrier and Spread Spectrum Systems*. John Wiley & Sons, 2003.

[44] A. Gatherer and M. Polley, "Controlling clipping probability in DMT transmission," in *Proc. Asilomar Conference on Signals, Systems and Computers*, vol. 1, Nov. 1997, pp. 578–584.

[45] A. Ghorbani and M. Sheikhan, "The effect of solid state power amplifiers (SSPAs) nonlinearities on MPSK and M-QAM signal transmission," in *Proc. 6th International Conference on Digital Processing of Signals in Communications*, Sept. 1991, pp. 193–197.

[46] M. Golay, "Complementary series," *IEEE Transactions on Information Theory*, vol. 7, no. 2, pp. 82–87, Apr. 1961.

[47] A. J. Goldsmith, "The capacity of downlink fading channels with variable rate and power," *IEEE Transactions on Vehicular Technology*, vol. 46, no. 3, pp. 569–580, Aug. 1997.

[48] A. J. Goldsmith and S. G. Chua, "Adaptive coded modulation for fading channels," *IEEE Transactions on Communications*, vol. 46, no. 5, pp. 595–602, May 1998.

[49] W. Greblicki, "Nonparametric identification of Wiener systems by orthogonal series," *IEEE Transactions on Automatic Control*, vol. 39, no. 10, pp. 2077–2086, Oct. 1994.

[50] S. H. Han and J. H. Lee, "An overview of peak-to-average power ratio reduction techniques for multicarrier transmission," *IEEE Wireless Communications Magazine*, vol. 12, pp. 56–65, Apr. 2005.

[51] G. R. Hill, N. Faulkner, and J. Singh, "Reducing the peak-to-average power ratio in OFDM by cyclically shifting partial transmit sequences," *IEE Electronics Letters*, vol. 36, no. 6, pp. 560–561, Mar. 2000.

[52] P. Hoeher, D. Kaiser, and P. Robertson, "Two-dimensional pilot-symbol-aided channel estimation by Wiener filtering," in *Proc. IEEE International Conference on Acoustics, Speech and Signal Processing*, vol. 3, Apr. 1997, pp. 1845 – 1848.

[53] A. Hyvarinen, J. Karhunen, and E. Oja, *Independent Component Analysis*. John Wiley & Sons, 2001.

[54] IEEE Std 802.16-2004, "IEEE Standard for Local and metropolitan area networks. Part 16: Air Interface for Fixed Broadband Wireless Access Systems," Oct. 2004.

[55] IST-2003-507581 WINNER, "D2.10 final report on identified RI key technologies, system concept, and their assessment," Dec. 2005.

[56] A. D. S. Jayalath and C. Tellambura, "Reducing the peak-to-average power ratio of orthogonal frequency division multiplexing signal through bit or symbol interleaving," *IEE Electronics Letters*, vol. 36, no. 13, pp. 1161–1163, June 2000.

[57] M. C. Jeruchim, P. Balaban, and K. S. Shanmugan, *Simulation of Communications Sytems*, 2nd ed. Boston, MA: Kluwer Academic Publishers, 2000.

[58] A. E. Jones, T. A. Wilkinson, and S. K. Barton, "Block coding scheme for the reduction of peak-to-mean envelope power ratio of multicarrier transmission schemes," *IEE Electronics Letters*, vol. 30, pp. 2098–2099, Dec. 1994.

[59] A. Katz, "Linearization: reducing distortion in power amplifiers," *IEEE Microwave Magazine*, vol. 2, no. 4, pp. 37 – 49, Dec. 2001.

[60] P. Kenington, "Linearized transmitters: an enabling technology for software defined radio," *IEEE Communications Magazine*, vol. 40, no. 2, pp. 156 – 162, Feb. 2002.

[61] D. Kim and G. L. Stuber, "Clipping noise mitigation for OFDM by decision-aided reconstruction," *IEEE Communication Letters*, vol. 3, no. 1, pp. 4–6, Jan. 1999.

[62] D. Kocur, J. Čížová, and S. Marchevský, "The Microstatistic Multi-User Reciever: Basic Principles and Preliminary Results," TD-03-008-P, COST–272: Packet-Oriented Service Delivery Via Satellite, Napoli, Italy, Nov. 2003.

[63] ——, "Sub-optimum MSF-MUD for CDMA Systems," Second COST–289 Workshop: Special Topics on 4G systems, COST–289: Spectrum and Power Efficient Broadband Communications, pp. 64–71, July 2005.

[64] D. Kocur, J. Krajňák, and S. Marchevský, "Multi-Channel Complex Non-Linear Microstatistic Filters. structure and Design," *Springer Journal on Wireless Personal Communications*, submitted for publication, Oct. 2005.

[65] ——, "Piece-Wise Linear Multi-Channel Complex Microstatistic Filters," in *Proc. International Conference on Intelligent Engineering Systems*, June 2006, pp. 53–56.

[66] J. Krajňák, M. Deumal, P. Pavelka, D. Kocur, J. L. Pijoan, and P. Galajda, "Multiuser detection of nonlinearly distorted MC-CDMA symbols by microstatistic filtering," *Springer Journal on Wireless Personal Communications*, Oct. 2007.

[67] B. S. Krongold and D. L. Jones, "PAR reduction in OFDM via active constellation extension," in *Proc. IEEE International Conference on Acoustics, Speech and Signal Processing*, vol. 4, Apr. 2003, pp. 525–528.

[68] ——, "PAR reduction in OFDM via active constellation extension," *IEEE Transactions on Broadcasting*, vol. 49, no. 3, pp. 258 – 268, Sept. 2003.

[69] ——, "An Active-Set Approach for OFDM PAR Reduction via Tone Reservation," *IEEE Transactions on Signal Processing*, vol. 52, no. 2, pp. 495 – 509, Feb. 2004.

[70] X. Li and L. J. Cimini Jr., "Effects of clipping and filtering on the performance of OFDM," *IEEE Communication Letters*, vol. 2, pp. 131–133, May 1998.

[71] Y. Li, "Piecewise linear system modeling based on a continuous threshold decomposition," *IEEE Transactions on Signal Processing*, vol. 44, no. 6, pp. 1440 – 1453, June 1996.

[72] ——, "Pilot-symbol-aided channel estimation for OFDM in wireless systems," *IEEE Transactions on Vehicular Technology*, vol. 49, no. 4, pp. 1207–1215, July 2000.

[73] V. Lottici and F. Giannetti, "A Novel Adaptive Digital Predistortion Scheme for MC-CDMA Systems," in *Proc. International Symposium on Wireless Personal Multimedia Communications*, no. 1, Sept. 2005, pp. 1–5.

[74] S. Loyka, V. Kostina, and F. Gagnon, "Symbol error rates of Maximum-Likelihood detector: convex/concave behavior and applications," in *Proc. IEEE International Symposium on Information Theory*, June 2007.

[75] F. J. MacWilliams and N. J. A. Sloane, *The theory of error-correcting codes*. North-Holland Mathematical Library, 1998.

[76] S. H. Müller and J. B. Huber, "OFDM with reduced peak-to-average power ratio by optimum combination of partial transmit sequences," *IEE Electronics Letters*, vol. 33, pp. 368–369, Feb. 1997.

[77] K. Narendra and P. Gallman, "An iterative method for the identification of nonlinear systems using a Hammerstein model," *IEEE Transactions on Automatic Control*, vol. 11, no. 3, pp. 546–550, July 1966.

[78] H. Ochiai and H. Imai, "Performance analysis of deliberately clipped OFDM signal," *IEEE Transactions on Communications*, vol. 50, pp. 89–101, Jan. 2002.

[79] A. Papoulis and S. U. Pillai, *Probability, Random Variables and Stochastic Processes*, 4th ed. McGraw-Hill, 2002.

[80] H. Poor and S. Verdu, "Probability of error in MMSE multiuser detection," *IEEE Transactions on Information Theory*, vol. 43, no. 3, pp. 858 – 871, May 1997.

[81] B. Popovic, "Synthesis of power efficient multitone signals with flat amplitude spectrum," *IEEE Transactions on Communications*, vol. 39, no. 7, pp. 1031–1033, July 1991.

[82] J. G. Proakis, *Digital communications*, 4th ed. McGraw-Hill, 2000.

[83] J. G. Proakis and M. Salehi, *Communication systems engineering*, 2nd ed. Prentice Hall, 2002.

[84] R. Raich, H. Qian, and G. T. Zhou, "Optimization of SNDR for amplitude-limited nonlinearities," *IEEE Transactions on Communications*, vol. 53, no. 11, pp. 1964–1972, Nov. 2005.

[85] C. Rapp, "Effects of HPA-nonlinearity on 4-DPSK-OFDM-signal for a digital sound broadcasting system," in *Proc. 2nd European conf. Satellite Communications*, 1991, pp. 179–184.

[86] A. A. M. Saleh, "Frequency-independent and frequency-dependent nonlinear models for TWT amplifiers," *IEEE Transactions on Communications*, vol. 29, pp. 1715–1720, Nov. 1981.

[87] M. Schetzen, "Nonlinear system modeling based on the Wiener theory," *Proceedings of IEEE*, vol. 69, no. 12, pp. 1557–1573, Dec. 1981.

[88] W. H. Sheen and J. S. Sheu, "On the adaptability of OFDM-CDMA forward link with time-frequency spreading in multi-path fading channels," in *Proc. IEEE Vehicular Technology Conference Fall*, vol. 1, Sept. 2005, pp. 617 – 621.

[89] P. Silva and R. Dinis, "Joint Multiuser Detection and Cancelation of Nonlinear Distortion Effects for the Uplink of MC-CDMA Systems," in *Proc. IEEE International Symposium on Personal, Indoor and Mobile Radio Communications*, Sept. 2006, pp. 1 – 5.

[90] A. Skrzypczak, P. Siohan, and J. Javaudin, "Power spectral density and cubic metric for the ofdm/oqam modulation," in *Proc. IEEE International Symposium on Signal Processing and Information Technology*, Aug. 2006, pp. 846 – 850.

[91] W. G. Song and J. T. Lim, "Pilot-symbol aided channel estimation for OFDM with fast fading channels," *IEEE Transactions on Broadcasting*, vol. 49, no. 4, pp. 398–402, Dec. 2003.

[92] S. P. Stapleton and F. C. Costescu, "An adaptive predistorter for a power amplifier based on adjacent channel emissions [mobile communications]," *IEEE Transactions on Vehicular Technology*, vol. 41, no. 1, pp. 49–56, Feb. 1992.

[93] L. Sundström, "Digital RF Power Amplifiers Linearizers. Analysis and Design," Ph.D. dissertation, Lund university, Aug. 1995.

[94] J. Tellado, "Peak to Average Power Reduction for Multicarrier Modulation," Ph.D. dissertation, Stanford University, Sept. 1999.

[95] J. Tellado and J. Cioffi, "Efficient algorithms for reducing PAR in multicarrier systems," in *Proc. IEEE International Symposium on Information Theory*, Aug. 1998, p. 191.

[96] J. Tellado, L. M. C. Hoo, and J. M. Cioffi, "Maximum-likelihood detection of nonlinearly distorted multicarrier symbols by iterative decoding," *IEEE Transactions on Communications*, vol. 51, no. 2, pp. 218–228, Feb. 2003.

[97] C. Tellambura, "Phase optimisation criterion for reducing peak-to-average power ratio in OFDM," *IEE Electronics Letters*, vol. 34, pp. 169–170, Jan. 1998.

[98] R. van Nee and R. Prasad, *OFDM for wireless multimedia communications*. Artech House, 2000.

[99] S. Verdú, *Multi-user detection*. Cambridge University Press, 1998.

[100] J. H. K. Vuolevi, T. Rahkonen, and J. P. A. Manninen, "Measurement Technique for Characterizing Memory Effects in rf Power Amplifiers," *IEEE Transactions on Microwave Theory and Techniques*, vol. 49, no. 8, pp. 1383–1389, Aug. 2001.

[101] S. Weinstein and P. Ebert, "Data Transmission by Frequency-Division Multiplexing Using the Discrete Fourier Transform," *IEEE Transactions on Communications*, vol. 19, pp. 628 – 634, Oct. 1971.

[102] T. Wigren, "Recursive prediction error identification using the nonlinear Wiener model," *Automatica*, vol. 29, no. 4, pp. 1011 – 1025, July 1993.

[103] ——, "Convergence analysis of recursive identification algorithms based on the nonlinear Wiener model," *IEEE Transactions on Automatic Control*, vol. 39, no. 11, pp. 2191 – 2206, Nov. 1994.

[104] T. A. Wilkinson and A. E. Jones, "Minimisation of the peak to mean envelope power ratio of multicarrier transmission schemes by block coding," in *Proc. IEEE Vehicular Technology Conference*, vol. 2, July 1995, pp. 825–829.

[105] A. Zhu and T. J. Brazil, "An adaptive volterra predistorter for the linearization of RF high power amplifiers," in *IEEE MTT-S International Microwave Symposium Digest*, vol. 1, June 2002, pp. 461–464.

Notation

Symbols and definitions

Scalars and vectors

$\mathbb{R}^M$	Set of real numbers of size M
$\mathbb{C}^M$	Set of complex numbers of size M
$\mathbb{N}^M$	Set of natural numbers of size M
$\mathbb{Z}^M$	Set of integer numbers of size M
$\mathbf{x} = [x_1, \ldots, x_M]^\mathsf{T} = [x_1; \ldots; x_M]$	Scalar samples constituting the column vector $\mathbf{x}$
x_i	i-th sample of vector $\mathbf{x}$
$x^{(r)},\ \mathbf{x}^{(r)}$	Real part of the scalar x or vector $\mathbf{x}$
$x^{(i)},\ \mathbf{x}^{(i)}$	Imaginary part of the scalar x or vector $\mathbf{x}$
$x^*,\ \mathbf{x}^*$	Complex conjugate of the scalar x or vector $\mathbf{x}$
$\mathbf{x}^\mathsf{T}$	Transpose of vector $\mathbf{x}$
$\mathbf{x}^\mathsf{H}$	Hermitian of vector $\mathbf{x}$
$\mathcal{I}_M = \{i_1, i_2, \ldots, i_M\}$	List of elements constituting the set $\mathcal{I}$

Functions

$\mathrm{A}(x)$	Function A: $\mathbb{R} \to \mathbb{R}$ or $\mathbb{C} \to \mathbb{C}$
$\mathrm{A}(\mathbf{x})$	Function A: $\mathbb{R}^M \to \mathbb{R}$ or $\mathbb{C}^M \to \mathbb{C}$
$\mathbf{A}(x)$	Function A: $\mathbb{R} \to \mathbb{R}^N$ or $\mathbb{C} \to \mathbb{C}^N$
$\mathbf{A}(\mathbf{x})$	Function A: $\mathbb{R}^M \to \mathbb{R}^N$ or $\mathbb{C}^M \to \mathbb{C}^N$
$\lfloor x \rfloor$	Floor. Largest integer smaller than or equal to x
$\lceil x \rceil$	Ceil. Smaller integer larger than or equal to x

Random variables and stochastic processes

$\langle \mathbf{x} \rangle, \langle x(t) \rangle$	Sample average of the vector $\mathbf{x}$, time average of the signal $x(t)$
$\langle \mathbf{x}, \mathbf{y} \rangle, \langle x(t), y(t) \rangle$	Inner product between the vectors(signals) $\mathbf{x}(x(t))$ and $\mathbf{y}(y(t))$
$E[X]$	Expected value of the random variable X
σ_X^2	Variance of the random variable X
$\text{kurt}(X), \tilde{\kappa}(X)$	Kurtosis and normalized kurtosis of the random variable X, respectively
$I(X;Y)$	Mutual information between two random variables X and Y
$E[X(t)]$	Expected value of the random process $X(t)$
$R_{XX}(t_1, t_2)$	Auto-correlation function of the random process $X(t)$
$R_{XY}(t_1, t_2)$	Cross-correlation function of the random processes $X(t)$ and $Y(t)$

Definitions

L	Oversampling factor
N	Number of subcarriers
T	Sampling interval
T_s	OFDM symbol duration
s_n	n-th sample of the time-domain signal vector $\mathbf{s}$
S_k	k-th sample of the frequency-domain signal vector $\mathbf{S}$
$PAPR$	Average PAPR of a multicarrier system
$PAPR_{max}$	System PAPR, i.e. the maximum PAPR of a multicarrier system
CM	System CM, i.e. the average CM of a multicarrier system
CM_{max}	Maximum CM of a multicarrier system
$\mathbf{S}^{\text{zp}}$	Zero padded frequency-domain signal vector $\mathbf{S}$
$\bar{s}_n, \bar{\mathbf{s}}$	PAPR/CM reduced signal.
$\tilde{s}_n, \tilde{\mathbf{s}}$	Clipped/segmented signal.
$\hat{s}_n, \hat{\mathbf{s}}$	Estimation of the scalar s_n or vector $\mathbf{s}$
$\check{s}_n, \check{\mathbf{s}}$	Candidate to be the estimation of the scalar s_n or vector $\mathbf{s}$
$\mathcal{P}_M = \{p_1, p_2, \ldots, p_M\}$	Set of data tones indexes in tone reservation technique
$\mathcal{Q}_R = \{q_1, q_2, \ldots, q_R\}$	Set of reserved tones indexes in tone reservation technique

Acronyms

3GPP	Third Generation Partnership Project
ACE	Active Constellation Extension
ACLR	Adjacent Channel Leakage Ratio
A/D	Analog-to-Digital
A/D/A	Analog-to-Digital and Digital-to-Analog
AM/AM	Amplitude Modulation/Amplitude Modulation
AM/PM	Amplitude Modulation/Phase Modulation
ASIC	Application-Specific Integrated Circuit
AWGN	Additive White Gaussian Noise
BER	Bit Error Rate
CCDF	Complementary Cumulative Density Function
CDF	Cumulative Density Function
CDMA	Code Division Multiple Access
CM	Cubic Metric
C-M-MSF	Complex-Valued Multi-Channel Microstatistic Filters
CSO	Controlled Spectral Outgrowth
D/A	Digital-to-Analog
DC	Direct Current
DFT	Discrete Fourier Transform
DFTS-OFDM	DFT-Spread OFDM
DS	Direct-Sequence
DS-CDMA	Direct-Sequence Code Division Multiple Access
DS-SS	Direct-Sequence Spread-Spectrum
DVB	Digital Video Broadcasting
EVM	Error Vector Magnitude
FDD	Frequency-Division Duplex
FDMA	Frequency Division Multiple Access
FH	Frequency Hopping
FH-SS	Frequency Hopping Spread-Spectrum

FFT	Fast Fourier Transform
FPGA	Field Programmable Gate Array
GO-MC-CDMA	Group-Orthogonal Multicarrier Code Division Multiple Access
HF	High Frequency
HPA	High Power Amplifier
IBO	Input Back Off
ICI	Inter-Carrier Interference
IDFT	Inverse Discrete Fourier Transform
IFFT	Inverse Fast Fourier Transform
ISI	Inter-Symbol Interference
ITU	International Telecommunication Union
LAN	Local Area Network
LTE	Long-Term Evolution
MAC	Multiplications And Accumulations
MAI	Multiple Access Interference
MC	Multicarrier
MC-DS-CDMA	Multicarrier Direct-Sequence Code Division Multiple Access
MC-CDMA	Multicarrier Code Division Multiple Access
MC-SS	Multicarrier Spread Spectrum
ML	Maximum Likelihood
MMSE	Minimum Mean-Squared Error
MSE	Mean-Squared Error
MSF	Micro-Statistic Filter
MUD	Multiuser Detector
NL	Nonlinearity
OBO	Output Back Off
OCM	Objective Cubic Metric
OFCDMA	Orthogonal Frequency and Code Division Multiple Access
OFDM	Orthogonal Frequency Division Multiplexing
OFDMA	Orthogonal Frequency Division Multiple Access

PA	Power Amplifier
PAPR	Peak-to-Average Power Ratio
PD	Predistortion
PDF	Probability Density Function
PN	Pseudo-Noise
POCS	Projection Onto Convex Sets
PSD	Power Spectral Density
PSK	Phase Shift Keying
PTS	Partial Transmit Sequences
QAM	Quadrature Amplitude Modulation
QCQP	Quadratically Constrained Quadratic Program
QPSK	Quadrature Phase Shift Keying
RAN	Radio Access Network
RCM	Raw Cubic Metric
RF	Radio Frequency
SC-FDMA	Single Carrier Frequency Division Multiple Access
SF	Spreading Factor
SGP	Smart Gradient Project
SL	Soft Limiter
SLM	Selected Mapping
SNR	Signal-to-Noise Ratio
SNDR	Signal to Noise-plus-Distortion Ratio
SS	Spread Spectrum
SS-MC-MA	Spread Spectrum Multicarrier Multiple Access
SSPA	Solid State Power Amplifier
SSS	Strict-Sense Stationary
TDD	Time-Division Duplex
TI	Tone Injection
TR	Tone Reservation
TWTA	Traveling-Wave Tube Amplifier

VSF	Variable Spreading Factor
WF	Wiener Filter
WINNER	Wireless World Initiative New Radio
WSS	Wide-Sense Stationary